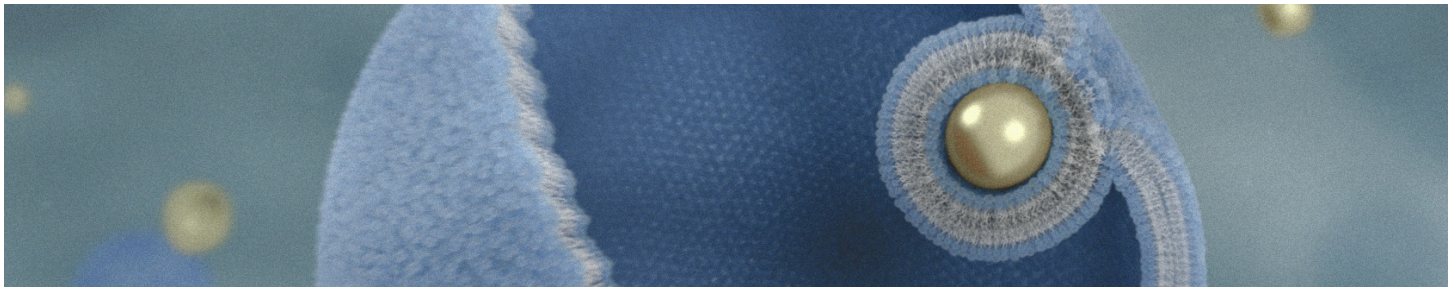

Interactions of Gold Nanoparticles with Polymeric Membranes

Dissertation

zur Erlangung des Grades

"Doktor der Naturwissenschaften"

im Promotionsfach Chemie

am Fachbereich Chemie, Pharmazie und Geowissenschaften

der Johannes Gutenberg Universität Mainz

vorgelegt von

Amelie Helena Ruth Koch

geboren in Freiburg im Breisgau

Mainz, 2014

MAX-PLANCK-GESELLSCHAFT

Die vorliegende Arbeit wurde im Zeitraum von Dezember 2011 bis November 2014 am Max-Planck-Institut für Polymerforschung in Mainz unter der Anleitung von Frau [redacted] und Herrn [redacted] angefertigt.

Tag der mündlichen Prüfung:	16.12.2014
Dekan:	[redacted]
Erster Berichterstatter:	[redacted]
Zweiter Berichterstatter:	[redacted]

D77

Nur die Gegensätze lehren einen die Welt kennen:
Wer nicht ums Dunkel weiß,
kann das Licht nicht erkennen.

aus Japan

Contents

1. Introduction

Determining the interactions between nanoparticles and membranes is of high interest for many different fields of research. In our everyday life, people become progressively exposed to nanoparticles, since nanotechnological applications are on the rise. While the number of applications of nanoparticles increases, it is more and more needed to understand the effect of nanoparticle expusure to humans and to study their potential toxicity. Particle toxicity is often related with their ability of entering cells and their fate and behavior once inside a cell. In contrast, nanoparticles are also utilized for imaging and diagnostics in the medical field, where interactions with tissues and cells is desired. Consequently, understanding the interactions of nanoparticles and cells is crucial for almost all applications related to nanotechnology. In vitro cytotoxicity studies have been performed for a wide range of different nanoparticles [Lew08], but science is still far from completely understanding the uptake-process into cells [Jia08].

Since direct investigation of living cells is rather complex, an artifical model system is needed, which mimics the nanomechanical properties of a cell membrane, but excludes all irrelevant features of a cell. In addition, multiple convenient characterization methods should be applicable and easy handling of the system is favored. It was found that vesicles formed from amphiphilic block-copolymers, so-called *polymersomes*, are suitable membrane models with mechanical properties close to those of liposomes (see Figure 1.1), the main component of natural cell membranes [Jas12b, Jas12a, Jas12d]. The main advantages of polymersomes over cells are long-term stability, the possibility of tuning their properties due to their fully synthetic nature, and their easy handling as well as convenient experimental requirements. The formed vesicles are of perfectly spherical shape and their size can be adjusted according to the experimental needs. In this work, a reduced size of

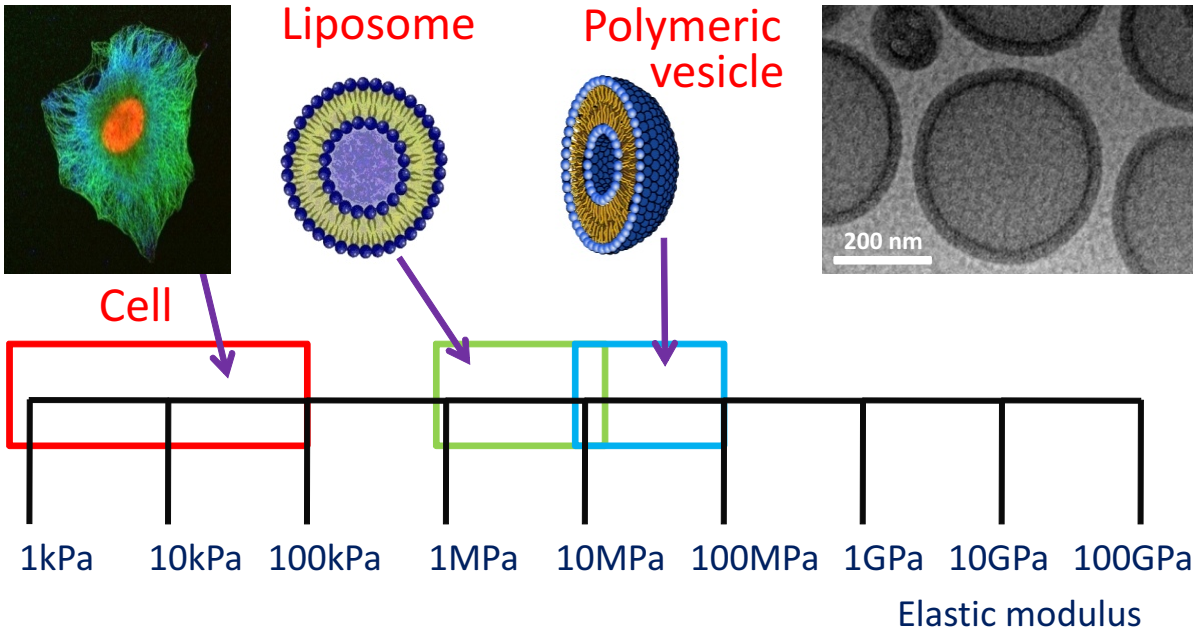

Figure 1.1: *Comparision of elastic moduli of cell membranes, liposomes and polymersomes as well as their schematic structures. The cryo-TEM image in the right shows a typical polymersome in (frozen) water.*

the polymersomes (diameter $d = 300$ nm) was chosen in order to enable characterization techniques like photon correlation spectroscopy (PCS) or cryogenic transmission electron microscopy (cryo-TEM). PCS allows the studies of both static and dynamic properties of a very large number of individual structures in the sample, whereas cryo-TEM provides a more descriptive image of the system.

Nanoparticles, that are particles from 1 nm to 100 nm in diameter, were extensively researched during the last decades [Sch14]. The number of available nanoparticles is endless. Besides many different materials, different shapes and sizes can be obtained. In general, one distinguishes between inorganic (metals or oxides) and organic (carbon or polymeric) nanoparticles. Among metal particles, gold colloids are probably the most prominent examples, and they have been used in clinical therapy as early as the 1920s [Aas98]. Gold nanoparticles (AuNPs) can be synthesized in many different shapes, including spheres and rods, but also more advances geometries, such as mono-, bi-, tri-, and tetrapods [Che03], triangles [Sha05], stars [Yua12], or nanocages [Che05], are accessible.

AuNPs exhibit a number of physical properties which make them very suitable for medical applications, such as the absorbance of light in the visible and near-infrared region [Pay06, Fle10], the high optical scattering intensities [ES05], the absorbance of X-rays [Liu10], as well as the ability to transform absorbed light into heat [Che12]. In addition, the surface of the gold nanoparticles can easily be modified thanks to thiol chemistry.

The absorbance of light is probably the most prominent property of colloidal gold, since it is responsible for its characteristic colors, which are absent in the bulk material. This property is attributed to the gold particle's surface plasmons, and the effect is very sensitive to the particle's size, shape and chemical surrounding [Lin99]. This sensitivity and the high scattering intensity of gold nanoparticles make them the perfect candidates for being tracers in biomedical or sensing applications. On the other hand, polymersomes offer a good system for investigating the interactions of nanoparticles with polymeric membranes. Consequently, the combination of both polymersomes and gold nanoparticles results in a highly sensitive methodology for sensing these interactions. In addition, polymersomes and nanoparticles can be distinguished in light scattering experiments without labeling with dyes, as will be shown in this work.

This thesis consists of five chapters. Following this introduction, basic information on membranes and colloidal systems are given. In addition, the principles of light scattering of colloids is discussed. Chapter 3 gives an overview of the experimental methods used in this work with a focus set on photon correlation spectroscopy. Results are presented in Chapter 4, subdivided into four main parts: In the first part, synthesis of the amphiphilic block-copolymer PDMS-*b*-PMOXA is described, as well as the formation of vesicles by extrusion and their characterization by PCS and cryo-TEM. The second part contains the synthesis and characterization of gold nanospheres, discussing in detail their inherent internal crystallinity and their asymmetric surface coating. Part three and four comprise the study of interactions of gold nanospheres and gold nanorods with vesicles, respectively. In the final chapter, the results are summarized and an outlook for future experiments is given.

2. Theoretical Background

2.1 Membranes

A membrane is a material that separates two compartments from each other, facilitating the transport of some material while hindering the transport of others. The permeability of a membrane defines its function, and practical applications are widely spread. Some prominent examples for membranes are *biomembranes*, which can be found in living cells, *dialysis membranes*, which are used for purification of blood, and *membrane filters*, which are used for (waste) water purification. In this section, an introduction on biological membranes is given. The focus lies on transmembrane transport and in particular on the experimental and theoretical reports of endocytosis, which is the invagination of molecules or small particles into cells. Furthermore, artificial membranes, which serve as membrane mimics, are introduced and discussed.

2.1.1 The Cell Membrane

The cell membrane is a biological membrane, which surrounds the living cell and separates its interior from the exterior environment. It protects and organizes cells, controlling which substances enter and the amount that comes in. Natural cellular membranes are composed of phospholipids which align side-by-side to form bilayer sheets. The hydrophilic phosphate heads face both towards the water-based cytoplasm and the exterior of the cell, while the hydrophobic hydrocarbon tails line up in the bilayer's interior. There are approximately $5 \cdot 10^6$ lipid molecules per square micrometer area of lipid bilayer [Alb02]. Although the cellular membrane is primarily composed of lipids, they

only account for roughly half of its mass. The other half is due to proteins which are embedded into the membrane and stick out on either one side (surface protein) or both sides (integral protein). These proteins help control the transport of ions, molecules and particles in and out of the cell, and also help mediate cell signaling [Lod00]. A schematic representation of the biomembrane is given in Figure 2.1.

Cellular membranes are fluid under physiological conditions, but they become gel-like at cooler temperatures [Lod00]. This change of state is called *phase transistion*. When in the fluid state, individual lipid molecules can diffuse freely within one side of the bilayer ($\sim 10^7$ times per second), but they rarely flip from one side of the bilayer to the other (less than once a month). The fluidity of the cell membrane can be precisely controlled by its composition and temperature. In general, phospholipids with short or cis-double bonded hydrophobic tails increase the fluidity of the membrane, whereas the incorporation of cholesterol and glycolipids into the membrane make the bilayer stiffer [Coo00]. Phase transition has even been observed upon contact of phospholipid bilayers with charged nanoparticles [Wan08].

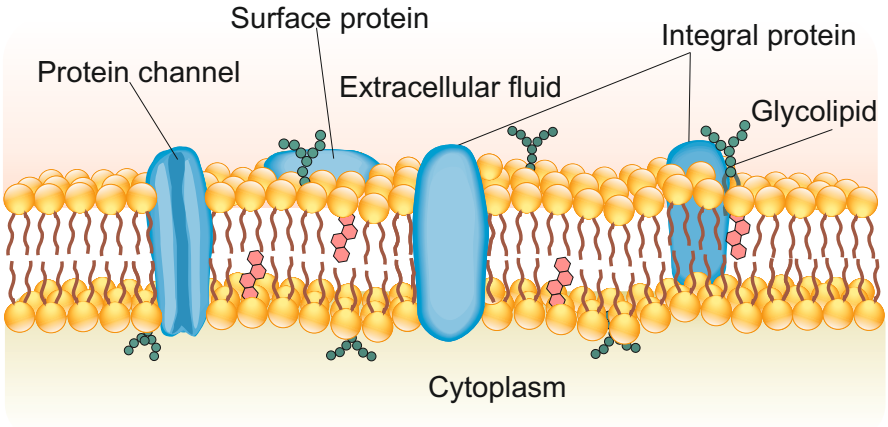

Figure 2.1: *Schematic representation of a biomembrane. A phospholipid bilayer, which also contains glycolipids (green molecules), cholesterol (red molecules) and some other minor components, separates the cytoplasm from the extracellular fluid. Surface proteins and transmembrane proteins are embedded into the membrane.*

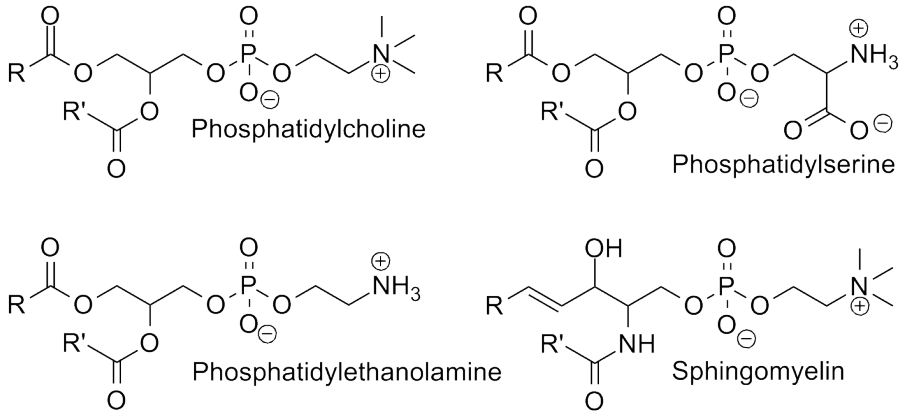

Figure 2.2: *The four major phospholipids in mammalian plasma membranes with different head groups are shown.*

There are four predominant phospholipids which constitute more than half of the mass of lipid in the plasma membrane of most mammalian cells: *phosphatidylcholine, phosphatidylethanolamine, phosphatidylserine, and sphingomyelin* (Figure 2.2). Only phosphatidylserine is negatively charged, whereas the other three are electrically neutral at physiological pH values. In general, the different lipid molecules are randomly distributed within each monolayer of the lipid bilayer. However, small microdomains of ~ 70 nm in diameter (*lipid rafts*) can be formed which contain mostly sphingolipids and cholesterol [Lin10]. In addition, the composition of the outer and the inner monolayer may differ significantly, which results in a charge difference between the two halves of the bilayer. The thickness of the cell membrane ranges from 7 to 9 nanometers [Cur89].

2.1.2 Biological Transport Through Membranes

In biological systems, many substances can be transported from one side of the cell membrane to the other, although the phospholipid membrane is not permeable for most molecules and particles. In general, one can distinguish three main transport processes (Figure 2.3): passive (Fickian) diffusion, facilitated diffusion (passive transport), and active transport. Small hydrophobic molecules can pass the membrane by passive diffusion due to a concentration gradient or an electrochemical gradient. Consequently, the entropy of the system will increase. Here, no input of other energy is required. For facilitated

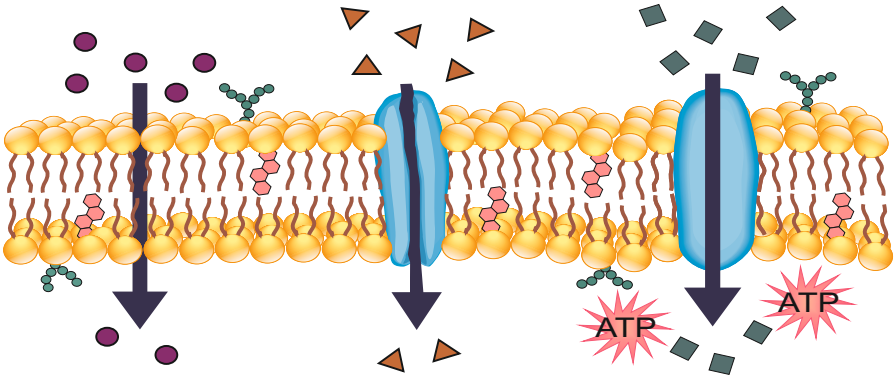

Figure 2.3: *Schematic of passive diffusion, facilitated diffusion and active transport (from left to right) in biomembranes.*

diffusion, membrane channels are involved in this diffusion process. These membrane channels are embedded in the membrane and form small tunnels, which are selective for specific ions or molecules. Again, no metabolic energy is consumed. In contrast to passive transport, active transport requires input of additional energy from an outside source. Therefore, ions and molecules can be translocated against a concentration or electrochemical gradient, decreasing the energy of the system. In general, the energy for active transport is provided by hydrolysis of adenosine triphosphate (ATP) .

The transport processes mentioned above describe how ions and small molecules can directly pass through the lipid bilayer without disrupting the membrane. However, larger molecules or even particles cannot diffuse through the membrane or its channels, but need to be absorbed by being engulfed by the cell. This process is called endocytosis. Upon contact of the substance with the membrane, a portion of the membrane becomes deformed and invaginated until the substance is completely wrapped. Consequently, an intracellular vesicle is formed, which is then pinched off and released into the cellular interior. Such an internalization process is schematically shown in Figure 2.4.

In biology, endocytosis pathways can be subdivided into four different catergories: clathrin-mediated endocytosis, caveolae, macropinocytosis, and phagocytosis. A detailed review of all endocytosis pathways is beyond the scope of this thesis and can be found in [Muk97], [LR05], [Doh09] and [McM11].

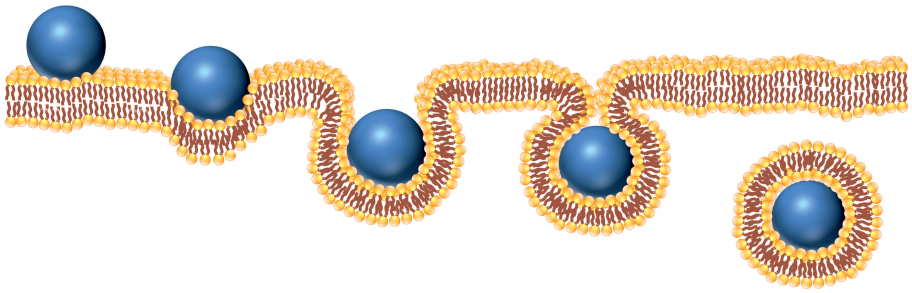

Figure 2.4: *Close-up of the endocytosis process of particles. The membrane wraps around the particle and forms a vesicle, which is then internalized into the cell. An endosome is formed.*

2.1.3 Theoretical Models of Endocytosis

Endocytosis in biological systems occurs via a complex mechanism which has not yet been understood completely. Therefore, theoretical models were developed to describe the process of endocytosis and to predict the interactions between particles and membranes. In an oversimplified physical approach, endocytosis can be described by two competing processes: adhesion-energy gain upon close contact between a nanoparticle and a membrane due to attractive interactions between them and deformation-energy cost upon bending of the membrane. Basically, a nanoparticle will attach on the membrane when the gained adhesion energy is greater than the energy needed to deform the membrane upon wrapping. Many different computer simulations can model the interactions of nanoparticles with membranes through using different mathematical descriptions of the system.

A very simple theoretical model by Deserno *et al.* uses coarse-grained membrane simulations to describe the interactions between a homogeneous vesicle and a colloidal particle [Des02]. Adhesion between the vesicle and the particle as well as deformation of the membrane were investigated. Under specific conditions, the particle can either be unbound, partially wrapped or fully enveloped, depending on on the physical properties of the system. These properties include the ratio of adhesion and membrane stretching energies, the size ratio between particle and vesicle, and the bending energy of the membrane. It was found that complete wrapping of the particle takes place if the the membrane tension

is low enough and if the size ratio between particle and vesicle is in a specific (intermediate) size range. Particles that are either too small or too large cannot be taken up by the vesicle. Therefore, the process of endocytosis is strongly size-dependent [Des04, Des03].

Balazs and co-workers examined the interactions of synthetic vesicles with spherical nanoparticles using dissipative particle dynamics [Smi07]. They also found that, for complete wrapping of the particle, there is a threshold adhesion strength even at zero membrane tension. However, they did not observe fission of the fully wrapped particle from the inner leaflet of the membrane, but noticed the formation of a membrane "eyelid" (Figure 2.5). In order to allow the wrapped particle to detach from the membrane (fission), an inhomogeneous membrane is needed, consisting of an adhesive raft in an otherwise nonadhesive membrane. This is due to the draft's interfacial energy, which is reduced by a fission process at the membrane neck, thus releasing the endosome (wrapped particle) from the membrane. Figure 2.5 shows multiple cross-section images for different wrapping processes.

Compared to wrapping of spheres, the wrapping of ellipsoidal or cylindrical particles is qualitatively different [Das13]. For spherical particles and zero membrane tension, only two possible stable states exist: a zero-wrapped state and a completely wrapped state, and the transition between these is continuous. This is due to the fact that upon membrane wrapping around a perfect sphere, the bending energy stays constant. A partially wrapped state is only possible if the membrane possesses a finite tension. However, for ellipsoidal particles, this half-wrapped state is possible for both zero and non-zero membrane tension. A partially wrapped state is already possible at low adhesion energies and is separated from the fully wrapped state by a relatively high energy barrier. It was shown that the higher the aspect ratio of the particle, the more easily it can attach to the membrane. However, at the same time, an increasing aspect ratio makes it more difficult to achieve complete wrapping due to the elevated curvature at the tips of the particle.

In addition to ellipsoidal particles, Dasgupta *et al.* have also studied the interactions of other nonspherical particles with membranes [Das14]. Although geometrically similar, nanorods show qualitatively different wrapping behavior compared to ellipsoids. Ellipsoids are wrapped by a *submarine mode*, where the particle's long axis is oriented parallel

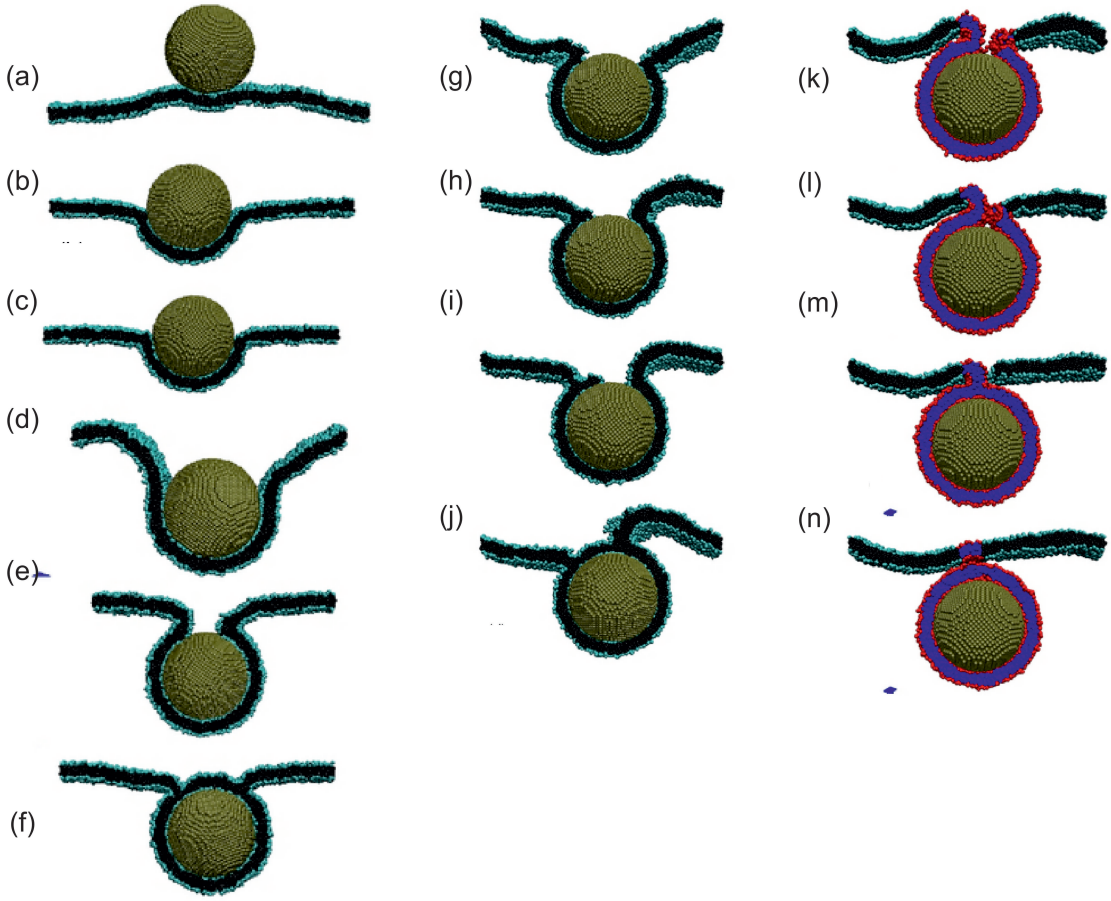

Figure 2.5: *(a) Cross-section images of membrane wrapping around a particle at various values of adhesion energy. (b) Time sequence showing a cross-section of the formation of a membrane "eyelid" which prevents fission of the particle from the inner leaflet of the membrane. (c) Time sequence of an inhomogeneous membrane wrapping around a particle, forming a neck and finally allowing the particle to separate from inner leaflet of the membrane (adapted with permission of the American Institute of Physics from [Smi07]).*

to the membrane, and the wrapping process is continuous. In contrast, rod-like particles attach with the long axis normal to the membrane, because parallel binding would cost too much deformation energy of the membrane. Depending on the sharpness of the particle's edges and on its aspect ratio, the rod either enters in a *rocket mode* without reorientation, or it switches back to parallel orientation after initial binding and then

back to normal orientation (competing *submarine* and *rocket mode*). Generally, particles with low aspect ratios and/or sharp edges prefer the rocket mode, whereas the other mode is more favorable for particles with high aspect ratios and/or rounded edges.

All these theoretical models assume homogeneous surface properties of the particle and homogeneous membranes. Multicomponent membranes and additional features like cell cytoskeleton or patchy particles require more detailed calculations. However, the theoretical models give a good overview on the physical background of endocytosis and predict the passage of nanoparticles across membranes under certain conditions.

2.1.4 Membrane Models

Biological membranes are rather complex structures, containing lipids, proteins, polysaccharides, etc. (see subsection 2.1.1 (The Cell Membrane)) and thus making direct investigation of nanoparticle-membrane interactions difficult. Therefore, in order to study the interactions between membranes and particles, cell membrane mimics are used. Vesicles formed by self-assembly of phospholipids in water, so-called *liposomes* [Ban93], are the closest model to the cellular membrane. However, these liposomes are often unstable and tend to fuse or flocculate [Mat95]. The formation of lipid bilayers can also be mimicked by amphiphilic block copolymers (see subsection 2.2.2 (Self-Assembly Principles)), which consist of a hydrophobic polymer block covalently linked to a hydrophilic polymer block, and thus have the same amphiphilic character as phopholipids. Amphiphilic block copolymers can be synthesized in large quantities via polymerization reaction, and are therefore easily accessible and non-expensive raw materials. Similar to lipids, amphiphilic block copolymers self-organize in water into so-called *polymersomes* [Dis06], so they are promising model systems for biomembranes. Their chemical, physical and mechanical properties should be similar to liposomes, but can be, due to their synthetic origin, synthetically tuned in order to match the requirements of the desired membrane.

The most important parameters for cell membrane mimicks are membrane fluidity and stability: due to the low molecular weight of lipids and also due to their phase transition at temperatures below physiological conditions, lipid molecules are highly mobile within the membrane. This is responsible for high membrane elasiticity in liposomes, but low

stability in vesicles. Several efforts were made to stabilize liposomes, e.g. by photopolymerization [Mor03, Spe93], by steric stabilization due to incorporation of PEG-ylated lipids or PEG-containing polymers into the membrane [DS07, Kos99, Las94, Ran03], by adsorption of polyelectrolytes [Mad09, Que10] or even by charged nanoparticles on the liposome's surface [Sav11, Yu07b, Mic13]. In contrast to liposomes, polymersomes exhibit only moderate or even very low exchange rates of polymer chains between aggregates. In addition, they possess higher chemical stability towards oxidation [Kem88, Log80, Fra84] and/or hydrolysis of ester bonds [Gri89, Gri93, Ken81], resulting in much longer lifetimes while remaining similar membrane fluidity. Prominent examples for polymersomes in water are PEO-*b*-PBD (poly(ethyleneoxide)-*block*-polybutadiene) and the hydrogenated homolog PEO-b-PEE (PEO-*block*-poly(ethylethylene() [Dis99, AE01, Lee02], PEO-PPS (PEO-poly(propylene sulfide)) [Nap01], PEO-PLA (PEO-polylactide) [Bat97], as well as PDMS-*b*-PMOXA (poly(dimethylsiloxane)-*block*-poly(2-methyloxazoline) as a diblock copolymer [Egl11] and PMOXA-PDMS-PMOXA as a triblock copolymer [Nar00], just to name a few. In general, the polymersomes become more stable but less fluid with increasing molecular weight of the single polymer chain [Dis02, Dis06]. The stability increases linearly until it reaches a plateau, whereas the fluidity (lateral mobility of the individual polymer chains) decreases drastically when the chains become long enough to entangle (see Figure 2.6). Membrane thicknesses of the polymersomes also increase with increasing molecular weight of the building blocks, showing a larger range than lipid membranes. However, a minimum membrane thickness of d $\approx$ 8 nm seems to be required for stable polymersomes [Sch99, Ber02]. Hence, the membrane thicknesses are always larger than for liposomes, and many integral membrane proteins, which are optimized for lipid membranes, may not be compatible with these thick polymersome membranes. Nevertheless, Meier *et al.* reported on the insertion of integral membrane proteins into triblock PMOXA-*b*-PDMS-*b*-PMOXA membranes with d $\approx$ 10 nm [Mei00]. This is possible because polymer chains can be significantly compressed and due to their polydispersity, shorter chains can segregate around a membrane protein.

Besides their increased stability, polymersomes have the advantage that their properties can be adjusted by a precise molecular design of the polymer chains and/or by mixing

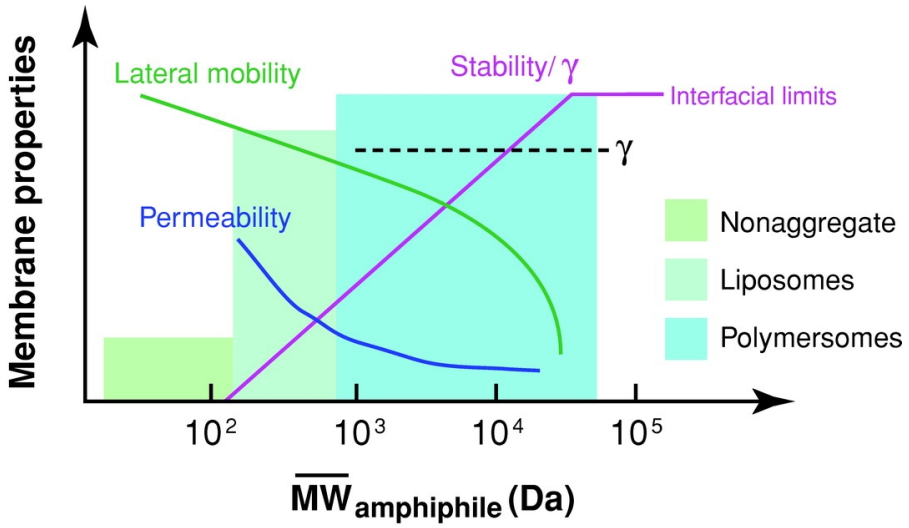

Figure 2.6: *Schematic plot of typical physical properties of vesicles versus molecular weight of the constituent amphiphiles (Used with permission of Annual Reviews from [Dis06]).*

different amphiphiles for membrane formation. Depending on their field of application, e.g. for drug delivery, their permeability or their ability to release loaded drugs can be modulated [LM11]. Their surface functionality [Egl11] as well as membrane inhomogeneity [Win13] can be tuned.

Jaskiewicz *et al.* studied the mechanical properties of PDMS-*b*-PMOXA polymersomes by atomic force microscopy (AFM). They found that these polymersomes exhibit a bending modulus around 5-7 times greater than that of gel-like lipids [Jas12d]. This is due to the higher membrane thickness (d $\approx$ 16nm) compared to natural liposomes (d $\approx$ 5nm). However, compared to other polymersomes based on PS-*b*-PAA (polystyrene-*block*-poly(acrylic acid)), the PDMS-*b*-PMOXA polymersomes are more flexible by 1 order of magnitude. This difference results from the very low T_g of the PDMS-*b*-PMOXA polymer ($T_g \approx -124$ °C). At the same time, PDMS-*b*-PMOXA polymersomes exhibit long-time stability in water without the tendency to fuse, and they even remained stable when adsorbing onto silica surfaces [Jas12d]. This combination of high stability and elevated elasticity makes PDMS-*b*-PMOXA polymersomes auspicious candidates for model membranes.

2.1.5 Experimental Transport of Nanoparticles Through Membranes

As seen previously in subsection 2.1.3 (Theoretical Models of Endocytosis), the wrapping of nanoparticles through membranes has been extensively studied theoretically and by simulations due to the importance of this topic for understanding nanoparticle bioactivity and nanotoxicity. However, concrete experiments of interactions of nanoparticles with model membranes are scarce, and most experimental reports are on direct investigation of nanoparticle uptake into living cells. Experiments on the transport of nanoparticles into mammalian cells suggested that nanoparticles enter red blood cells and cyt-D-blocked macrophages by non-endocytotic pathways, since both systems lack endocytotic capabilities [Gei05, RR06]. However, when using liposomes as a mimic for a biological membrane, no passive transmembrane transport of gold nanoparticles could be observed [Ban07]. Some experimental reports on the adhesion and spontaneous wrapping of nanoparticles by liposomes are published [Die97, Kol99, Fer03, Mic13]. The adhesion of the nanoparticles is based on electrostatic interactions, but the (partially) wrapped particles remained attached to the vesicle's periphery. LeBihan *et al.* observed nanoparticle uptake into large unilamellar DOPC (1,2-dioleoyl-*sn*-glycero-3-phosphocholine) liposomes by using cryo-electron tomography [LB09], demonstrating that nanoparticles can be transported through a lipid membrane via an invagination process similar to endocytosis, but without any supplementary energy from the biological cell.

So far, Jaskiewicz *et al.* were the first and only to report on the uptake of nanoparticles into polymersomes, which are synthetic membranes. They used vesicles composed of PDMS-*b*-PMOXA with a definite size of around 250 nm in diameter and both polystyrene and silica nanoparticles with smaller diameters of ≈ 30 nm. To visualize and analyze the internalization process, cryogenic transmission electron microscopy (cryo-TEM), fluorescence correlation spectroscopy (FCS), and photon correlation spectroscopy (PCS) were used [Jas12b]. Similar to LeBihan *et al.*, they observed nanoparticle uptake upon membrane deformation. They divided this endocytosis-like process into four steps, which are schematically shown in Figure 2.7: 1) nanoparticle adsorption at the vesicle surface, 2) engulfing of single nanoparticles or groups of particles, 3) entire coverage of the nanopar-

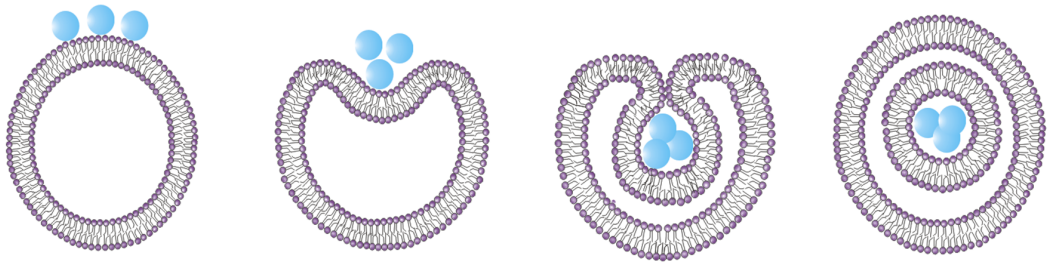

Figure 2.7: *Schematic illustration of the four steps of nanoparticle uptake into PDMS-b-PMOXA polymersome. Details are given in the text. (Used with permission of Wiley from [Jas12b])*

ticles by the membrane, and 4) complete internalization. They have also shown that this process is size and concentration dependent [Jas12c].

It is very remarkable that endocytosis of nanoparticles can be mimicked by an artificial vesicle. This leads to the assumption that the process of nanoparticle uptake is driven by physical parameters only, and no bioactive components like membrane proteins or receptors are needed. In addition, it opens the possibility to study nanoparticle-membrane interactions in a much less complex system than the cell, using very sensitive and noninvasive analytical techniques such as PCS. This minimal model system can also be modified and specialized for further experiments or applications in nanotoxicology research.

2.2 Colloidal Systems

According to IUPAC , a colloid is a molecule or particle dispersed in a medium which is between 1 nm and and 1 μm in diameter [McN97]. The term "colloid" is derived from the greek words κόλλα (*kólla*) and εἶδος (*eidos*), which mean "glue" and "shape" or "form", respectively. In principle, a colloidal system always consists of two phases: a dispersed phase and a continuous phase. Depending on the aggregation states of both phases, colloids can be classified into different categories. In this work, only emulsions (liquid dispersed in liquid) and sols (solid dispersed in liquid) are used. The following sections introduce basic terms of colloidal science, focusing on the self-assembly of amphiphilic block copolymers in water. Furthermore, the stability of colloidal dispersions is discussed.

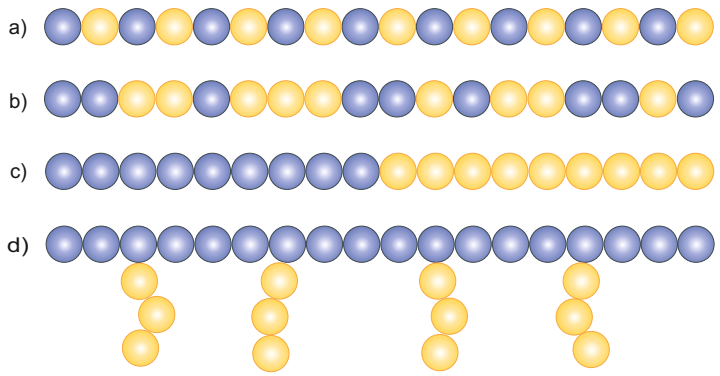

Figure 2.8: *Schematic representation of different copolymer structures: a) alternating, b) statistical, c) diblock and d) graft copolymers. The blue and yellow spheres represent different monomers.*

2.2.1 Block Copolymers

A copolymer is a polymer consisting of two or more different monomer units. For simplification, only copolymers of two different monomers will be described here. Depending on how the two monomers are arranged along the chain, one can distinguish between *alternating copolymers* (regular alternating monomer units), *statistical copolymers* (monomer sequence follows a statistical rule), *block copolymers* (covalently linked homopolymer subunits), and *graft copolymers* (homopolymer subunits grafted on a homopolymer chain). All different possible structures are shown in Figure 2.8. The copolymer composition is the molar ratio of the two monomer units in the copolymer and depends on the reactivity ratios r_A and r_B of monomer A and monomer B, respectively. This is mathematically described by the Mayo-Lewis equation [Odi04].

In this work, only block copolymers have been used. Depending on the number of covalently linked homopolymer subunits, one can distinguish *diblock* ($(A)_n(B)_m$), *triblock* ($(A)_n(B)_m(A)_p$ or $(A)_n(B)_m(C)_p$) and *multiblock* ($[(A)_n(B)_m]_p$) copolymers. Block copolymers can be synthesized by controlled radical polymerization (both reactivity ratios are greater than one), by living polymerization and subsequent addition of the monomers, or by polymerization of the other monomer using a homopolymer block as macroinitiator [Had02]. Here, poly(dimethylsiloxane)-*block*-poly(2-methyloxazoline) copolymer

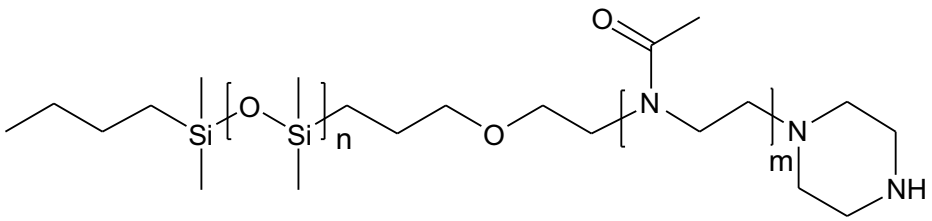

Figure 2.9: *Chemical structure of PDMS-b-PMOXA block copolymer. n and m refer to the degree of polymeraization of the PDMS- and PMOXA-block, respectively.*

(PDMS-*b*-PMOXA) was synthesized by cationic ring-opening polymerization of 2-methyl-2-oxazoline (MOXA) using a triflate-activated poly(dimethylsiloxane) block (PDMS-Otf) as initiator. The chemical structure of PDMS-*b*-PMOXA is shown in Figure 2.9.

Since block copolymers consist of at least two different chemical blocks which might be incompatible but are covalently bonded to each other, they undergo a microphase separation in order to minimize interfacial free energy. Depending on the relative lengths of the blocks, different morphologies were observed in bulk, including spheres of one block dispersed in the second, lamellae or layers of different blocks, hexagonally packed cylinders, gyroids and other bicontinuous structures. The microphase separation can be thermodynamically described by the product of the degree of polymerization n and the Flory-Huggins interaction parameter χ [Lei80].

In this work, *amphiphilic* diblock copolymers have been investigated. Amphiphiles (from Greek αμφις (*amphis*) and φιλία (*philia*), which means "both" and "love, friendship", respectively) are compounds that possess both hydrophilic (water-loving) and lipophilic (fat-loving) properties. Asides from microphase separation in bulk, amphiphilic block copolymers can form various morphologies in solution, since the hydrophilic and the hydrophobic parts will behave differently when placed in a solvent. The way the molecules arrange themselves is determined by the nature of the solvent, the degree of stretching of the core-forming blocks, and the repulsive interactions among the corona-forming chains. Amphiphilic block copolymers possess similar structures as lipids and can self-assemble into equivalent structures.

2.2.2 Self-Assembly Principles

Due to their possession of both polar and nonpolar characteristics, amphiphilic molecules are able to self-assemble into various structures in solution. In this work, only water was used as solvent, and other solvents should therefore be neglected. In very dilute solutions, the entropy of mixing dominates, and molecules are simply dispersed randomly in the solvent. However, dispersing hydrophobic species into water result in a cleavage of hydrogen bonds between water molecules, since hydrophobic molecules are unable of forming hydrogen bonds to their surrounding water molecules. This causes a higher ordering of the water molecules surrounding the solute and results in a significant reduction of entropy. As the concentration of the solute increases, the entropy is further reduced. In order to avoid this energetically unfavorable process, the hydrophobic molecules form aggregates, hence reducing the surface area exposed to water. The resulting entropic penalty of assembling the amphiphilic molecules is less than the alternative entropic penalty of highly ordered water molecules. This is called the *hydrophobic effect* and is the main driving force for the process of amphiphile self-assembly [Isr76, Cha05].

At very low concentrations of the amphiphile, the molecules are either dissolved in the solution or will arrange themselves at the surface of the water such that the hydrophilic part interacts with the water and the hydrophobic part is held above the surface. However, with increasing concentration, the surface becomes completely loaded with amphiphiles and more and more molecules need to be dispersed in water. At a certain concentration of the amphiphile, the formation of aggregates becomes more favorable than further dissolving of amphiphiles in water. This is called the critical micelle concentration (CMC) and is dependent on temperature, pressure, and on the presence and concentration of other amphiphiles [Tan74].

Besides micelles, other structures can also be formed by self-assembly of amphiphilic molecules, e.g. cylindrical micelles, vesicles or planar bilayers (see Figure 2.10). The formed morphologies can be predicted by calculating the molar packing parameter p according to:

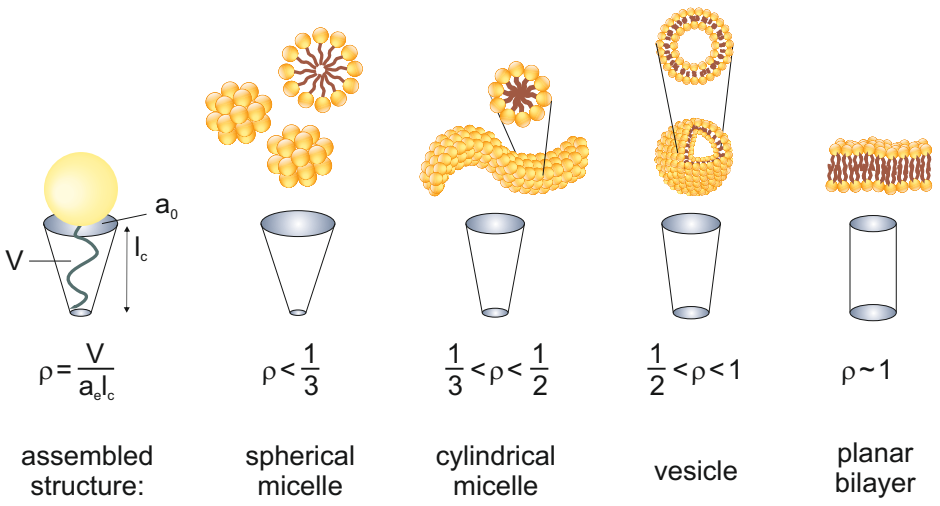

Figure 2.10: *Relationship between packing parameter p and the morphology of self-assembled amphiphiles as predicted by Israelachivili [Isr76].*

$$p = \frac{V}{a_e l_c} \tag{2.1}$$

where V is the surfactant's tail volume, a_e is the equilibrium cross section area of the hydrophobic core per molecule at the aggregate interface, and l_c is the length of the surfactant's hydrophobic chain. p is not constant for a specific surfactant, since the solvent properties, the temperature and the ionic strength of the solvent can affect V, a_e and l_c [Isr76].

Thermodynamically, the formation of micelles can be described either by the mass action model of micellization [Kam84] or by the phase separation model [Elw66]. For the mass action model, one assumes a stepwise and reversible aggregation of each amphiphilic molecule. The equilibrium constants K_A for each aggregation step are calculated by:

$$K_A = \frac{[M]}{[S]^n}, \tag{2.2}$$

where M denotes the aggregates (micelles), S denotes the single surfactant molecules and n is the aggregation number of aggregates. However, monodispersity of all formed micelles is assumed, and summation of all K_A becomes rather complex for high aggregation numbers. According to thermodynamic laws, the free enthalpy of micelle formation

ΔG_M, its enthalpy ΔH_M and its entropy ΔS_M can be calculated. ΔS_M is positive for low molecular weight surfactants, and hence the formation of micelles causes an increase in entropy due to the hydrophobic effect.

In the phase separation model, a micelle is regarded as a separate phase. Under equilibrium conditions, the chemical potential of the surfactant molecules in the aqueous phase μ_W is equal to the chemical potential of the surfactant molecules in the micelle phase μ_M. μ_W is the sum of the chemical standard potential μ_W^0 and of the concentration-dependent term $RT \ln x_T$, whereas x_T is the molar fraction of the single surfactant molecules in water:

$$\Delta\mu = \mu_M + \mu_W^0 = RT \ln x_t \tag{2.3}$$

Under thermodynamic equilibrium conditions, $\Delta\mu = 0$, and the concentration of the single surfactant molecules equates to the critical micelle concentration. According to Tanford [Tan80] and Israelachvilli [Isr76], the chemical potential is composed of three different terms: a tail transfer term, which is responsible for aggregation since the hydrophobic tails avoid contact with water, an interfacial term which promotes the growth of aggregates due to residual contact between water and the hydrophobic tails, and a head term, which limits the aggregate size due to head group repulsion. This model explains the basic features of micellization.

As seen in Figure 2.10, different morphologies can be formed by self-assembly of amphiphilic molecules. The focus of this work is on polymersomes, and hence only the formation of vesicles shall be discussed. The packing parameter (see Equation 2.1) for vesicles is $\approx$ 0.5-1. Therefore, the relative size of hydrophilic to hydrophobic segments must be almost equal. This purely geometrical model is not very accurate in describing the self-assembly of amphiphilic block polymers, because it considers neither the entropy loss during vesicle formation nor the entropy of the polymer chain itself. The resulting structure does not only depend on the geometry of the molecule, but also on the minimization of both the interfacial energy and the loss of entropy of the polymer chains [LM11], making it very difficult to fully predict the required molecular structure to form

vesicles. Nevertheless, it was empirically found that vesicle formation occurs for coil-coil block copolymers if the hydrophilic weight fraction is close to 35% (±10%) [Dis02].

2.2.3 Polymersome Formation

While the mechanism of vesicle formation from block copolymers is still not clear, two different mechanisms are under discussion. In both mechanisms, the initial stage is the formation of spherical micelles in solution, which then either increase in size, leading to the formation of vesicles (*mechanism 1*) or which evolve towards other structures like cylindrical or open-disk micelles (*mechanism 2*). In mechanism 1, the increasing size of the micelles causes water to diffuse into the micelle's interior and the radius of curvature is increased [LM11]. Consequently, vesicles evolve slowly from micelles, and their ability to encapsulate hydrophilic molecules should therefore be low, which was experimentally shown for PEO-*b*-PDEAMA (PEO-*b*-poly(N,N-diethylaminoethyl methacrylate) [Ada08]. In mechanism 2, the initially formed micelles evolve into cylindrical and open-disk micelles upon collision. These disks then slowly deform to vesicles [Une07]. This mechanism has been pre-estimated by computer simulations [Nog01, Yam02, Mar03] and was supported by experimental observations of different transition states from micelles towards vesicles [Che99, Du04]. Monte Carlo simulations as well as experiments on lipid systems indicate that mechanism 2 is preferred over mechanism 1, and it is likely that the mechanism of vesicle formation is the same for both lipids and polymersomes [Ber96, Len02, Len03].

Considering mechanism 2, disk micelles with a line energy $E_l = 2\pi R_d \gamma$ are formed. γ is the line tension and R_d the radius of the disk. Due to the line energy on the edges, disks benefit from closing into vesicles, and a bending energy $E_{\text{bend}} = 8\pi\kappa$, with κ being the bending modulus, needs to be raised. Assuming that the disk radius is double that of the vesicle and the line energy is balanced with the bending energy, the minimal vesicle size R_{min} is:

$$R_{min} = \frac{2\kappa}{\gamma} \tag{2.4}$$

For common values of the line tension ($\approx$ 1 kT/nm) and of the bending modulus for block copolymer bilayers ($\approx$ 40 kT), R_{min} must be larger than 80 nm. The vesicle size also depends on the balance between mixing entropy, which favors a large number of small vesicles, and bending energy, which prefers large vesicles [LM11]. A high polydispersity of the hydrophilic block lowers the curvature energy of the vesicles because the shorter molecules gather along the inner leaflet, whereas the longer ones gather along the outer leaflet [Luo01]. In addition, highly polydisperse block copolymers lead to a decrease in the vesicle size polydispersity.

The previous discussion is only effective at the thermodynamic equilibrium, but vesicles are experimentally often trapped in non-equilibrium (frozen) state, meaning that there is a very low exchange between single molecules and self-assembled structures. Therefore, the actual vesicle size is more dependent on the preparation method and on the successive extrusion processes, making almost all vesicle radii possible.

2.2.4 Stability of Colloids in Dispersion

The stability of colloids in dispersion is determined by the sum of their attractive and repulsive interactions. Attractive forces between small molecules are *van-der-Waals* forces, which are proportional to the inverse seventh power of the distance d between the two molecules. Since the change in the free energy is *force* $\times$ *distance*, the free energy of attraction E_A is proportional to d^{-6}. Repulsive forces originate from the electrostatic interaction between the electron clouds of two approaching atoms or molecules (*Born repulsion*) and the energy of repulsion E_R is proportional to d^{-12}. Hence, attractive forces have a wider range than repulsive forces. The total energy E_t of interaction is the sum of the contributions from attractive and repulsive energies and is usually known as the Lennard-Jones potential (Figure 2.11).

In order to calculate the total free energy of interaction in colloidal dispersions, one would need to sum up the interactions between all molecules of particle A and of particle B. The van-der-Waals interactions between two spheres are different from that between two molecules, and the energy of attraction is then proportional to d^{-1}. Consequently, the attractive forces between colloidal particles have a much longer range than those

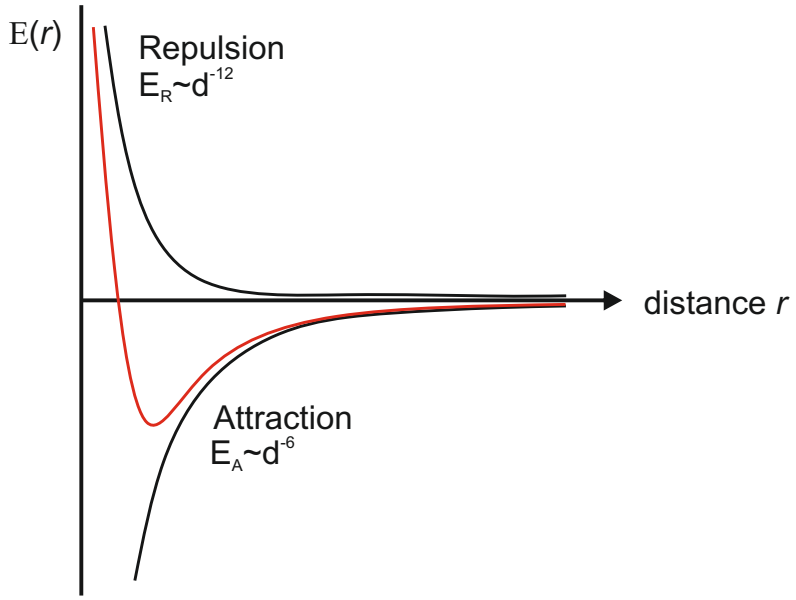

Figure 2.11: *Lennard-Jones Potential (red, potential energy Φ vs. distance d) describing both attractions (d^{-6}) and repulsions (d^{-12}) between uncharged particles.*

between molecules. Depending on the origin of repulsive forces - either electrostatic or steric repulsion - one has to consider different terms. Electrostatic repulsion is based on Coulomb's law but is not applicable here due to the shielding effect of ions around the particle. This *electric double layer* consists of a rigid layer of absorbed counter-ions close to the charged surface and a diffuse layer of non-bound ions at larger distance from the surface (see Figure 3.3 in subsection 3.2.5 (Zeta-Potential Measurements)). It balances the charge on the particle and the electrical potential in the solution then falls off exponentially with distance from the particle surface. The thickness of the double layer depends mainly on the concentration of ions, decreasing with increasing electrolyte concentration. For steric stabilization, when two particles meet, the stabilizing chains on their surfaces will interpenetrate. Osmotic and entropic effects will drive their surfaces apart. Consequently, the magnitude of the repulsion depends on the grafting density of the particle surfaces.

For simplification, it is assumed that the long-range repulsive forces originate from either electrostatic or steric contributions. The total free energy difference ΔG between particles is therefore:

$$\Delta G = \Delta G^{att}(\text{vdW}) + \Delta G^{rep}(\text{Born}) + \Delta G^{rep}(\text{electrostatic or steric}) \tag{2.5}$$

The combination of all interactions to yield the total free energy is known as the *DLVO theory* introduced by Derjaguin and Landau [Der93] and Verwey and Overbeek [Ver47]. Graphically, this can be shown by potential curves for both cases (see Figure 2.12), describing the DLVO potential in relation to the distance d of two particles. At very small distances, the Born repulsion prevents the particles from overlapping. Van-der-Waals attractions cause a primary minimum at small d, which is referred to as coagulation. Once the particles reach this minimum, they are irreversibly agglomerated. At larger distances, the repulsion term causes a primary maximum, which determines the stability of the dispersion. Since the electrostatic repulsion depends on the ionic strength of the medium, the resulting primary maximum is either a high repulsive barrier at low ionic strengths, or no barrier at all at high ionic strengths. For low to intermediate ionic strengths, a secondary minimum may evolve (Figure 2.12a), which is referred to as reversible flocculation. Consequently, one can differentiate three main scenarios:

- For low charged particles in medium or high ionic strength, the attractive forces are dominant for all distances and E_R is always smaller than the particle's thermal energy. This means that there is no energy barrier and hence very fast coagulation of the particles occurs.

- The particle's thermal energy is smaller than both the secondary minimum and the maximum. Depending on E_A and the particle's size, the time needed for coagulation varies. Agglomerates will be formed, which can be redispersed through mixing.

- The particle's thermal energy is larger than the secondary minimum, but smaller than the ernergy barrier. No aggregates will be formed and hence the dispersion is stable.

For steric repulsion, both the repulsive barrier and the depth of the minimum depend on the solvent and on the temperature (Figure 2.12b).

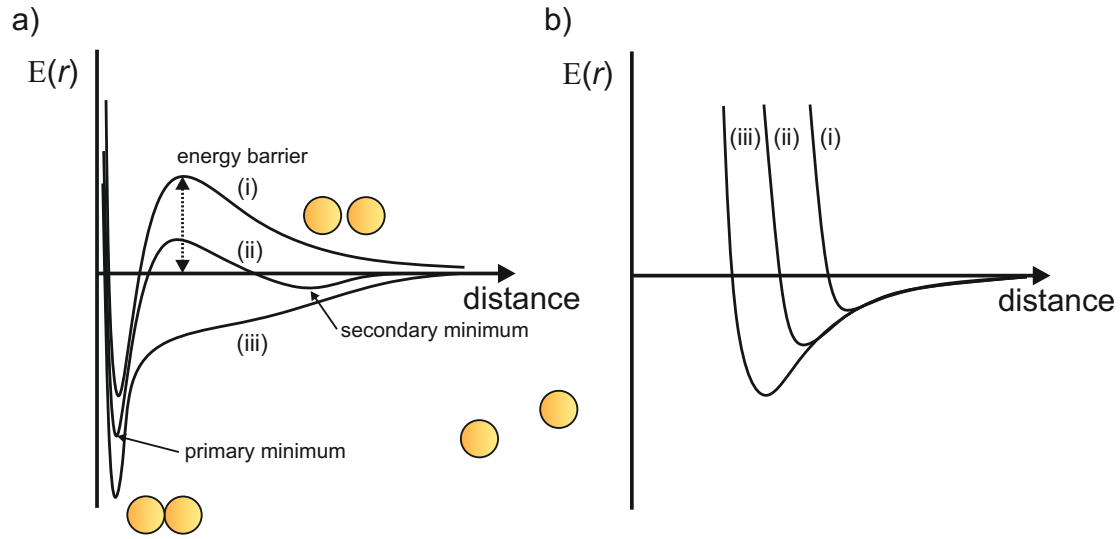

Figure 2.12: *Potential curves for a) electrostatically stabilized dispersions with increasing electrolyte concentration from (i) to (iii), and b) sterically stabilized dispersions with decreasing thickness of the adsorbed layer.*

2.3 Light Scattering of Colloids

In the second half of the 19th century, John Tyndall and Lord Rayleigh performed the first experiments on light scattering, trying to explain the blue color of the sky. While Tyndall thought that sunlight is scattered from dust particles in the atmosphere, Rayleigh concretized that scattering can also occur by gas due to fluctuation of the molecules around a position of equilibrium. He also explained that the amount of scattering is related to the light's wavelength and that therefore, blue light is preferentially scattered in comparison to red light.

Interaction of light with matter can take many forms which can be described by considering that light has both particle and wave character. In order to understand the phenomenon of light scattering, one has to treat light with the classical wave picture. When a laser beam impinges on a sample, it can be considered as an electromagnetic wave oscillating at a given frequency which will interact with the charges of the scattering material. The molecule's charge distribution will be shifted and will therefore emit an electromagnetic wave of the same frequency as the incident light beam, but with

modulated amplitude and phase. This emitted radiation - the scattered light - contains information about the scatterer's size, shape and interactions.

In this section, the very basic principles of light scattering are discussed. A special focus is placed on gold nanoparticles and their characteristic surface plasmons. In addition, dynamic diffusion properties of spherical and non-spherical particles are presented, which are fundamental for performing dynamic light scattering.

2.3.1 Fundamentals of Light Scattering

The fundamentals of classical light scattering theory were developed and extended by Lord Rayleigh, Gans, and Debye. Light is an electromagnetic wave, which is a periodic modulation of electric field strength, and, at right angles, has an associated fluctuating electrical field propagatingd through space at the velocity of light. When light impinges on a material, a dipole moment will be induced by the electric field. The induced dipole $\vec{p}$ is proportional to the incident field $\vec{E}$ and the proportionality constant is called the polarizability α:

$$\vec{p} = \alpha \cdot \vec{E} \tag{2.6}$$

When a particle is subject to an electric field, the particle will be polarized and a dipole moment will be induced. This is the source of the scattering. If the particle is small (R $\approx \lambda/20$), all parts of the particle are subject to the same electric field, and the induced dipole will fluctuate in magnitude. Consequently, an electromagnetic field is produced which radiates light of the same frequency as the incident radiation. In the plane normal to the direction of polarization, the ratio of the scattered intensity (I) to the incident intensity (I_0) of the scattered light at a distance r from its source is:

$$\left(\frac{I}{I_0}\right)_v = \frac{16\pi^4}{r^2\lambda^4}\left(\frac{\alpha}{4\pi\epsilon_0}\right)^2 \tag{2.7}$$

where ϵ_0 is the permittivity of a vacuum and λ is the wavelength of the light. The subscript v indicates that the incident light is vertically polarized with respect to the

observational plane. The polarizability α is dependent on the particle's volume V, ϵ_0 and on both the refractive indices n_0 and n_1 of the medium and of the particle, respectively:

$$3\epsilon_0 \left(\frac{n^2-1}{n^2+2}\right) V \tag{2.8}$$

with $n = n_1/n_0$ and for a spherical particle of radius R with $V = 4/3\pi R^3$. Consequently, for $n_0 = n_1$, α is zero and the scattering intensity also falls to zero. On the other hand, the greater the ratio of the indices, the stronger the scattering. Substituting α and V in Equation 2.7 gives:

$$\left(\frac{I}{I_0}\right)_v = \frac{16\pi^4}{r^2} \cdot \frac{R^6}{\lambda^4} \left(\frac{n^2-1}{n^2+2}\right)^2 cos^2\theta \tag{2.9}$$

To quantify the scattered intensity, one defines the so-called *Rayleigh ratio* at the scattering angle θ, R_θ, which refers to the light scattered by a single particle. For a dilute dispersion, the total scattering is simply the sum of contributions from each individual particle. Thus, Equation 2.9 for a particle dispersion at concentration c is:

$$\frac{I}{I_0} = R_\theta c/r^2 \tag{2.10}$$

R_θ is a function of the particle's volume and hence the particle's radius can be obtained (assuming a spherical shape of the particles). Due to the strong dependence of R_θ on the wavelength ($\propto \lambda^{-4}$), the scattering is strongest for short wavelengths. This accounts for the blueness of the sky and the redness of the setting sun, since the sun light is scattered by molecules in the atmosphere.

So far, all equations are only valid for very dilute particle dispersions, where the particles are spherical and much smaller than the wavelength of the light. For larger particles, not all parts of the particle are subject to the same electric field at the same instant of time. Therefore, light scattered from different parts of the particle is not in phase and interferes at the detector, reducing the intensity of scattering. Consequently, the scattering intensities will be different for different angles. The Rayleigh scattering is modified by a correction factor $P(\theta)$:

$$P(\theta) = 1 - \frac{1}{3}(qR_g)^2 + ... \tag{2.11}$$

with q being the *wave vector* ($q = (4\pi/\lambda)\sin(\theta/2)$) and R_g the *radius of gyration*. Since for zero angle, $\sin(\theta/2) = 0$ and hence $P(\theta) = 1$, the scattering in the backwards direction is decreased compared to Rayleigh scattering (for $\theta = 180°$, $\sin(\theta/2) = 1$ and hence $P(\theta) = 1 - \frac{1}{3}(4\pi R_g/\lambda)^2 + ...$).

For much larger particles ($R/\lambda \approx 1$), the scattering shows a complex dependence on θ and shall not be discussed here. In addition, more concentrated dispersions show multiple scattering effects, which make analysis of the scattering intensity impossible. Consequently, light scattering is possible for rather small particles in dilute suspensions. More details about light scattering as a method in colloidal science is given in subsection 3.2.1 (Photon Correlation Spectroscopy).

2.3.2 Gold Surface Plasmon

In general, a plasmon is a partially or fully ionized gas, but which is neutral in its sum. Correspondingly, in metals, the free flowing cloud of electrons surrounding the metal atoms can also be called plasmon. This plasmon may be described as a collective oscillation of the free electrons around the atomic cores. One differentiates volume plasmons and surface plasmons, depending on where the electron density fluctuations occur. Here, only surface plasmons shall be described. When a plasmonic particle is exposed to light, and consequently to an electromagnetic wave, a dipole is induced in the material due to reorientation of the free charges inside the particle. In order to compensate for the dipole, the free electrons migrate in the material. However, the oscillating light waves lead to a permanent shift in the dipole, forcing the electrons to oscillate at the same frequency as the light. This resonant frequency depends on the size and shape of the plasmonic nanoparticles. For instance, spherical gold nanoparticles (AuNPs) with a diameter of $d \approx 30$ nm have a resonance frequency of $\lambda \approx 450$ nm. Consequently, the blue to green range of the spectrum is absorbed while red light is reflected, resulting in the deep red color of AuNPs dispersions with $d = 30$ nm. With increasing particle size,

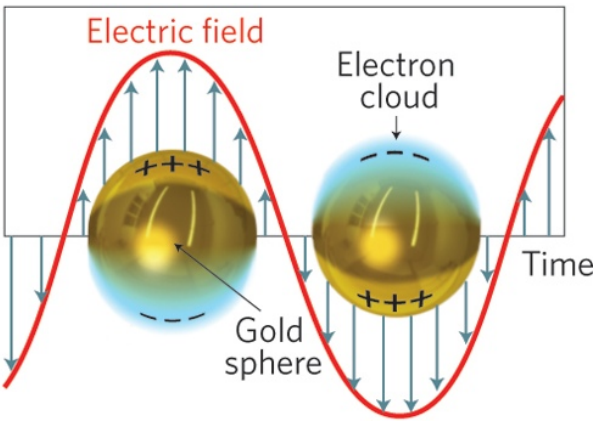

Figure 2.13: *Collective oscillation of electrons with the incident electromagnetic field in a gold nanoparticle (Used with permission of Nature Photonics from [Jua11]).*

the surface plasmon resonance wavelength shifts to higher wavelengths (redshift), causing red light to be absorbed and blue light to be reflected. Thus, such AuNPs dispersions show a purple to blue color. Non-spherical particles, for instance gold nanorods, exhibit anisotropic surface plasmon responses due to the two different axes of the nanorod. Consequently, two plasmon modes are present: The longitudinal resonance mode arising from electrons oscillating along the long axis and a transverse mode associated with transverse electron oscillations. Due to the longer electron path at the long side of the rod, the longitudinal mode is located at higher wavelengths than the transverse. In addition, the extinction of the longitudinal plasmon resonance predominates, and hence gold nanorod dispersions show a green or blue color, depending on the size of the long axis. The size dependence of the surface plasmon can be demonstrated by adding salt to the gold dispersion. Upon reduction of the thickness of the electric double layer (see subsection 2.2.4 (Stability of Colloids in Dispersion)), the nanoparticles aggregate, and the color of the dispersion changes from red to blue or even colorless (resonance maximum in the infrared portion).

Assuming small spherical nanoparticles ($d \leq 25$ nm), the extinction cross-section $\sigma_{ext,sphere}$ can be described by the so-called dipole approximation of Mie theory [Lin99]:

$$\sigma_{ext,sphere}(\lambda) = \frac{9V\epsilon_m^{3/2}}{c} \frac{\epsilon_2(\lambda)}{[\epsilon_1(\lambda) + 2\epsilon_m]^2 + \epsilon_2(\lambda)^2} \tag{2.12}$$

with V being the volume of the particle, c the speed of light, λ the wavelength of the incident light, and ϵ_m the (lambda-independent) dielectric constant of the surrounding medium. $\epsilon_1(\lambda)$ and $\epsilon_2(\lambda)$ are the real and imaginary part of the dielectric function of the particle material, respectively ($\epsilon(\lambda) = \epsilon_1(\lambda) + i\epsilon_2(\lambda)$).

As can be seen from Equation 2.12, σ_{ext} depends on both the dielectric function of the particle's material and the dielectric constant of the medium in which the particle is dispersed. Resonance (maximum of σ_{ext}) occurs when the denominator of Equation 2.12 approaches zero. This is the case at the wavelength λ_{max} for which $\epsilon_1(\lambda) \approx$ -2ϵ_m if $\epsilon_2(\lambda)$ is small. For larger particles (2R $\geq$ 25 nm), σ_{ext} depends also on higher-order multipole modes.

For nanorods, the extinction cross-section $\sigma_{ext,rod}$ can be also described by quasistatic theory, the nanorod has to be approximated as a prolate spheroid [Boh98]:

$$\sigma_{ext,rod}(\lambda) = \frac{k^4}{6\pi} |\alpha|^4 + k \,\mathrm{Im}(\alpha_i) \tag{2.13}$$

with

$$\alpha_i = 4\pi abc \frac{\epsilon_1 - \epsilon_m}{3\epsilon_m + 3L_i(\epsilon_1 - \epsilon_m)} \tag{2.14}$$

where k is the wavevector, α_i is the polarizability of the metal nanocrystal, and L_i is the depolarization factor that relates to one axis, and a, b, and c are the half lengths of the ellipsoid along the three major axes. Consequently, $\sigma_{ext,rod}$ varies with size and shape of the nanorod. If one increases the aspect ratio while keeping the diameter constant, the resonance wavelengths for both transversal and longitudinal plasmon modes will increase. However, for the transversal plasmon, the shift of λ_{max} will only be marginal, whereas λ_{max} of the longitudinal mode will be red-shifted up to several hundred nanometers. This is due to the much higher polarizability of the nanorod at the long axis. In addition, the longitudinal plasmon peak is almost linearly dependent on the aspect ratio [Joh72].

Equation 2.12 and Equation 2.13 show that, in addition to size, the surface plasmon also depends on the refractive index of the surrounding material. This effect was experimentally shown by Underwood and Mulvaney, who dispersed spherical AuNPs with

a mean diameter of 16 nm in different solvents with refractive indices reaching from $n = 1.336$ (water) to $n = 1.583$ (mixture of butyl acetate and CS_2). The observed color changed from red to purple, and the plasmon resonance wavelengths were shifted from 520 nm to 545 nm. They also showed that the color change is reversible upon changing of the refractive index (evaporation of CS_2) and not due to coalescence of the gold [Und94].

2.3.3 Dynamics of Gold Spheres and Nanorods

As discussed in subsection 2.3.2 (Gold Surface Plasmon) above, Au nanospheres and Au nanorods exhibit characteristic UV/Vis absorption spectra. The position of the peak wavelengths yield information about the size and aspect ratio of the particles. A more accurate measure of particle sizes is provided by transmission electron microscopy (TEM). However, no information about nanoparticle grafting can be obtained from TEM, and no information on interaction and/or aggregation in suspensions can be obtained. In contrast, light scattering measurements (photon correlation spectroscopy (PCS)) allow a very accurate determination of the size of spherical particles and also rather reliably predict nanorod lengths and aspect ratios [Gli12, Hag13]. For elongated nanoparticles, a depolarized component of the light scattering signal can be recorded, and hence both translational and rotational diffusion coefficients can be obtained. Consequently, knowing the dynamic properties of nanospheres and nanorods, PCS can be used to determine the size of the particles [Khl08, Cal07].

Colloidal particles diffuse freely in dispersion. This movement is called Brownian motion. The diffusion velocity depends on the particle's shape, size, and on the viscosity and therefore on the temperature of the dispersion. The larger the particle, the slower it will diffuse. The velocity of the Brownian motion is defined by the translational diffusion coefficient, D^{t}. Knowledge of D^{t} allows the calculation of the particles hydrodynamic radius, R_{h}, from the Stokes-Einstein equation [Ein05]:

$$D^t = \frac{k_b T}{6\pi\eta R_h} \tag{2.15}$$

$2 \cdot R_\mathrm{h}$ is the diameter of a sphere that has the same translational diffusion coefficient as the measured colloid. Note that the Stokes-Einstein equation is only valid for spheres and that particle diffusion is more complex for other geometries and hence other equations need to be used.

In principle, Brownian motion consists of two separate movements of the particles: a) particles change their position in space (translational diffusion) and b) change their overall orientation (rotational diffusion). For perfectly spherical particles, rotational diffusion is (almost) not detectable, since the orientation of a sphere is identical for all positions upon rotation. Therefore, diffusion of spherical particles is of only translational nature, and consequently D^t can be directly obtained from the translational relaxation rate $\Gamma_\mathrm{t} = D^\mathrm{t} q^2$. For non-spherical (anisotropic) particles, both translational and rotational diffusion exists, since upon rotation of anisotropic particles, the original configuration is not restored immediately. The rotational diffusion coefficient D^r, which can be derived from $\Gamma_\mathrm{r} = 6D^\mathrm{r} + D^\mathrm{t} q^2$ and $D^\mathrm{t} = (D_{||} + 2D_\perp)/3$, is an average of the two diffusion coefficients along and normal to the rod axis. Analogous to the Stokes-Einstein equation, one can calculate the radius of rotation (R_r from D^r, using the Einstein-Smoluchowski relation [Smo06]:

$$D_r = \frac{k_b T}{8\pi\eta R_r^3} \tag{2.16}$$

In light scattering, both the translational and the rotational motion contribute to the recorded auto-correlation function, which is therefore bimodal. Rotational motion alone can be recorded if the incident laser light is polarized, and a polarizer in front of the detector allows only recording of depolarized scattered light. The correlation function is then only monomodal [Gli12].

For elongated particles, the information obtained from D^t and D^r can be used to calculate the length L and width d of the anisotropic particle, and consequently its aspect ratio $AR = L/d$. Therefore, one can use two different geometrical models of anisotropic particles: straight cylinders [Ort03, Tir84, Tor81] and ellipsoids [Per36]. The theoretical expressions for D^t and D^r are:

$$D_t = \frac{k_B T}{3\pi\eta L} \cdot F(AR) \tag{2.17}$$

$$D_\mathrm{r} = \frac{3k_B T}{\pi\eta L^3} \cdot G(AR) \tag{2.18}$$

with different expressions for $F(AR)$ and $G(AR)$ for straight cylinders and ellipsoids. For straight cylinders,

$$F(AR) = \ln(AR) + 0.312 + \frac{0.565}{AR} - \frac{0.1}{AR^2} \tag{2.19}$$

and

$$G(AR) = \ln(AR) - 0.662 + \frac{0.917}{AR} - \frac{0.05}{AR^2} \tag{2.20}$$

Details for F(AR) and G(AR) are for prolate and oblate ellipsoids can be found in the Appendix.

In principle, both translational and rotational contributions are present in the dynamics of all nanoparticles. However, for noble-metal NPs, the depolarized scattering is strongly enhanced due to their surface plasmons. Therefore, light scattering is a very suitable method for characterizing Au nanospheres and Au nanorods.

3. Experimental Methods

3.1 Materials

This section describes the synthesis of the materials used in this work. The fundamental groundwork for this thesis was the synthesis of a suitable block copolymer for vesicle formation. The synthesis is described in the following experimental section as well as the preparation of vesicle dispersions. Nanoparticle synthesis is also described, although spherical particles were prepared by Sebastian Harms from the group of Prof. Sönnichsen at the University of Mainz. Surface modification was performed both by Sebastian Harms and by myself. Gold nanorods were purchased from Nanopartz^{TM}and NanoSeedz^{TM}and modified by myself. An overview of all nanoparticles used in this work is given in the Appendix.

3.1.1 Blockcopolymer Synthesis

Poly(dimethylsiloxane)-*b*-poly(2-methyloxazoline) diblock copolymers (PDMS-*b*-PMOXA) with different degrees of polymerization were synthezised according to a slightly modified version of the procedure published by Egli *et al.* [Egl11]. The synthesis is based upon an activation of a commercially available PDMS-monocarbinol (PDMS-OH) with defined molecular weight, followed by a cationic ring-opening polymerization of 2-methyloxa"-zoline (MOXA) and a capping reaction in order to determine two different polymer endgroups. The synthetic pathway is given in Figure 3.1.

All reaction steps were carried out under a nitrogen atmosphere. PDMS-OH was dried under vacuum at 60 °C for at least 14 h. 50 mL of dry hexane was added and the solution

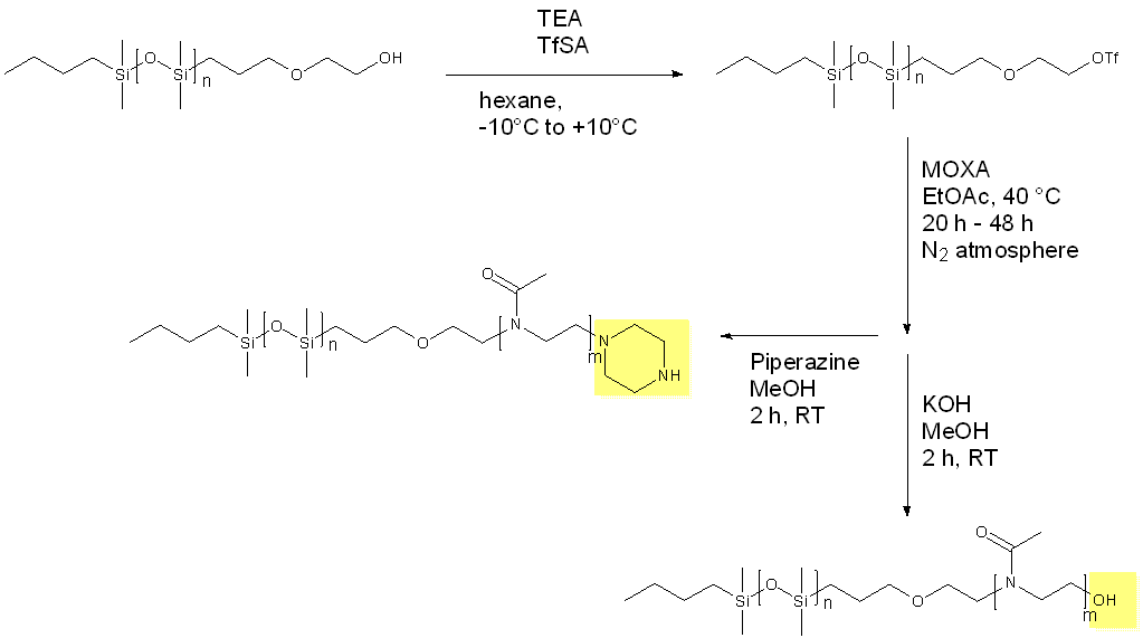

Figure 3.1: *Synthetic pathway of PDMS-b-PMOXA copolymer with two different endgroups, starting from PDMS monocarbinol.*

was refluxed for 24 h in a Soxlhet apparatus filled with a 4 Å molecular sieve. After cooling to room temperature, 0.29 mL (2.08 mmol) of freshly distilled triethylamine was added and the solution was cooled to -10 °C. 0.35 mL (2.08 mmol) of trifluoromethyanesulfonic anhydride in 15 mL of hexane was slowly added over 30 min via a dropping funnel. The solution was slowly allowed to warm to room temperature. Subsequently, hexane was evaporated in vacuum and the residual oil was redissolved in cold hexane. It was separated from triflate salt by careful filtration at 0 °C through a glass frit. The solvent was again evaporated in vacuum, yielding the intermediate product PDMS-OTf.

PDMS-OTf was dried overnight in vacuum. 50 mL of dry ethyl acetate and 5.56 mL (66.0 mmol) of freshly distilled MOXA were added. The reaction mixture was stirred for several hours at 40 °C. The polymerization reaction was stopped after 20 h, 30 h, 40 h or 48 h by cooling to room temperature and adding either 5 mL of 1.0 M potassium hydroxide solution in dry methanol (for -OH endgroup) or 20 mL of 1.0 M piperazine solution in dry methanol (for -NH endgroup). After stirring for an additional 2 h, the solvent was evaporated in vacuum and the remaining glue-like raw product was suspended

in Milli-Q water. The pH was set to neutral and the water was removed by lyophilization. A white and fluffy solid was obtained.

For purification of the polymer, the product was dissolved in ethanol and centrifuged at 4000 rpm for 40 min to separate unreacted PDMS, which is not soluble in ethanol. Subsequently, the ethanol-polymer solution was transferred into an ultrafiltration device (3000 MWCO regenerated cellulose membrane), extensively washed with an ethanol-water mixture for 3 days and finally washed with pure ethanol for one more day. The ethanol was then removed under vacuum and the resulting purified, glue-like block copolymers were characterized by NMR spectroscopy. Characterization data of the obtained products are shown in Table 4.1 in subsection 4.1.1 (Synthesis of PDMS-*b*-PMOXA).

3.1.2 Polymersome Preparation

Polymersomes were formed using the film hydration method. In summary, 5 mg of PDMS-*b*-PMOXA were dissolved in 5 mL of ethanol (p.a. $\geq$ 99.5%, Sigma Aldrich) in a 10 mL round bottom flask. Subsequently, ethanol was evaporated under rotation (80 rpm) at 100 mbar and slightly elevated temperature. The resulting polymer film was dried at $5 \cdot 10^{-2}$ mbar at room temperature for 2 h in order to remove residual solvent. 5 mL of Milli-Q water (Millipore, conductivity $<$ 18.2 MΩ·cm) was added into the flask in order to rehydrate the polymer film. It was stirred overnight at an intermediate stirring speed (300 rpm). In order to homogenize vesicle size, the solution was extruded using an automatic extruder, consisting of a LiposoFast® Basic Extruder (Avestin, Ottawa, Canada) and a motor (homebuild apperature by group of Prof. Schmidt at the University of Mainz). It was extruded through polycarbonate membranes from Avestin of 800 nm and 400 nm pore size (11 times each), and finally through a polycarbonate membrane of 200 nm pore size (31 times) using defined flow rates. Size, shape, polydispersity and membrane thickness of the resulting polymersomes were carefully characterized using static and dynamic light scattering and cryo-TEM.

3.1.3 Nanoparticle Synthesis and Surface Modification

A stock of gold spheres was synthesized according to a literature procedure [Zie11], known as the *seed-growth method*. In general, seed particles were prepared by the standard citrate reduction method [Fre73] and were subsequently grown until the desired size was achieved. In summary, 2.5 mL of a $H[AuCl_4]\cdot 3\ H_2O$ solution (0.2 wt%) in 50 mL of water was heated until boiling and then 2 mL of a preheated sodium citrate solution (1 wt%, containing 0.05 wt% citric acid) was added quickly under vigorous stirring. The solution was kept boiling for 5 min and was then allowed to cool down to room temperature. To 3 mL of the seed solution, 10 mL of a diluted $H[AuCl_4]\cdot 3\ H_2O$ solution (2 mL 0.2 wt% in 8 mL MilliQ water) and 10 mL of a diluted sodium citrate solution (0.5 mL 1 wt% ascorbic acid, 0.25 mL 1 wt% citric acid in 9.25 mL MilliQ water) were added dropwise while vigorously stirring. Directly after the addition, the solution was heated to approx. 75-80°C and maintained at this temperature for about 45 min. After cooling to room temperature, the excess citrate molecules were removed by centrifugation and redispersion of the AuNPs in MilliQ water.

For surface modification, different thiol-capped molecules were used, such as SH-PEG-OCH_3 ($M_W = 736$ Da, $M_W = 2015$ Da, $M_W = 5079$ Da), SH-PEG-COOH ($M_W = 4975$ Da), Cetyltrimethylammonium bromide (CTAB), Mercapto undecanoic acid (MUA) and DNA (T10: Thymine 10-mer with 5'-Thiolink-C6. T40: Thymine 40-mer with 5'-Biotin-C6. Both purchased from Biomers.net), were bound to the particles by overnight incubation at room temperature as described by Hanauer et al. [Han07].

3.2 Characterization Methods

The main method used in this work is *Photon Correlation Spectroscopy*. The basic principles of light scattering are discussed in section 2.3 (Light Scattering of Colloids). This section focuses on the methodology of static and dynamic light scattering. Furthermore, other methods for supporting the findings from light scattering are briefly described in this section.

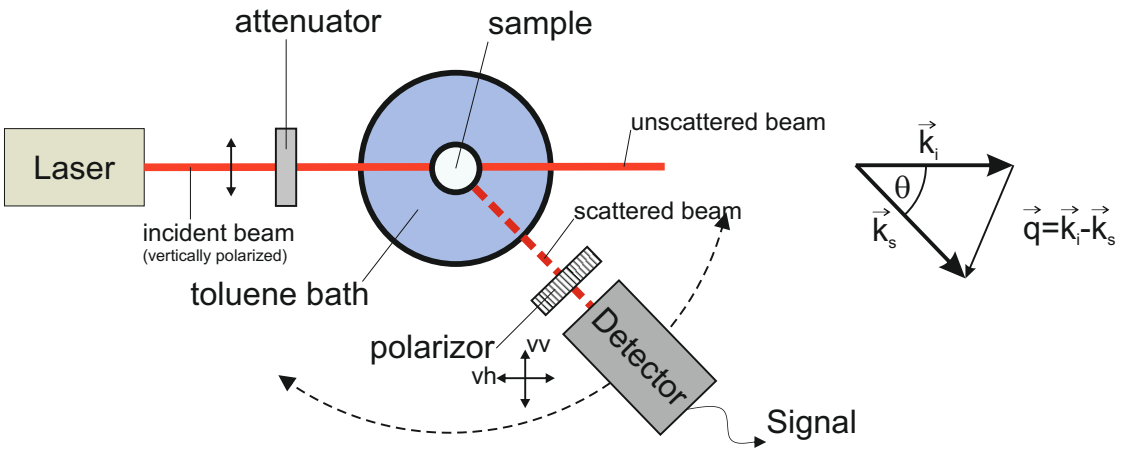

Figure 3.2: *Schematic illustration of a typical light scattering setup.*

3.2.1 Photon Correlation Spectroscopy

Photon Correlation Spectroscopy (PCS) is a well established, non-destructive technique in order to investigate the properties of macromolecules, colloids, and particles in solution or suspensions. In this work, PCS was used to carefully characterize AuNPs, polymeric vesicles, and the mixture of both, for gaining information such as size, molecular weight, diffusion and interactions. The classical physical phenomenon that matter scatters visible light is used for this technique: when a laser beam impinges on a material, the incident electromagnetic radiation of the laser interacts with the polarizable molecules in the sample, thus inducing an oscillating dipole. Consequently, the molecules scatter light. The degree of polarizability is directly related to the difference in refractive index between solute and solvent. The scattered intensity is measured at different angles by a detector. In principle, one distinguishes between static light scattering (SLS) and dynamic light scattering (DLS) . In SLS , one measures the absolute mean intensity of the scattered light, while for DLS, the intensity fluctuations of the scattered light is analyzed. By investigating the frequency shifts of the scattered light, its angular distribution, its polarization and its intensity, one can obtain information about size, weight, shape and molecular interactions in the scattering material.[Sch07] Theoretical fundamentals of light scattering are given in section 2.3 (Light Scattering of Colloids).

A schematic representation of a typical PCS setup can be seen in Figure 3.2. Basically, the instrument consists of a laser light source, an attenuator, a sample cell embedded into an index-matching bath (in our case toluene, which has a refractive index similar to that of glass), a polarizer, a detector, a correlator, and a computer for setup operation and data recording. Initially, the laser beam is passed through an attenuator in order to manually adjust the laser intensity. This intensity is then detected by a photodiode. The laser beam impinges the sample in a glass cuvette, which is located in the toluene bath. After passing through the polarizer, the scattered light is captured by a detector which is mounted on a movable arm which allows to scattered intensities to be measured at different angles. The detected signal is then directed to a correlator, which processes the incoming signal in order to obtain a correlation function. The setup used in this work is able to measure at angles from 12° to 155°. Furthermore, the toluene bath is connected to a thermostate which is able to regulate the temperature of the sample.

The intersection of the incident beam and the scattered beam defines the volume of the sample which is seen by the detector (scattering volume). It is dependent on the scattered angle θ, the wavelength of the beam and the refractive index of the medium. The scattering vector $\vec{q}$ is defined as the difference between the incoming vector of the incident wave $\vec{k_i}$ and the outgoing vector of the scattered light $\vec{k_s}$, which reaches the detector (Equation 3.1).[Chu07]

$$q = k_i - k_s \tag{3.1}$$

The magnitude of q is

$$q = \frac{4\pi\eta}{\lambda} sin\frac{\theta}{2} \tag{3.2}$$

where θ is the angle between k_i and k_s and is called the scattering angle. q increases for increasing scattering angles.

Normally, the incident laser beam is polarized in the direction perpendicular to the plane defined by the experimental setup (source, cell and detector). Therefore, it has

vertical polarization. For spherical and isotropic particles, the scattered light is also vertically polarized. In addition, the detector is adjusted in a vertical position in order to make sure that only vertically polarized scattered light is detected. Consequently, both the incident and the scattered light is in the vertical polarization, and the process is referred to as *polarized* or VV light scattering. If the polarizer is rotated by 90°, the horizontal component of the scattered light is detected. This is referred to as *depolarized* or VH light scattering and is only present for particles with anisotropic shape or anisotropic polarizability.[Sch07]

Static (SLS) and dynamic (DLS) light scattering experiments were performed using an ALV/LSE-5004 goniometer/correlator setup using lasers with two different wavelengths $\lambda = 632.8$ nm (HeNe laser) and $\lambda = 532$ nm (Compass 215M, Coherent, Santa Clara, CA). An avalanche photodiode was used as detector. The normalized light scattering intensity autocorrelation functions were recorded over a broad time range of (10^{-7}-10^{3} s) and an angular range from 25° to 150° corresponding to a scattering vector $q = 5.73 \cdot 10^{-3} - 2.56 \cdot 10^{-2}$ nm^{-1} (red laser) or $q = 6.80 \cdot 10^{-3} - 3.04 \cdot 10^{-2}$ nm^{-1} (green laser). All measurements were conducted at a constant temperature $T = 20$ °C. Cylindrical silica glass cuvettes (Hellma, inner diameter Ø = 10 mm) had been cleaned before use with acetone in a Thurmont-apparatus (details are given in the Appendix).

3.2.1.1 Static Light Scattering

In static light scattering (SLS), the intensity I_s of the scattered light is measured. For ideal gases, Rayleigh described I_s as proportional to the intensity of the incident light beam I_0 and to λ^{-4}:

$$I_s = \frac{8}{3}\pi I_0 \left(\frac{2\pi}{\lambda}\right)^4 \alpha^2 \tag{3.3}$$

α is the polarizability of a molecule or particle and can be expressed as:

$$\alpha = \frac{2nM}{4\pi N_A}\frac{\partial n}{\partial c} \tag{3.4}$$

where n is the refractive index of the solution and $\frac{\partial n}{\partial c}$ is the refractive index increment and needs to be determined by interferometric measurements.

The intensity of the scattered light is measured at different angles, and therefore it is dependent on q. In addition, I_s depends on specific parameters of the PCS apparatus such as the intensity of the incident laser beam and the distance between detector and sample. In order to avoid these dependencies, the so called Rayleigh ratio R_θ is used. R_θ is proportional to $I(q)$ but is independent of instrumental effects:

$$R_\theta = \frac{I_{sample} - I_{solvent}}{I_{toluene}} \cdot RR_{toluene} \tag{3.5}$$

$RR_{toluene}$ is the absolute scattering intensity of toluene (toluene bath) at $\theta = 90°$ and at $T = 20$ °C at $\lambda = 633$ nm. Its value is $1.355 \cdot 10^{-5}$ cm^{-1}.

For vertical polarized incident laser light, concentration c and molar mass M of the dissolved material are related to the Rayleigh ratio via

$$R_{VV}(q) = \frac{4\pi^2 n^2}{N_A \lambda^4} \left(\frac{\partial n}{\partial c}\right)^2 cM = K_o cM \tag{3.6}$$

where K_o is the optical constant with:

$$K_o = \frac{4\pi^2 n^2}{N_A \lambda^4} \left(\frac{\partial n}{\partial c}\right)^2 \tag{3.7}$$

Including a power series to Equation 3.6, one can write:

$$\frac{K_o c}{R_{VV}(q)} = (\frac{1}{M} + 2A_2 c + 3A_3 c^2 + ...) \tag{3.8}$$

where A_2 and A_3 are the second and third virial coefficients [Ter02], giving information about the interactions between the colloidal particles.

Equation 3.6 is only valid for very diluted solutions. However, the scattering intensities of very diluted solutions are very weak and therefore difficult to capture. Consequently, measurements need to be performed in concentration areas where interference occurs. During data evaluation, it is necessary to extrapolate to $c = 0$. In addition, for particles

or molecules larger than $\frac{\lambda}{20}$, the scattered light interferes at all scattering angles but $q = 0$. Therefore, the scattering intensity needs to be extrapolated to the zero angle.

3.2.1.2 Dynamic Light Scattering

In general, colloids randomly diffuse in diluted solutions due to Brownian molecular motion. Therefore, when incident light is scattered by a moving particle or macromolecule, the scattering intensity is not constant over time, and its frequency will be shifted due to the *Doppler* effect. This means that the frequency of the scattered light will be slightly higher or lower than that of the original incident light, depending on whether the particle moves towards or away from the detector. This shift in frequency is correlated to the speed of the colloids in motion. In comparison to SLS, where the average scattered intensity $I(q,t)$ is measured, the fluctuating pattern is important for DLS measurements. Therefore, the normalized intensity-intensity time correlation function $G(q,\tau)$ is recorded, which compares the scattering intensity I at a certain time t with the scattering intensity at a later time $t+\tau$ at a defined scattering angle: [Bro93, Ber00]

$$G(q,\tau) = \frac{\langle I(q,t)I(q,t+\tau)\rangle}{\langle I(q,t)^2\rangle} = A(1+\beta|C(q,\tau)|^2) \tag{3.9}$$

A ($\langle I(q,t)I(q,t)\rangle$) is the measured baseline, β is a coherence factor which depends on the laser beam and experimental setup, and $C(q,\tau)$ is the normalized electric field-field time correlation function. In idealized condition, $\beta = 1$ (perfect coherence).

As soon as the measured intensities at time t+τ no longer correlate to the intensities at time t, the autocorrelation reaches zero. Therefore, the correlation function indicates how far a particle moved within the time τ. The smaller a colloid, the faster it moves, and hence the correlation function decays faster, and vice versa. The decay of the autocorrelation is described by an exponential decay function (Equation 3.10). $C(q,t)$ includes both translational and rotational diffusion as well as internal motions:

$$C(q,t) = A \cdot e^{-\Gamma t}\left[1 + \sum_j B_j \cdot e^{-t/\tau_j}\right]\left[1 + C \cdot e^{-t/\tau_c}\right] \tag{3.10}$$

The first term expresses the translational diffusion, the second describes the rotation about the jth molecular axis, and the third term covers internal motion. A, B and C are constants defining the magnitude of each motion. However, for small, monodispers spheres, only translational diffusive motion is considered, such that

$$C(q,t) = A \cdot e^{-\Gamma t} \tag{3.11}$$

Virtually, Γ is the line-width. For low concentrations and low values of q, $\Gamma = D^t q^2$. This is used to calculate the translational diffusion coefficient D^t, which is in turn related to the radius of hydration R_h (for spherical particles) by the Stokes-Einstein equation [Ein05] (Equation 3.12).

$$R_h = \frac{k_B T}{6\pi\eta D_t} \tag{3.12}$$

So far, rotational diffusion and internal motion have been neglected. If the shape of a molecule or a particle is anisotropic, its scattering is dependent on its orientation. Light scattered from different parts of the particle may lead to a certain amount of destructive interference. For ellipsoids or rigid rods and a vertically polarized incident laser beam (V) and vertically polarized scattered light (V), rotational diffusion needs to be added to $C(q,t)$.

$$C_{VV}(q,t) = A \cdot e^{-q^2 Dt}(1 + B \cdot e^{-6D_r t}) \tag{3.13}$$

For vertically polarized incident light (V) and horizontally polarized scattered light (H), $C(q,t)$ is

$$C_{VH}(q,t) = A \cdot e^{-q^2 Dt - 6D_r t} \tag{3.14}$$

The rotational diffusion coefficient D^r can be determined from the second exponential decay. D^r can also be determined for isotropic particles when the polarizability of the scattering species is anisotropic. In that case, a small component of the scattered light is polarized in a direction perpendicular to that of the normal scattering.

Since diffusion is dependent on temperature T and viscosity η, it is important to keep T and η constant during DLS measurements. In addition, the investigated particles should neither float nor sediment during measurement in order to investigate the self-diffusion of particles only. Additionally, the concentration of the analyzed samples should be very low in order to avoid multiple scattering.

3.2.1.3 Data Evaluation

Data evaluation of the DLS experiments was performed by using the stretched single or double exponential Kohlrausch-Williams-Watts (KWW) [Yos01, Wil70] functions or the CONTIN algorithm [Pro82, Esq02]. The KWW method assumes that for single or double non-exponential decays, the computed relaxation functions $C_{single}(q,t)$ and $C_{double}(q,t)$ can be represented by:

$$C_{single}(q,t) = a_{single} exp[-(t/\tau)^{\beta}] \tag{3.15}$$

and by:

$$C_{double}(q,t) = a_{double_1} exp[-(t/\tau_1)^{\beta_1}] + a_{double_2} exp[-(t/\tau_2)^{\beta_2}], \tag{3.16}$$

respectively. τ is the "average" relaxation time of the corresponding decay and β ($0 \leq \beta \leq 1$) is a measure of the width of the distribution of retardation times.

A method for analyzing $C(q,t)$ of more polydisperse samples (and hence no single exponential decay of $C(q,t)$) is using the CONTIN algorithm. It is based on the inverse Laplace transform of $C(q,t)$:

$$C(q,t) = \int_0^{\infty} G(\Gamma) e^{-\Gamma t} d\Gamma \tag{3.17}$$

For analytically separating two particle populations, their sizes should differ from each other by at least a factor of 4.

3.2.2 (Cryogenic-)Transmission Electron Microscopy

Transmission electron microscopy (TEM) was used in order to characterize size and shape of gold nanoparticles. TEM was also used for vesicle characterization (size, shape and membrane thickness) and for visualizing the interactions of vesicles and nanoparticles. However, since polymersomes are a very soft material and would collapse during normal TEM sample preparation, cryo-TEM was required. In cryo-TEM, aqueous solutions of the sample are vitrified at cryogenic temperatures. In addition, the TEM machine needs to be cooled down to T = -172 °C in order to keep the vitrified samples stable.

Sample prepartation and measurements were performed by Max Bernhardt [Ber14]. For cryofication of the samples, 3.5 µL of the aqueous sample solution was placed onto Quantifoil grids (R2/2, Cu-mesh 300). The grid was blotted with a Vitrobot^{TM} Mark II system (FEI, USA). Excess liquid of the sample was blotted with a Whatman filter paper, and the grid was subsequently plunged into liquid ethane. The grid was transferred into a JEOL 1400 transmission electron microscope, operating at 120 kV, and imaged at cryogenic temperatures (-172 °C). TEM micrographs were processed using ImageJ 1.45s software.

Generally, electron microscopy can be seen as an analogous to light microscopy. Instead of light waves in the visible range, electron microscopes use electron beams. Therefore, the maximal resolution is determined by the wavelength of the electron beam source and is in the nanometer range. In TEM, the electron beam is transmitted through the sample and the scattered electrons are detected by a lens. It is important that the electron beam as well as the sample are in high vacuum in order to avoid any collision with gas atoms [Rei08]. In contrast to normal TEM, cryo-TEM samples as well as the setup must be cooled to very low temperatures.

3.2.3 UV/Vis Spectroscopy

UV/Vis spectroscopy was performed in order to determine size, shape and concentration of pure Au nanoparticles and in order to investigate nanoparticle uptake into polymersomes. In metal nanoparticles, the absorption bands are related to the diameter

and aspect ratio of the material as well as to its chemical surrounding (refractive index) due to plasmonic resonance (see subsection 2.3.2 (Gold Surface Plasmon). Since the excitation of the Au nanoparticle's plasmons appears in the visible range of the electromagnetic spectra, UV/Vis spectroscopy is a very suitable method for characterizing Au nanoparticles and its complexes.

A UV/Vis spectrometer consists of a light source, a sample holder, a monochromator, and a detector. The liquid samples are typically placed in a cuvette made of quartz glass, transparent to UV, visible, and near infrared light. The intensity of light passing through a sample and passing through a reference is compared. The reference beam intensity is taken as 100% transmission, and the spectra of the absorbing sample is correlated to that value.

In this work, the absorption spectra of various Au nanoparticles were measured, using pure water as a reference. All UV/Vis measurements were recorded on a PerkinElmer LAMBDA 25 UV/Vis spectrometer.

3.2.4 Single-Particle Polarization Anisotropy Measurements

The symmetry of noble-metal nanoparticles can be revealed by single-particle polarization anisotropy (PA) measurements. For studying individual particles, one needs to be able to distinguish single particles in the far field by using a conventional microscope, and hence very diluted solutions of the sample are needed. Due to surface plasmons (see subsection 2.3.2 (Gold Surface Plasmon)), an enhanced electromagnetic field is present around noble metal particles. These plasmons are excited by a white light source. Upon decay, the plasmons in turn emit light which is collected using a conventional microscope. A rotatable polarization filter is placed before the camera, and the wavelength-dependent scattering intensity $I(\theta, \lambda)$ is recorded as a function of the polarization angle θ. The polarization anisotropy $PA(\lambda) = (I_a - I_b)/(I_a + I_b)$ can be calculated from the unequal intensities of scattered light which is polarized parallel either to the major (I_a) or to the minor (I_b) particle axis.[Sch08]

Polarization Anisotropy measurements were carried out by Andreas Henkel and Sebastian Harms in the group of Prof. Sönnichsen at the University of Mainz. An optical

microscopy system was used. This is based on a motorized inverted microscope equipped with a piezo scanning stage, a z-piezo, a spectroscopy system, and an autosampler. Self-made flow cells composed of two microscope cover slips were used. All components were controlled by a central MATLAB-based software. A spectral precision for the plasmon peak of 0.3 nm was achieved by refining the exact nanoparticle position before each measurement. The polarization dependency was investigated by inserting a polarization filter in the detection light path. The spectra were acquired in 15° movements from 0° to 180°.

3.2.5 Zeta-Potential Measurements

The zeta-potential measurement determines the electric potential at an interface between two phases (liquid-liquid or, more often, solid-liquid). Usually, in simple electrolyte solutions, (ionic) charges are randomly distributed. However, this is not the case at interfaces. Usually, the two sides of the interface are oppositely charged. This can be due to surface charges originated from dissociable groups (-COOH, -NH_2, -piperazine) or specific adsorption of ions on a surface. This charge accumulation at an interface leads to the formation of an electrochemical double layer.

Charged colloids in solution are surrounded by oppositely charged ions, which form a defined layer around the particle's surface (see Figure 3.3). This layer consists of a tightly adsorbed layer (*Stern* or *Helmholtz layer*) very close to the interface, and a more diffuse layer (*Gouy Chapman layer*) further away from the interface. The Helmholtz layer can be divided into the inner and outer Helmholtz layer (IHL and OHL, respectively). Within the Helmholtz layer, the electric potential decays linearly in the IHL and reaches a minimum Ψ_i, then increases in the OHL until the Stern potential Ψ_S is reached. In the diffuse layer, the electric potential decays exponentially, approaching zero with increasing distance to the particle.[Dör02]

When an electric field is applied to a colloid suspension, the colloids will move towards the opposite charged electrode, accompanied by their Helmholtz layer and partially by the diffuse layer. During this flow, the diffuse layer is sheared off. The potential at the slipping plane is called zeta-potential, ζ.

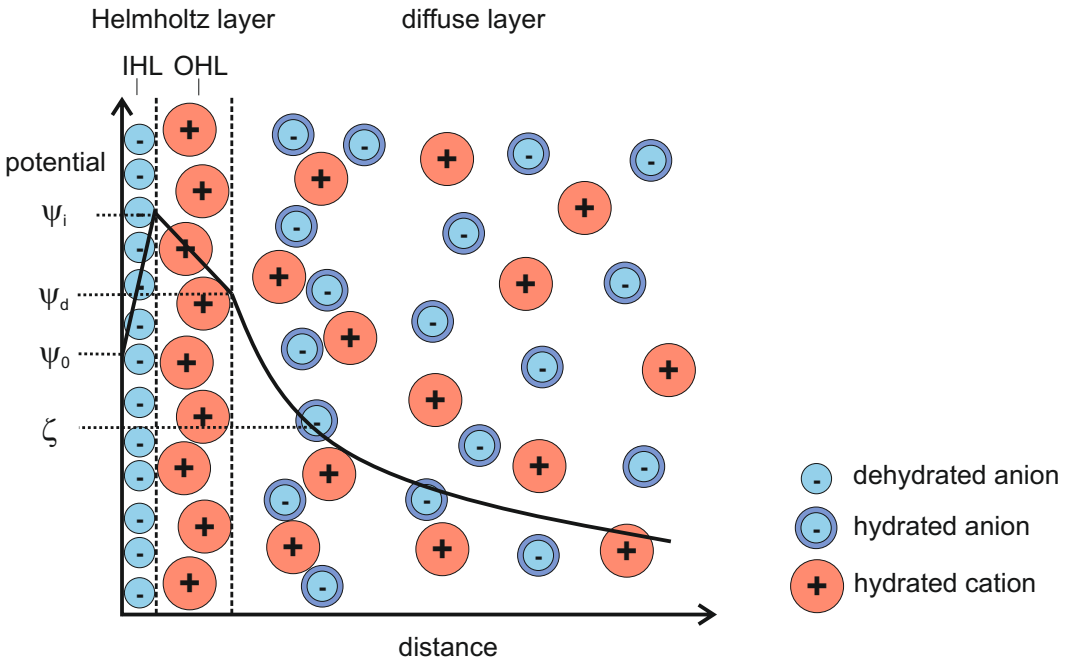

Figure 3.3: *Schematic representation of the electric double layer.*

The zeta-potential can be measured by applying an electric field across the sample solution. Consequently, charged colloids will migrate towards the oppositely charged electrode. The zeta potential is proportional to the particle's velocity and can be calculated by using the equation by von Smoluchowski (Equation 3.18) [Hun81, Dör02]:

$$\zeta(mV) = \frac{6\pi\eta_0\nu_w}{\varepsilon E} \tag{3.18}$$

with ν_w being the electrophoretic mobility, η_0 the solution viscosity, ε the dielectric constant of the medium, and E the strength of the electric field. Equation 3.18 is only valid for spherical, non-conductive and non-deformable colloids at low particle concentration.

The zeta-potentials of nanoparticles and polymersomes in aqueous solutions were determined by using MALVERN Zetasizer Nano Z.

4. Results and Discussion

4.1 Blockcopolymer Synthesis and Vesicle Formation

Synthesis of the amphiphilic block copolymer PDMS-*b*-PMOXA and successive vesicle formation was recently described by Egli *et al.*[Egl11]. Jaskiewicz *et al.* demonstrated that these polymeric vesicles can be used as a minimal cell model in order to study the uptake process of nanoparticles into polymersomes [Jas12b]. In this work, PDMS-*b*-PMOXA molecules with varying hydrophilic block lengths were synthesized. The influence of the PMOXA block lengths on the vesicle formation ability and on the properties of the formed polymersome membrane was studied. It was assumed that the mechanical properties of the membrane would be dependent on the membrane thickness and therefore on the block lengths of the diblock copolymer. Although the synthesis of PDMS-*b*-PMOXA was already described in the literature, obtaining a polymer which forms spherical vesicles was rather difficult. Nevertheless, successful synthesis of PDMS-*b*-PMOXA was crucial for this work since it is the basis for the subsequent investigation on particle uptake into polymersomes. This section describes the successful synthesis of PDMS-*b*-PMOXA with varying PMOXA block lengths and the careful characterization of the formed polymersomes by static and dynamic light scattering (SLS, DLS) as well as cryogenic transmission electron microscopy (cryo-TEM). Furthermore, it is shown that the size and polydispersity of the vesicles can be easily controlled by an automatic extrusion process.

4.1.1 Synthesis of PDMS-b-PMOXA

PDMS$_n$-*b*-PMOXA$_m$ was synthesized by sequential ring-opening polymerization. Experimental details can be found in subsection 3.1.1 (Blockcopolymer Synthesis). n and m refer to the number-average degree of polymerization of the hydrophobic PDMS block and hydrophilic PMOXA block, respectively. The polymerization reaction time was adjusted in order to obtain different PMOXA block lengths, and hence different values for m. Since the PDMS block is used a a macro initiator, its length is fixed and cannot be adjusted. Here, n is $\approx$ 65, resulting in a molecular weight (M_n) of $\approx$ 5000 g/mol for the PDMS block. According to GPC analysis, the polydispersity of the PDMS precursor is $\approx$ 1.1 and therefore very low. For each PMOXA block length m, the polymerization reaction was terminated using either piperazine or KOH, resulting in two different endgroups (-OH for hydroxyl and -NH for piperazyl). The resulting block copolymers were analyzed by ^{1}H-NMR spectroscopy and their molecular weights were estimated by integration, using characteristic methyl signals of PDMS as a reference. GPC did non yield reliable results because of strong interactions between the PMOXA block and the column. Results are summarized in Table 4.1.

Table 4.1: *Specification of different PDMS-b-PMOXA batches, with n and m referring to the number-average degree of polymerization of the hydrophobic and hydrophilic block, respectively. The molecular weights of the samples with piperazyl endgroup are shown.*

Sample	n [-]	m [-]	$M_n^{1H\text{-}NMR}$ [g/mol]
BC-20h	65	13	6243
BC-30h	65	15	6413
BC-40h	65	17	6583
BC-48h	65	19	6753
BC-65h	65	21	6923

4.1.2 Vesicle Formation by Extrusion

Vesicle formation by extrusion using an automatic extruder is described in subsection 3.1.2 (Polymersome Preparation). Due to the very low glass transition temperature of PDMS-*b*-PMOXA ($T_g \approx -124$ °C), the polymersomes are flexible at room temperature and can be adjusted and homogenized in their final size by forcing the polymer dispersion through filters with defined pore sizes. In the first two extrusion steps, the dispersion was prefiltered through a 800 nm and a 400 nm pore size membrane in order to downsize large structures and to improve the homogeneity of the size distribution of the final suspension. For polymersomes larger than the membrane pores, the vesicles need to deform to pass through the pore, and a breaking and resealing of the polymersome membrane occurs. In the final extrusion step, the polymersomes were repeatedly cycled through a 200 nm pore size filter, and polymersomes with a mean diameter of 220-260 nm were yielded. The polymersome diameter and their homogeneity depend on the exact pore size of the filter, on the extrusion speed, and on the number of repeating cycles. Here, polymersomes with average mean diameter of $\approx$ 250 nm were desired, so the pore size of the final filter membrane was 200 nm always. The size of the resulting polymersomes was determined by PCS.

The influence of the extrusion speed and of the number of repeating cycles on the vesicle size and polydispersity was investigated. Therefore, 10 mL of a polymersome dispersion (NH40) were prepared and extruded 11 times through a 800 nm and a 400 nm pore size membrane. Subsequently, 1 mL of the polymersome dispersion was extruded through a 200 nm pore size filter at one out of three different speeds (volumetric flow rates) and at either 15 or 31 repeating cycles. Figure 4.1a shows the Guinier plots for 31 repeating cycles at three different volumetric flow rates. It can be seen that the polydispersity decreases with increasing speed (reduced kink in the Guinier plot at high q^2) and that the size of R_g decreases (lower slope), although the difference between speed 6 (correlates to a volumetric flow rate of 70 μL/s) and speed 10 (115 μL/s) is marginal. Generally, a more homogeneous size distribution is obtained for 31 repeating cycles than for only 15 repeating cycles (Table 4.2, Guinier plots not shown). The obtained radii of gyration and radii of hydration, R_g and R_h respectively, are shown in Figure 4.1b. The

Table 4.2: *Characteristics of vesicles (Radius of gyration R_g, hydrodynamic radius R_h, and structure parameter ρ) obtained from extrusion at different speeds and number of extrusion cycles.*

extrusion speed	extrusion cycles	R_g [nm]	R_h [nm]	ρ
3	15	126.3 ± 3.5	146.2 ± 9.6	0.86 ± 0.07
3	31	126.3 ± 2.7	137.9 ± 4.3	0.92 ± 0.05
6	15	124.5 ± 1.5	126.1 ± 4.5	0.99 ± 0.05
6	31	128.0 ± 1.4	126.9 ± 2.8	1.00 ± 0.01
10	15	125.3 ± 2.6	137.5 ± 6.9	0.91 ± 0.06
10	31	122.3 ± 1.2	126.5 ± 3.5	0.97 ± 0.02

structure parameter $\rho = R_g/R_h$ depends on the morphology of the dispersed structures in solution and is ≈ 1 for all samples, which is characteristic for vesicles [Wu96]. Although R_g and R_h are almost similar for speed 6 and speed 10, the errors for speed 6 are lower for both 15 and 31 repeating cycles. The vesicles extruded with speed 3 (35 μL/s) are generally larger than the vesicles extruded at higher speeds, they exhibit larger errors, and ρ is significantly smaller than 1. Therefore, it is assumed that for very low extrusion speed, no monodisperse vesicles are formed. This may be due to the fact that at low volumetric flow rates, the vesicles are not completely broken and resealed upon extrusion through the membrane pores. Since the polymersomes are very soft and flexible, they can deform to pass through the membrane and unfold to their larger size upon release from the pores. For higher extrusion speeds, the vesicles are broken and forced to adopt the size of the membrane pores. The more often they are extruded through the membrane, the more monodisperse they become. However, if they are pressed through the pores too fast, polydispersity increases again since also smaller vesicles are formed. Therefore, the most monodisperse and spherical polymersomes were obtained at medium speed (speed 6) and at high repeating units. Later vesicle formation by extrusion was always performed at medium speed using 31 repeating cycles for extrusion.

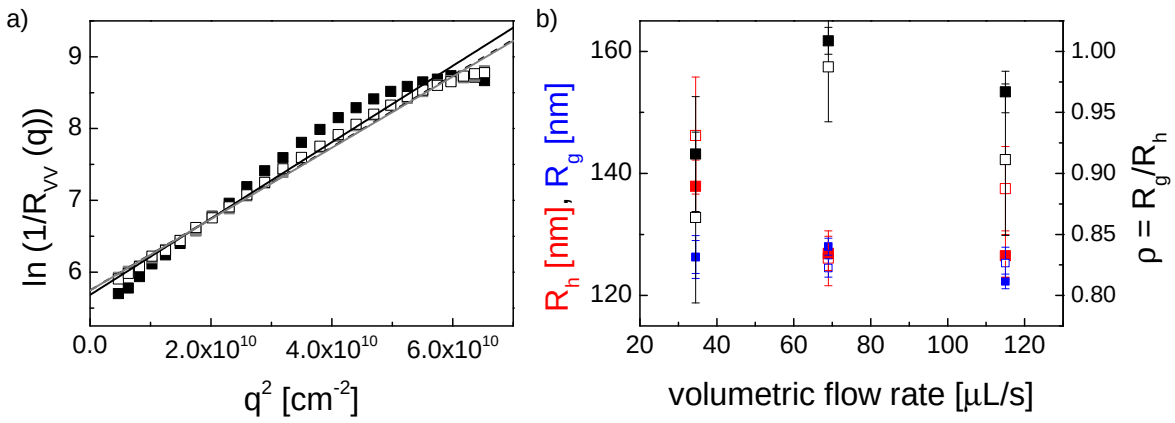

Figure 4.1: *a) Guinier plots of polymersomes obtained from extrusion at speed 3 (black), speed 6 (gray) and speed 10 (open symbols) for 31 repeating cycles. b) Calculated R_g (blue) and R_h (red) from PCS data as well as the structure parameter ρ (black) vs. volumetric flow rate for 15 repeating cycles (open symbols) and for 31 repeating cycles (filled symbols).*

4.1.3 Vesicle Characterization by PCS and cryo-TEM

The previously formed polymersomes needed to be characterized in terms of their shape, size, membrane thickness and mechanical properties. It is focused on the characterization by photon correlation spectroscopy, using cryo-TEM as an additional techniques to obtain a concrete picture of the polymersomes. Complete PCS characterization was performed for all different block copolymer samples from Table 4.1. Sample NH40 was chosen as standard vesicle system for all upcoming experiments, and hence all shown graphs are based on this sample if not stated otherwise.

4.1.3.1 PCS Analysis

PDMS-*b*-PMOXA polymersomes were investigated by both static and dynamic light scattering (SLS and DLS, respectively). SLS was used to determine the radius of gyration R_g of the vesicles, their apparent molecular weight $M_{w,app}$, and the polydispersity PDI of the system. The absolute Rayleigh intensity $R_{VV}(q)$ plotted vs. q is shown in Figure 4.2a (open circles). $R_{VV}(q)$ was fitted by a form factor represented by Equation 2 in the appendix with $R = 102$ nm and $PDI = 1.08$ for the standard vesicles NH40 (represented

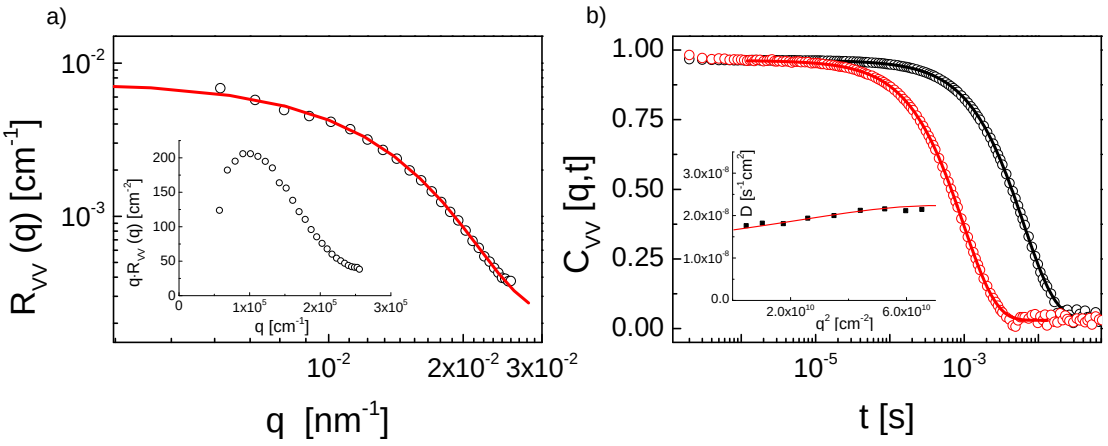

Figure 4.2: *a) Absolute Rayleigh intensity R_{VV} vs. scattering wave vector q for $c = 0.05$ g L^{-1}. The solid lines represents the fit using equation Equation 2. η=0.00115, b) Relaxation functions [C_{VV}(q,t)] for a dilute ($c = 0.04$ gL^{-1}) aqueous suspension of polymersomes at the scattering wave vectors $q = 1.01 \times 10^{-2}$ nm^{-1} (black symbols) and $q = 2.29 \times 10^{-2}$ nm^{-1} (red symbols). The solid lines indicate the theoretical representation of the experimental functions. The translational diffusion coefficient D^t vs. q^2 is shown in the inset.*

by the solid line in Figure 4.2a. For the fit, the thickness d of the membrane was assumed to be $d = 16$ nm and the viscosity of the sample was assumed to be $\eta = 1.15{\cdot}10^{-3}$ Pa·s. R_g was calculated from the slope of the Guinier plot, yielding $R_g = 128.0 \pm 1.4$ nm. R_h was determined from DLS (see below) to be $R_h \approx 128$. The structure parameter $\rho = R_g/R_h \approx 1$ indicates the vesicular shape of the polymersomes. The agreement between SLS and DLS data is very good. The obtained radius R from the form factor fit is smaller than R_h obtained from DLS, because R_h is the hydrodynamic radius and is therefore always larger than the actual size of the particle due to its solvation shell of water molecules, which surrounds the vesicle and diffuses at the same rate.

The weight average apparent molecular weight M_{app} of the vesicle was determined via both an Ornstein-Zernicke and a Debye representation (Figure 4.3) of the scattering data. It was assumed that the very low concentration $c = 0.0365$ g L^{-1} is already low enough to exclude concentration dependence of the scattering data. The refractive index increment dn/dc of the polymersomes was determined from sample BC-65h-NH

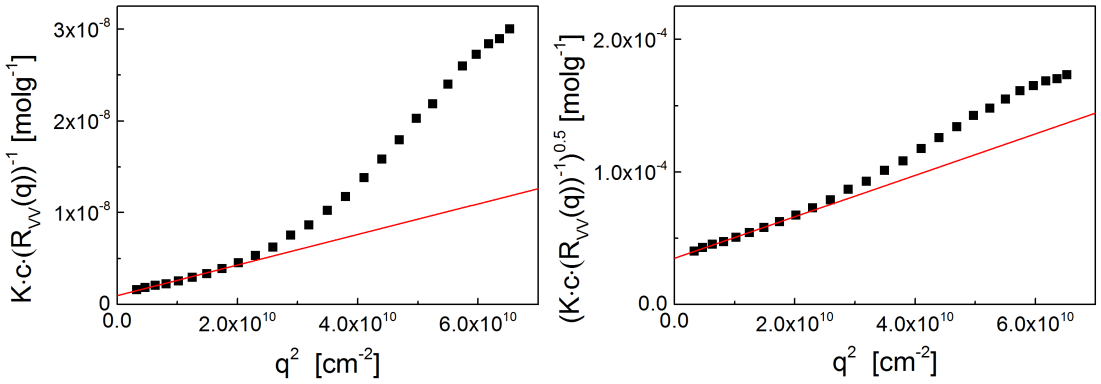

Figure 4.3: *Ornstein-Zernicke (a) and Debye representation (b) of the scattering data. The apparent molecular weight M_{app} can be obtained from the inverse of the intercept at $q = 0$.*

($dn/dc = 0.188$ mL g^{-1}). The apparent molecular weight obtained from the inverse of the intercept in the Ornstein-Zernicke representation is $M_{\mathrm{app}} = 1.05 \cdot 10^9$ g mol^{-1}, and hence the aggregation number N_{agg} is ≈ 160000. However, the inverse intensity vs. q^2 is not perfectly linear at low q values. Therefore, the square root of the inverse scattering intensity vs. q^2 was plotted (Debye representation, Figure 4.3b). Here, the curve is linear at low q's and the obtained M_{app} from the intercept is $M_{\mathrm{app}} = 8.3 \cdot 10^8$ g mol^{-1}($N_{\mathrm{agg}} \approx 125000$). These values were assumed for all further experiments.

DLS was used to determine the radius of hydration, R_{h}, of the vesicles. All recorded correlation functions show a single relaxation process only (Figure 4.2b), indicating that only one major diffusion species is present in the sample. A stretched exponential fit (KWW, see subsubsection 3.2.1.3 (Data Evaluation)) was used to analyze the DLS data. The distribution of relaxation times τ is described by a shape parameter $\beta_{\mathrm{KWW}} \approx 1$ for almost all q's. For very high q's, $\beta_{\mathrm{KWW}} \approx 0.95$. These values also confirm the existence of only one diffusing process. The inset of Figure 4.2b shows the diffusion coefficient D^{t} vs. q^2. One can observe slight q-dependence, which is due to the vesicle's polydispersity and size. The small decline of D^{t} at high q's can be attributed to the presence of small vesicles in the sample as well as within the major polymersomes (*pregnant vesicles*, see Figure 4.4). D^{t} ($q \to 0$) was determined from both the fit with equation Equation 4 from the Appendix ($D^{\mathrm{t}}(q \to 0) = 1.66 \cdot 10^{-8}$ cm^{2}s^{-1}) and from the intercept of the

linear variation of D^t vs. q^2 ($D^t(q \rightarrow 0) = 1.69 \cdot 10^{-8}$ cm^{2}s^{-1}). Using Einstein-Stokes equation (Equation 3.12), R_h was determined to be 129 nm and 127 nm, respectively. For simplification and according to the marginal difference between the two estimated values for D^t ($q \rightarrow 0$), all experimental D^t ($q \rightarrow 0$) were determined from the linear fit of D^t vs. q^2 only.

The hydrodynamic radii for all different samples are listed in Table 4.3. It can be seen that the formed vesicles are similar in size, which is due to extrusion through a membrane with pore size $\approx$ 200 nm. However, the values for ρ differ. ρ is only close to 1 for BC-20h-NH, BC-40h-NH and BC-40h-OH. For the other samples, ρ <1, and the errors of R_g and R_h increase. For those samples, estimation of R_g from the slope of the Guinier plot was difficult due to a kink in the slope, getting larger radii for low q's and smaller radii for high q values. Therefore, it is assumed that these samples are very polydisperse. However, it must be considered, that the values for R_g and R_h depend very much on the applied extrusion technique (see subsection 4.1.2 (Vesicle Formation by Extrusion)). Nevertheless, BC-40h-NH and BC-40h-OH provided qualitatively the best cryo-TEM pictures among all samples. Since in the previous work on PDMS-*b*-PMOXA by Karmena Jaskiewicz piperazyl-functionalized polymers have been used, BC-40h-NH was chosen as standard vesicles for any further experiments. In addition, their scattering intensity resembled the vesicles used in Karmena Jaskiewicz work the most.

4.1.3.2 Cryo-TEM

The huge advantage of PCS over cryo-TEM is, that PCS measurements are integrating over a large number of scattering centers. Therefore, PCS experiments allow certain statistical analysis of the investigated structures and few exceptions from the average structure are of (almost) no consequence to the signal. Furthermore, PCS experiments are carried out in solution, and scattering of the investigated vesicles is very strong due to their size and refractive index. Consequently, PCS experiments can be conducted at very low concentrations, while obtaining its sensitivity. In contrast, TEM studies allow the analysis of only a very small number of individual structures, being very prone to artifacts. In addition, conventional TEM is not performed in aqueous solutions but on

Table 4.3: *Characteristics (Radius of gyration R_g, hydrodynamic radius R_h, and structure parameter ρ) of different PDMS-b-PMOXA polymersomes obtained from SLS and DLS.*

Sample	R_g [nm]	R_h [nm]	ρ
BC-20h-NH	118.3 ± 0.5	126.1 ± 2.4	0.94 ± 0.2
BC-20h-OH	129.7 ± 2.7	195.7 ± 8.7	0.66 ± 0.4
BC-30h-NH	110.4 ± 1.3	136.3 ± 2.6	0.81 ± 0.2
BC-30h-OH	110.1 ± 2.1	151.3 ± 6.2	0.73 ± 0.2
BC-40h-NH	128.0 ± 1.4	126.9 ± 2.8	1.01 ± 0.3
BC-40h-OH	111.1 ± 0.5	109.2 ± 1.4	1.02 ± 0.2
BC-48h-NH	107.8 ± 2.5	152.1 ± 7.3	0.71 ± 0.4
BC-48h-OH	112.4 ± 2.6	149.0 ± 4.3	0.75 ± 0.3
BC-65h-NH	116.7 ± 1.7	133.9 ± 4.2	0.87 ± 0.4

dried samples and the resulting pictures would therefore alienate the true picture pf PDMS-*b*-PMOXA polymersomes due to drying effects. In all probability, vesicles would even be destroyed upon drying. Nevertheless, TEM imaging is necessary for obtaining graphical pictures of the vesicles and for determining the vesicle's membrane thickness d. To ensure realistic imaging of the polymersomes, cryogenic transmission electron microscopy (cryo-TEM) was applied.

Figure 4.4 shows cryo-TEM pictures of vesicles formed from different PDMS-*b*-PMOXA batches. Estimating the size of the vesicles from cryo-TEM pictures is pointless, since the vesicles may be compressed from the blotting procedure. However, one can estimate the vesicle's membrane thickness using cryo-TEM pictures with good contrast between the membrane and the surrounding ice. Here, the average membrane thickness of vesicles from BC-40h-NH was measured from 150 different vesicles. The results are shown in Figure 4.5 and result in an average thickness of 16 ± 2 nm. Most of the vesicles in Figure 4.4 are perfectly spherical and empty inside. However, also smaller vesicles and so-called pregnant vesicles (vesicles with small vesicles or micelles inside) can be found. As shown by PCS, the average R_h of the vesicles is ≈ 130 nm, and polydispersity is rather

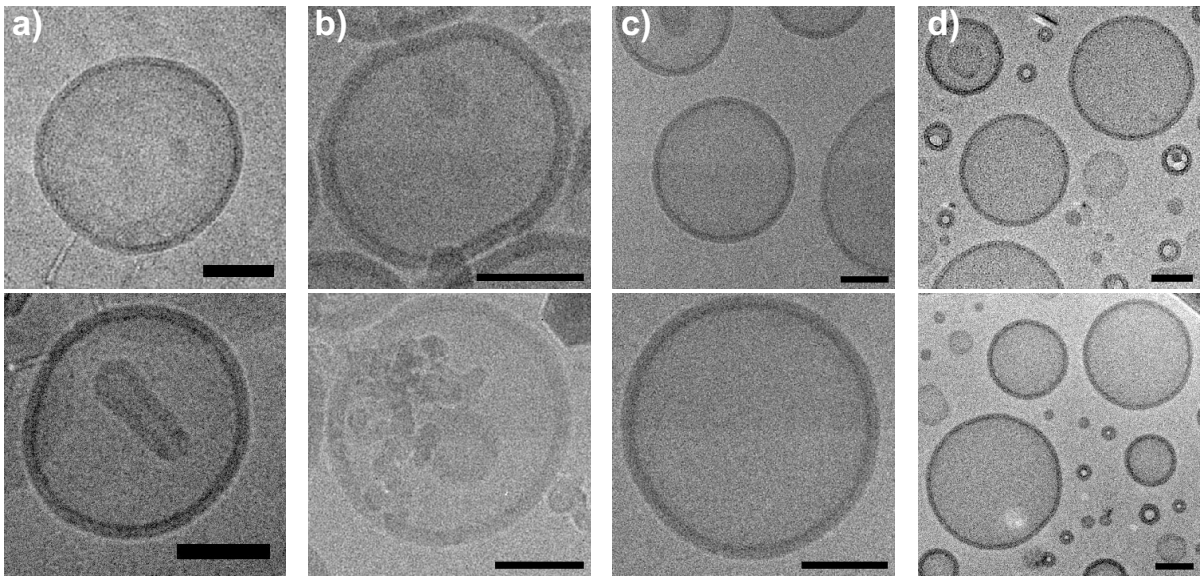

Figure 4.4: *Cryo-TEM pictures of different vesicles from Table 4.3. a) BC-20h-NH b) BC-40h-NH c) BC-48h-NH d) BC-65h-NH. The scale bar corresponds to 100 nm. Images were recorded by Max Bernhardt [Ber14]*

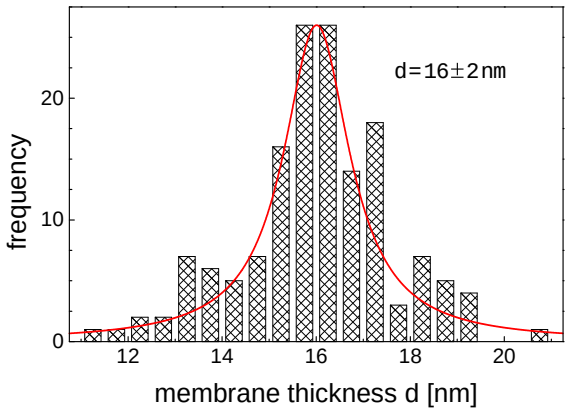

Figure 4.5: *Measured membrane thickness d of vesicles formed from BC-40h-NH. The values were obtained from cryo-TEM pictures of 150 different vesicles.*

low. Since cryo-TEM investigates only a small number structures, a quantitative analysis of the vesicle's size and polydispersity is not possible. However, it should be noted that also smaller vesicles and so-called *pregnant vesicles* are present in the vesicle solution.

4.2 Synthesis and Characterization of Au Nanospheres

In this section, the synthesis and characterization of spherical Au particles is described as well as their chemical surface modification by grafting. Synthesis and surface modification was performed by Sebastian Harms at the University of Mainz. The particles were carefully characterized by surface plasmon resonance enhanced dynamic polarized and depolarized light scattering at two wavelengths. UV/Vis, single-particle dark field spectroscopy and TEM revealed the virtually spherical shape of the bare gold particles with almost no aspect ratio. Nevertheless, it was found that the depolarized light scattering inherent to the spherical bare AuNP's is not zero due to the inevitable internal crystallinity [Pia91, Por10]. In addition, the arrangement of the grafting on spherical cores is asymmetric as proposed by two recent simulation papers [Lan10, Boz13]. The wavelength dependent depolarization ratio, the single UV/Vis extinction spectrum and two transport coefficients of the same Au spheres grafted with ligands of different chemistry and length are all consistently described only if their coating is asymmetric. Spatially anisotropic graft distribution on spherical nanoparticles impacts their assembly, the structure and properties of polymer nanocomposites.

The following section is adapted from the publication "Surface Asymmetry of Coated Spherical Nanoparticles" by Amelie H. R. Koch, Gaëtan Lévêque, Sebastian Harms, Karmena Jaskiewicz, Max Bernhardt, Andreas Henkel, Carsten Sönnichsen, Katharina Landfester and George Fytas, published in 2014 in Nano Letters, volume 14 on pages 4138 to 4144 [Koc14]. The publication is reprinted with permission. Copyright 2014 American Chemical Society.

4.2.1 Synthesis and Surface Modification of Spherical Au-NPs

Spherical AuNPs were synthesized by Sebastian Harms at the University of Mainz (AK Sönnichsen) by reduction of chloroauric acid ($H[AuCl_4]$) in aqueous solution - a method which was already introduced by Turkevitch in 1951 [Tur51]. Experimental details are given in subsection 3.1.3 (Nanoparticle Synthesis and Surface Modification). The size of the obtained AuNPs can be controlled by the molar ratio between the reducing

agent (trisodium citrate) to the gold derivative. Two batches with slightly different particle diameters d (d_1 = 41nm and d_2 = 44nm) were obtained and were characterized independently. Given by the experimental procedure, the surface of the bare AuNPs are stabilized by a physiosorbed layer of citrate molecules, which gives rise to a negative ζ-potential ($\approx$ -20 mV) of the particles. The extinction maxima of the Au particles were $\lambda_{\max}$ ($d_1 = 41$ nm) = 522 nm and $\lambda_{\max}$ ($d_2 = 44$ nm) = 524 nm, which are characteristic for their size and spherical shape, and were verified by theoretical calculations. Immediately after preparation of the bare (citrate) particles, the citrate layer was replaced by different ligands, which bound covalently to the Au surface via thiol-gold binding.

4.2.2 Surface Asymmetry of Coated Spherical Au-NPs

The synthesized nanoparticles were characterized in very dilute aqueous dispersions by dynamic polarized and depolarized light scattering, UV/Vis extinction and single-particle dark field spectroscopy. The system and methods were selected on the account of the sensitivity of the depolarized light scattering to deviation from spherical symmetry which is, moreover, localized surface plasmon resonance (LSPR) enhanced [Hag13]. In addition, the LSPR frequency of the Au core strongly depends on orientation and local environment of the particle [Kel03].

4.2.2.1 Characterization

The virtually spherical shape of two bare AuNPs was revealed by transmission electron microscopy (TEM) and single particle polarization anisotropy (PA) experiments [Sch08, Can08] and supported by the extinction spectrum in dilute aqueous solutions. TEM images for the AuNP with the thinnest (citrate) coating shows the size distribution with an average 44 ± 4 nm diameter (Figure 4.6a,b) and revealed the crystalline nature of each individual AuNP at high resolution TEM (Figure 4.6c). Polycrystallinty [Por10, Hua07, Tan07] turns out to be crucial for the behavior of electrons and twining defects can impact the optical properties as discussed below. The single peak in the extinction spectrum of Au-citrate NP (Figure 4.6d) conforms to the spherical symmetry of the Au core displaying only one LSPR mode. In contrast, elongated particles would exhibit two LSPR modes, a

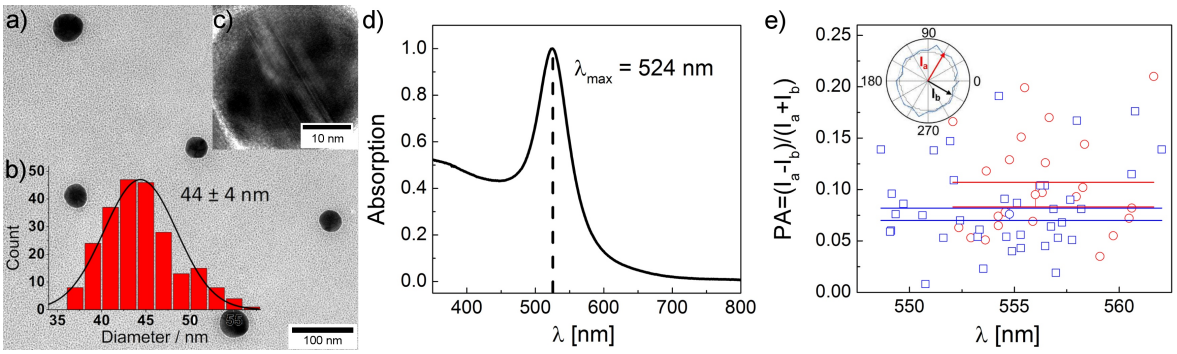

Figure 4.6: *(a) Transmission electron microscopy (TEM) of gold nanoparticles (AuNPs), (b) size-distribution, (c) high resolution TEM of a single AuNP and (d) the localized surface plasmon resonance peak in the extinction spectrum of dilute suspension of AuNP stabilized with citrate. (e) Polarization anisotropy measured by single-particle dark-field spectroscopy shows similar asphericities for Au-citrate (red circles) as well as Au-PEG$_{107}$ (blue squares).*

transverse one for the particle's short edge, and a longitudinal one for the long edge. For the AuNPs studied here, a quantitative measure of the asphericity was obtained by PA experiments using particles from the same batch but with different graftings (Au-citrate and Au-PEG$_{107}$, grafted with citrate ions and polyethyleneglycol (PEG) chain of about 107 monomer units, respectively). The results from the PA measurements can be seen in Figure 4.6e. The pattern of the polarization anisotropy of the scattering intensity from individual Au cores revealed a virtually spherical shape with very low aspect ratios of 1.029 and 1.023 for citrate- and PEG-coated particles respectively, which were calculated from the polarization anisotropy. The very low aspect ratios confirm almost absolute spherical shape of the particles. As expected, the geometry of the Au cores are identical regardless of their grafting.

The AuNPs were further characterized by PCS. Surprisingly, in addition to scattering in the polarized mode (VV), relatively strong scattering was also observed in the depolarized mode (VH). The absolute polarized $R_{\mathrm{VV}}(q)$ and depolarized $R_{\mathrm{VH}}(q)$ are shown as a function of the scattering wave vector q for a 0.02 nM Au-citrate solution in Figure 4.7c. $R_{\mathrm{VH}}(q)$ is virtually flat, while $R_{\mathrm{VV}}(q)$ exhibits a weak q-dependence due to the small particle size (Guinier plot in Figure 4.8a). Unexpectedly, the depolarization ratio

$\rho = R_{VH}/R_{VV} = 7\%$ is very high considering the spherical shape of the Au core. For perfect spheres, rotation of the particle would not change the dipol of the scatterer, and hence no VH-scattering would be observed. This is different for asymmetric and especially rod-shaped particles. In contrast to Au nanospheres, the asphericity of Au nanorods causes dynamic depolarized light scattering, which besides is significantly enhanced near the longitudinal SPR frequency [Hag13]. So far, this effect has not been observed for plasmonic nanospheres with a single LSPR mode. However, anisotropic dynamic light scattering was also anticipated for spherical NPs due to inherent crystallinity, as demonstrated by Piazza and Degiorgio, who observed depolarized light scattering for latex spheres (polytetrafluoroethylene copolymer) with partially crystalline internal structure [Pia91, Deg94].

The strong VH scattering of the AuNPs allowed to record the orientation relaxation functions $C_{VH}(q,t)$ which exhibit a single exponential decay with relaxation rate $\Gamma_{VH}(q) = 6D^r + q^2D^t$ (Figure 4.7c), where D^r and D^t denote the rotational and translational diffusion coefficients. For fast D^r ($> q^2 2D^t$), the estimation of D^t from the slope of $\Gamma_{VH}(q)$ is subject to large error. Hence it was obtained from the $C_{VV}(q,t)$ which in all known cases but plasmonics is a single decay function with a relaxation $\Gamma_{VV}(q) = q^2D^t$. For noble metal NPs, however, the anisotropic R_{VH} is LSPR-enhanced and hence its contribution in $C_{VV}(q,t) = a_{VH}exp(-\Gamma_{VH}t) + a_{iso}exp(-D^tq^2t)$ can be discernible as a second fast decay (arrow in Figure 4.7a) with amplitude a_{VH}; for Au nanorods with comparable amplitudes, the two-step decay of $C_{VV}(q,t)$ becomes very pronounced [Hag13]. The slow purely isotropic component with amplitude a_{iso} decays via translational diffusion allowing a precise determination of D^t from the slope of the linear dependence, $\Gamma_{VV}(q) = q^2D^t$(Figure 4.7b). The consistent representation of $C_{VH}(q,t)$ and $C_{VV}(q,t)$ is also indicated by the same slope of $\Gamma_{VH}(q)$ and $\Gamma_{VV}(q)$ in Figure 4.7b. The transport coefficient, D^r is directly obtained from the intercept of $\Gamma_{VH}(q)$.

The polarized and depolarized DLS experiments yielded the transport coefficients, D^r and D^t. SLS experiments yielded the depolarization ratio, ρ, measured for seven different grafts of the same Au core at 532 nm (green laser), near the peak position (λ_{max}) of the LSPR mode, and at 632 nm (red laser), representing off resonance condi-

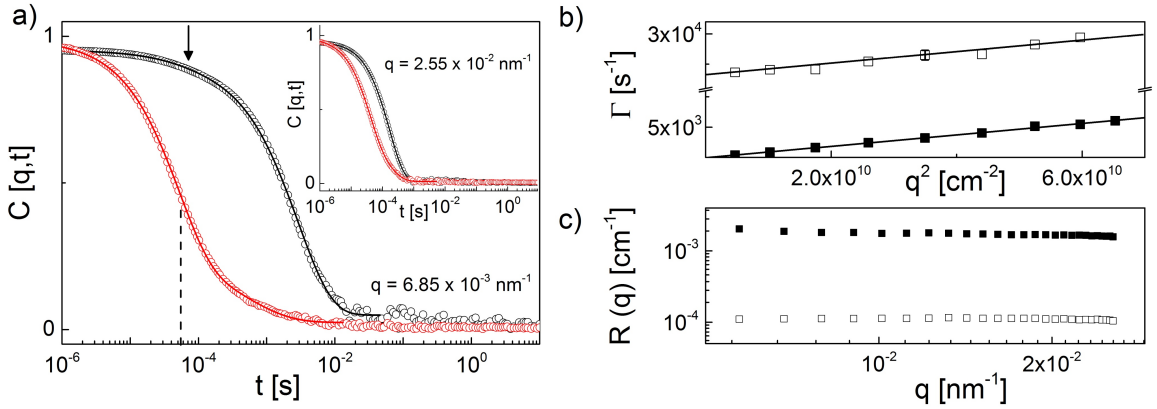

Figure 4.7: *a) Relaxation functions [$C_{VV}(q,t)$, $C_{VH}(q,t)$] for a dilute ($c = 0.01\ gL^{-1}$; $c_M = 0.02$ nM) aqueous suspension of Au nanospheres (diameter $d = 44$nm) stabilized with citrate at the scattering wave vector $q = 6.85 \times 10^{-3}\ nm^{-1}$ (corresponding to a diffusion length ~ 920nm), recorded for VV (black symbols) and VH (red circles) polarizations. The solid lines indicate the theoretical representation (see text) of the experimental functions and the arrow denotes the fast VH contribution to $C_{VV}(q,t)$. b) The relaxation rate Γ_s (solid squares) for the slow (VV) and Γ_f (open squares) for the fast (VH) component in $C_{VV}(q,t)$ and $C_{VH}(q,t)$, respectively. c) Time-average absolute Rayleigh ratio for polarized $R_{VV}(q)$ (solid squares) and depolarized $R_{VH}(q)$ (open squares) light scattering for the same Au nanospheres solution vs. q. The PCS experiment was performed with coherent laser light at $\lambda = 632$ nm above λ_{max} (~ 524 nm) of the extinction spectrum (Figure 4.6d).*

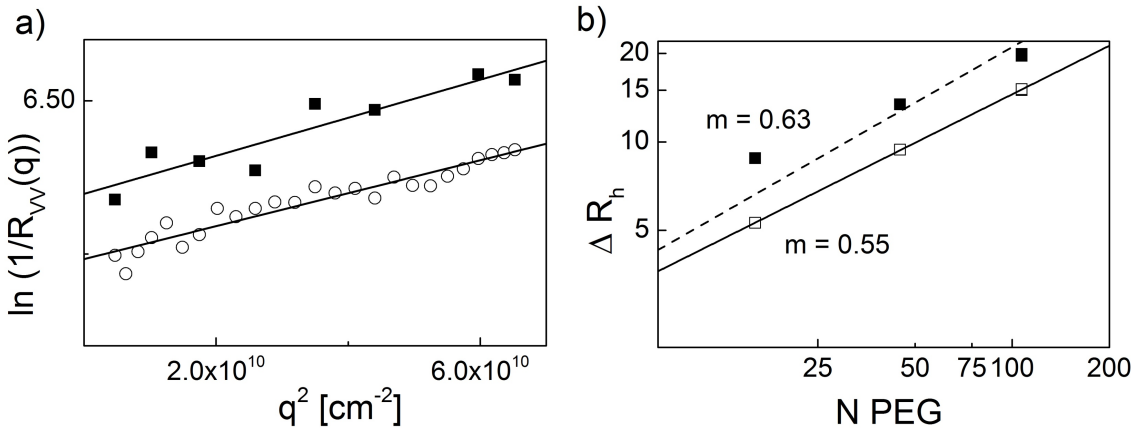

Figure 4.8: *a) Guinier plot, ln[1/$R_{VV}(q)$] vs q^2, for either the total polarized $R_{VV}(q)$ (open circles) or the pure isotropic $R_{ISO}(q)$ (solid squares) contribution obtained from the relaxation function $C_{VV}(q,t)$. b) Grafted layer thickness plot vs. degree of polymerization of the PEG grafts for AuNP with d = 44 nm in a log-log presentation yielding a slope ν = 0.55 (spherical geometry) and ν = 0.63 (ellipsoidal geometry).*

tions. From D^{t} and D^{r}, the hydrodynamic radius $R_{\mathrm{h}} = kT/(6\pi\eta_s D^{\mathrm{t}})$ and the rotational radius $R_{\mathrm{r}} = [kT/(8\pi\eta_s D^{\mathrm{r}})]^{1/3}$ for spheres under stick boundary conditions were calculated, where k is the Boltzmann's constant and η_{s} the solvent viscosity. In the opposite case of slip boundary conditions, R_{h} and in particular R_{r} would assume unacceptable much higher values in order to conform to the two experimental transport coefficients [Sch04, Koe03]. The obtained radii (R_{h}, R_{r}) are summarized in Table 4.4, as well as the depolarization ratio at two irradiation laser wavelengths and the position of localized surface plasmon resonance peak for very dilute suspensions of the same AuNP core (with diameter d = 44 nm) bearing seven different coatings. The scaling of the layer thickness for the PEG-grafted Au nanospheres, $\Delta R_{\mathrm{h}} = (2R_{\mathrm{h}}\text{-}d) \sim \mathrm{N}^{0.6}$ (Figure 4.8b) with the PEG degree of polymerization, N, implies swollen chain configurations. The absolute Rayleigh scattering intensities, R_{VV} and R_{VH}, are stronger near resonance (λ = 532nm), but exhibit a different drop at λ = 632 nm, as seen in Figure 4.9a. Consequently, the polarization ratio depends on λ, but surprisingly ρ assumes a larger value at λ = 632 nm, i.e. at off-resonance (Figure 4.9b, Table 4.5); the highest value is observed for the citrate and the lowest for the DNA coatings. The experimental quantities, intensities, depolar-

Table 4.4: *Characteristic dimensions of grafted Au nanospheres with diameter of 44 nm, depolarization ratio at two optical wavelengths and the wavelength of the single surface plasmon resonance.*

	R_h [nm]	R_r [nm]	$\rho = R_{VH} / R_{VV}$		λ_{max} [nm]
			632nm	532nm	
Au-citrate	23.7 ± 0.5[a)]	34.8 ± 0.7	0.07	0.01	524
Au-PEG_{16}	27.3 ± 0.4[b)]	36.8 ± 0.7	0.03	0.01	524
Au-PEG_{45}	31.4 ± 0.5[b)]	40.0 ± 2.0	0.04	0.02	525
Au-PEG_{107}	37.0 ± 1.4[b)]	40.0 ± 0.6	0.02	0.01	525
Au-$PEG_{107\text{-}COOH}$	37.1 ± 0.4[b)]	44.0 ± 1.3	0.03	0.01	525
Au-DNA_{T10}	32.0 ± 1.9	42.0 ± 2.1	0.01	0.01	526
Au-DNA_{T40}	36.5 ± 0.5	42.0 ± 1.4	0.01	0.01	526

[a)] For Au-citrate, $2R_h \approx d$ from TEM. [b)] For Au-PEG_N, the layer thickness $\Delta R_h = (2R_h - d) \sim N^{0.6}$ (Figure 4.8b).

ization ratio and the ratio of the two transport coefficients, assume the same values at 20 °C and and 50 °C.

Unexpectedly, $R_r > R_h$ for all examined AuNPs, and the value of ρ varies from 0.01 to 0.07 depending on the wavelength λ of the illuminated light and the grafted layer on the same Au core. For all grafts, ρ is stronger when λ is off resonance (at 632 nm) as shown in Figure 4.9b due to the different λ-dependence of the R_{VV} and R_{VH} intensities Figure 4.9a. This behavior was also found for a different Au core (d = 41 nm) also with chemically different grafts (Figure 4.10 and Table 4.5).

4.2.2.2 Theoretical Models

The observed finite values and the λ-dependence of the depolarization ratio can be described by analytical and numerical models (see Appendix section B (Theoretical Details)). Since for AuNPs of spherical shape $\rho = 0$, the predicted behavior for a

Table 4.5: *Characteristic dimensions of grafted Au nanospheres with diameter of 41 nm, depolarization ratio at two optical wavelengths and the plasmon resonance wavelength.*

	R_h [nm]	R_r [nm]	$\rho = R_{VH} / R_{VV}$		λ_{max} [nm]
			632nm	532nm	
Au-citrate	23.5 ± 0.7	36.3 ± 0.5	0.12	0.02	522
Au-PEG_{16}	23.0 ± 0.7	31.0 ± 1.5	0.01	0.01	523
Au-PEG_{45}	24.9 ± 0.7	29.5 ± 0.7	0.01	0.01	524
Au-PEG_{107}	30.4 ± 0.6	37.6 ± 0.7	0.01	0.01	524
Au-$PEG_{107\text{-}COOH}$	31.9 ± 0.3	34.7 ± 0.7	0.01	0.01	523
Au-CTAB	22.8 ± 0.7	32.7 ± 0.3	0.04	0.01	525
Au-MUA	28.4 ± 0.5	36.6 ± 0.4	0.07	0.02	525

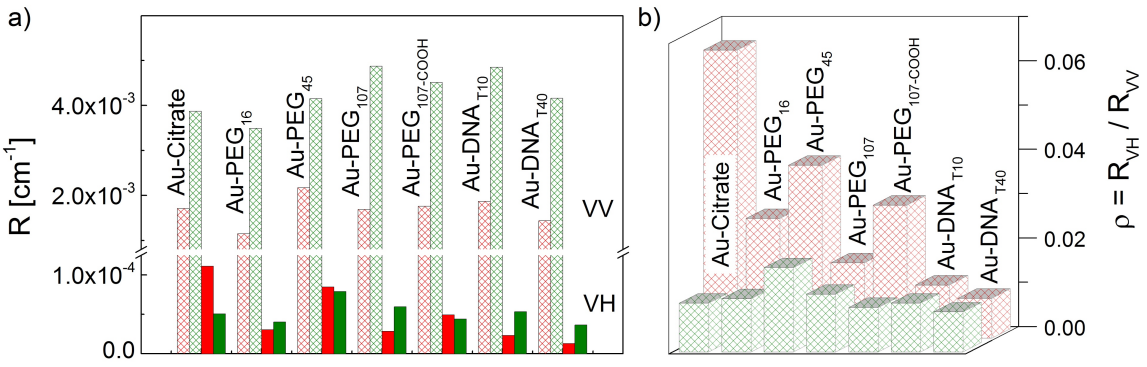

Figure 4.9: *a) Absolute Rayleigh ratio for polarized (R_{VV}, hatched areas) and depolarized (R_{VH}, solid areas) light scattering and b) depolarization ratio ρ at 532 nm (green) and 632 nm (red) for a dilute suspension of Au nanospheres with 44 nm diameter core and different grafts as indicated in the plots.*

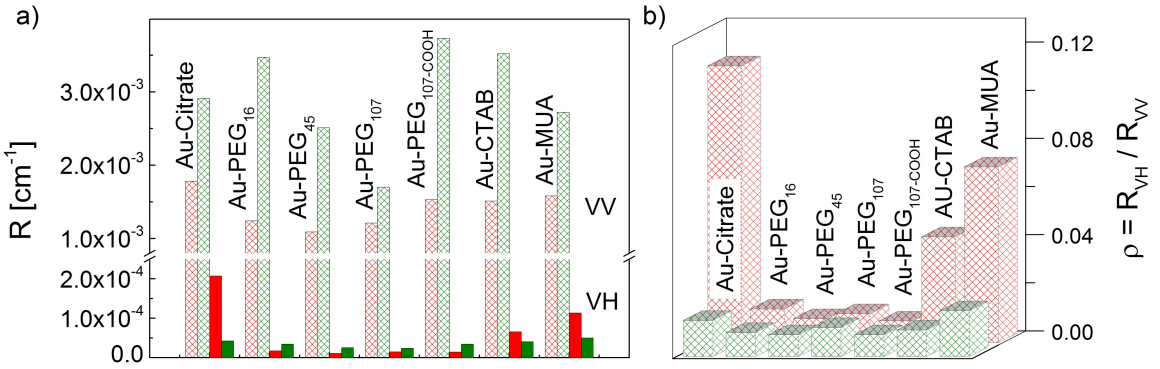

Figure 4.10: *a) Absolute Rayleigh ratio for polarized (R_{VV}, hatched areas) and depolarized (R_{VH}, solid areas) light scattering and b) depolarization ratio ρ at 532* nm*(green) and 632* nm*(red) for a dilute suspension of Au nanospheres with 41* nm*diameter core and different grafts as indicated in the plots.*

spheroidal "monocrystalline" Au core using the Green's tensor method (subsection B.2) was described. The length ratio, b/a, of the particle main axis (b) to the perpendicular degenerated axis (a) was allowed to slightly vary around one according to the single-particle dark-field microscopy results (Figure 4.6e) but considering also a size distribution with a width Δb. The experimental condition of a single peak extinction spectrum (Figure 4.6d) set the upper bound of the ratio $\Delta b/b \sim 10\%$ as suggested by the distribution obtained from the TEM images (Figure 4.6b). Spheroids with this size distribution, however, could neither reach the experimental depolarization ratio values, nor predict the experimentally observed higher value of the depolarization ratio at off-resonance. This opposite trend in the theoretical calculations is demonstrated in Figure 4.11a. While the maximum value of ρ expectedly increases with $\Delta b/b$, it occured near resonance ($\sim$ 550 nm) and its value even for an aspect ratio $\sim$ 1.1 remaines well below the experimental value.

To boost the value of ρ and predict an off-resonance enhancement, "polycrystallinity", which is the origin for the present non-zero depolarized light scattering from spherical Au cores, was introduced in an analytical model. Crystallinity characterization is a challenging issue and can benefit from the study of twining defects on the properties of plasmonic NPs. The splitting of the quadrupolar vibration mode in the low frequency Raman spectrum [Por10] due to LSPR-acoustic coupling is related to the crystallinity

of an ensemble of AuNPs. Here, nanocrystallinity is related to the anisotropic optical properties due to anisotropic electron free paths. More precisely, the effect of a cut plane between two monocrystals was modeled as an increased absorption rate of the free electrons in gold colliding with the cut plane, resulting in a shortened mean free path for the electrons moving perpendicular to the cut compared to the electrons moving parallel to it. Such a model is often used to describe the increased absorption in metal nanoparticles of size shorter than the mean free path of the free electrons in the bulk metal [Ber05].

Hence, a basic phenomenological model for the Au-polycrystallinity has been implemented in the theoretical calculations (Appendix subsection B.2). The polycrystalline particle was described as a spherical or spheroidal particle cut into several parallel slices of equal thickness l, along the direction of one of the principal axis, as shown in Figure B.1 in the Appendix. Each cut plane between two slices behaves as a barrier whose effect is to increase the collision rate of electrons moving perpendicularly to it by a factor inversely proportional to the slice thickness; for n cuts (n being called in the following the degree of polycrystallinity), l takes the values $2R/(n+1)$. This introduces an anisotropic electron mean free path. Electrons moving normal to the cut planes have a shorter mean free path on the order of l compared to $2R$, when the electrons are moving along one of the two other directions parallel to the cut planes. Consequently, the light absorption for polarization perpendicular to the cut plane will be larger than for light polarized along the two other directions. In the following, the former is called the *inherent* Au *anisotropy*. Hence the anisotropic absorption renders the depolarization ratio of an otherwise spherical shape higher.

Using an analytical expression of the depolarization ratio (Appendix Figure B.2), it was shown that the value of ρ at maximum ($\lambda \sim 550$ nm) of Au nanospheres increased rapidly for $l/2R < 1$ and $\rho \sim 1\%$ could be formally captured for $l/2R \sim 0.05$ as seen in Figure 4.11b. In this model, a symmetric coating of the Au nanosphere, i.e., a spherical core-shell particle, failed to predict the experimental ρ (532nm) $<$ ρ (632nm) trend, irrespectively of the values of the adjustable parameters, which in this case were the shell refractive index and the degree n of polycrystallinity. Instead, ρ (532nm) was an order

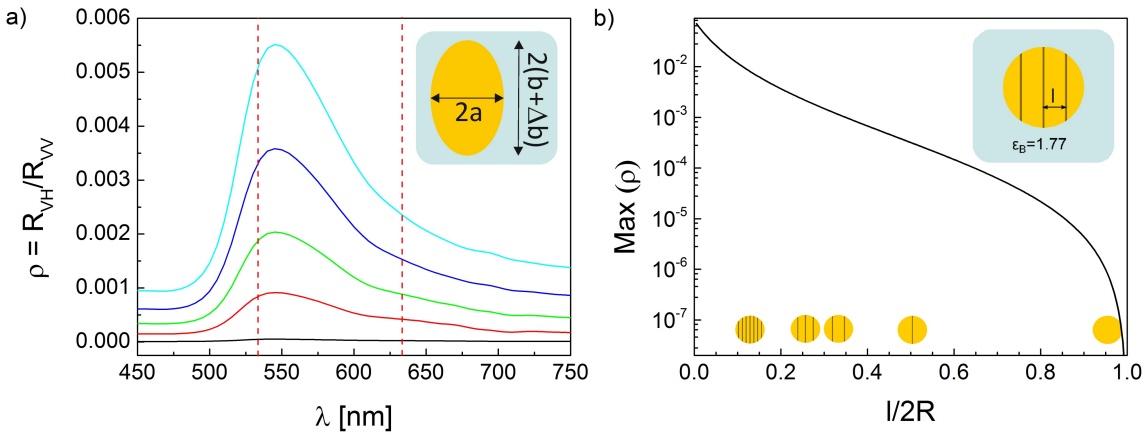

Figure 4.11: *a) Calculated depolarization ratio ρ for spheroidal Au NP in the presence of size distribution and different shapes in the range $0 \leq \Delta b/b \leq 10\%$ ($\Delta b/b = 2\%$ (black), $\Delta b/b = 4\%$ (red), $\Delta b/b = 6\%$ (green), $\Delta b/b = 8\%$ (blue), $\Delta b/b = 10\%$ (cyan)). The two vertical lines denote the wavelengths of the lasers employed in the experiment. The maximum depolarization ratio (at about 550*nm*) increases with the asphericity $\Delta b/b$. b) Effect of polycrystallinity modeled by anisotropic absorption, i.e. anisotropic electron mean free path l.*

of magnitude larger than ρ(632nm) for symmetric coatings of spherical Au cores (see Figure B.2b in the Appendix).

So far, it was verified with this analytical model that an even coating around a spheroidal polycrystalline gold core systematically lead to ρ (532 nm) $\geq$ ρ (632 nm), the equality occurring for slightly prolate AuNPs with a polycrystallinity degree $n = 2$ (not shown). Similarly, combining polycrystallinity with slightly prolate or oblate AuNPs without any shell failed to reproduce the lower depolarization ratio at the plasmon resonance. Assuming, however, an asymmetric arrangement of grafts in the theoretical calculations, the behavior could be reversed. The graft is characterized by its thickness b' along the particle revolution axis, and a' along the two perpendicular degenerated axes. The extinction spectrum and the depolarization ratio for two graft arrangements in Figure 4.12 show that the depolarization ratio can be lower at resonance when the shell anisotropy is directed normal to the cut plane inside the AuNP, i.e. parallel to the inherent Au anisotropy direction (dashed lines in Figure 4.12); calculations for different

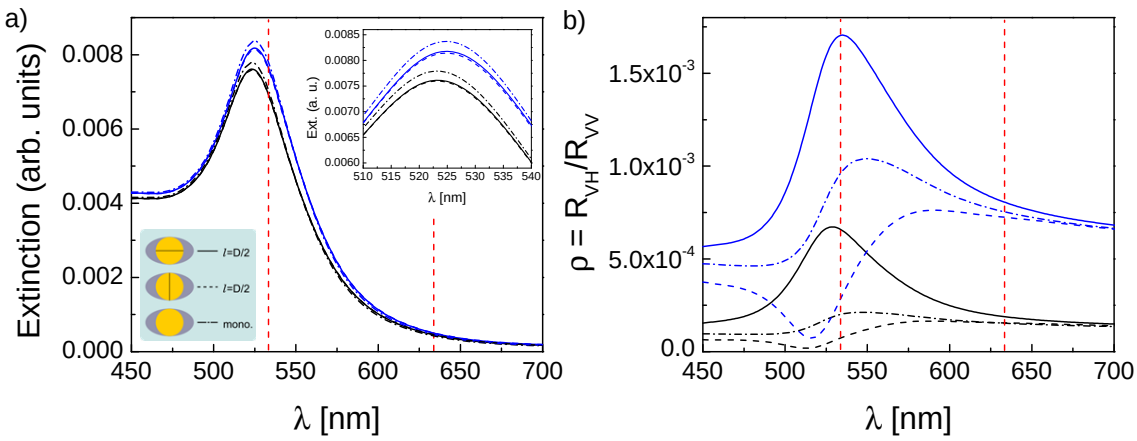

Figure 4.12: *a) Computed extinction spectra for polycrystalline Au nanosphere (d = 44 nm) coated with a nonspherical shell (a' = 0 nm, b' = 10 nm) and two different refractive indices (n_{graft} = 1.41, black; n_{graft} = 1.5, blue). The inherent Au anisotropy direction, perpendicular to the cut plane (the line in the gold core) inside the AuNP, is either perpendicular (solid lines) or parallel (dashed lines) to the graft anisotropy axis while the dot-dashed line is for monocrystalline AuNPs. b) Depolarization ratio for the three polycrystallinity configurations and the two graft refractive indices in a) as a function of the light wavelength; note the inversion of ρ (532 nm) / ρ (632 nm) between perpendicular (solid lines) and parallel (dashed lines) anisotropy directions. The two vertical dashed lines denote the wavelength of the two lasers employed in the experiment.*

b' values are presented in Figure B.2 in the Appendix. The extinction spectrum retains its single peak shape in agreement with the experiment apart from subtle frequency shift (inset to Figure 4.12a). For a "monocrystalline" Au core, ρ, caused by the imposed asymmetric grafting, is increased while it assumes the highest value at resonance. Finally, the strongest depolarization ratio was obtained when the grafting and inherent anisotropy directions are perpendicular to each other, and again reached the largest value at resonance. Quantitatively, the displayed behavior in Figure 4.12 depends on the assumed refractive index n_{graft} of the grafted layer and the effect is more pronounced for high n_{graft}.

A quantitative representation of the experimental ρ and $\rho^* = \rho\,(532\ \mathrm{nm}) \,/\, \rho\,(632\ \mathrm{nm}) \leq 1$ depended on the geometrical parameters (a', b'), polycrystallinity (n), dielectric constants of the Au core and hydrated grafts. Using the analytical model described in Ap-

Table 4.6: *Dimensions of the soft shell around the gold core for capturing the experimental data for $D_{\perp}^{r}$ and D^{t}.*

	p	a [nm]	b [nm]	κ
Au-citrate	1.3	22.0	28.6	2.95
Au-PEG_{16}	1.2	25.7	30.8	2.35
Au-PEG_{45}	1.2	29.5	35.4	1.85
Au-PEG_{107}	1.2	34.7	41.6	1.33
Au-$PEG_{107\text{-}COOH}$	1.2	34.9	41.9	1.55
Au-DNA_{T10}	1.1	31.0	34.1	1.95
Au-DNA_{T40}	1.1	35.0	38.5	1.55

pendix (Figure B.2), the core shape was deliberately fixed to a sphere (a=b) as asphericity was experimentally shown to be very small (Figure 4.6e), the polycrystallinity parameter n to 2, the sum a'+b' to the value deduced experimentally (see Table 4.6) for every type of grafting. The asphericity parameter b'/(a'+b') was then varied from zero to one, the case b'/(a'+b') = 0.5 corresponding to an even coating of the gold core. Figure 4.13 shows the theoretical prediction of the evolution of ρ^* with b'/(a'+b') for the six grafts on the Au core (d = 44nm). The experimental points have been obtained by matching the experimental value of ρ^* with the theoretical curve (solid circles). In any case, the obtained theoretical values for b'/(a'+b') were very close to the experimental ones. It is worth noticing that for the citrate shell, the experimental value of ρ^* is about 30% lower than the theoretical prediction, however, the minimum was obtained for b'/(a'+b')$\approx$0.93 (or a' $\approx$ 0) which is consistent with the experiment (Table 4.6). The AuNPs stabilized with citrate which is, unlike the PEG and DNA grafts, not covalently bonded, exhibit the strongest asphericity. Table 4.7 lists the parameters used in the calculations (shell refractive index n_{graft} and a'+b' deduced from the experiment (Table 4.6) and the results of the experimental (bold) and theoretical comparison.

All these values also represent well the two transport coefficients as described below. For all six grafts, $\rho^* \leq 1$ for $0.6 < b'/(a'+b') < 1$ which corresponds to an asymmetric

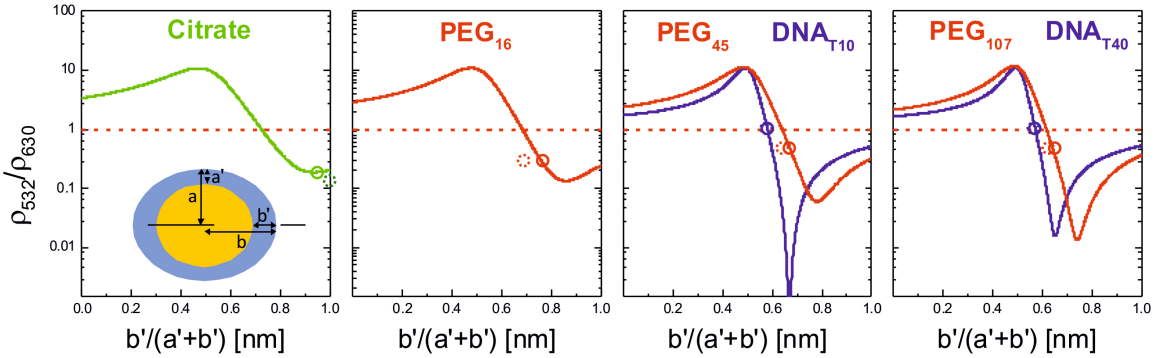

Figure 4.13: *Comparison between the experimental asphericity parameter b'/(a'+b') (dashed circles) with the corresponding computed (solid circles) ρ^* for the same AuNPs with six different coatings using core of diameter d = 44nm and the ρ^*=ρ(532 nm)/ρ(632 nm) values from Table 4.7.*

coating configuration. Since the grafting density can vary among the six systems, an account for the observed differences in the anisotropic coatings is not straightforward. For example, the lowest ρ^*, corresponding to the largest asphericity, was observed for citrate grafts on two different Au cores (Figure 4.13 and Table 4.5). The exact coverage of the grafts on the particles could not be obtained due to the minute quantity of the samples. It should also be noted that migration of the thiols on Au surfaces [Ima01] is not considered in the calculations, as the extent of this effect is still in dispute [Ion08].

Based on recent computer simulations [Lan10, Boz13, Sal14], the asymmetric graft arrangements around spherical NPs depend mainly on grafting density, core to shell sizes, and strength of interactions with the solvent. Qualitatively, low grafting density and long grafts promote NP anisotropy at constant core size. The simulations mostly take into account the graft length, but the density is difficult to include in the model. However, as the largest shell anisotropy has been obtained for citrate, which is not covalently bonded to the Au core, it was supposed that the distribution of citrate around the shell is very sparse. On the other hand, the correlation between inherent and grafting anisotropy directions (Figure 4.12) suggested from the theoretical calculations (Appendix Equation B.2) emphasizes the role of NP's crystallinity. It should be noted that a uniform coating was assumed in the simulation papers [Lan10, Boz13, Sal14].

Table 4.7: *Refractive indexes n_{graft} of the different coatings, experimental (from Table 4.6 in bold) and theoretical values of a', b', b'/(a'+b') and ρ^*.*

	$\mathbf{n_{graft}}$	**a' [nm]**		**b' [nm]**		**b'/(a'+b')**		$\boldsymbol{\rho^*}$	
Au-citrate	1.50	**0.0**	0.5	**6.6**	6.1	**1.00**	0.93	**0.14**	0.19
Au-PEG_{16}	1.46	**3.7**	3.1	**8.8**	9.4	**0.70**	0.75	**0.33**	0.33
Au-PEG_{45}	1.46	**7.5**	6.9	**13.4**	14.0	**0.64**	0.67	**0.50**	0.50
Au-PEG_{107}	1.46	**12.7**	11.6	**19.6**	20.7	**0.61**	0.64	**0.50**	0.50
Au-$PEG_{107\text{-}COOH}$	1.46	**12.9**	11.5	**19.9**	21.3	**0.61**	0.61	**0.33**	0.33
Au-DNA_{T10}	1.60	**9.0**	9.1	**12.1**	12.0	**0.57**	0.57	**1.00**	1.00
Au-DNA_{T40}	1.60	**13.0**	12.7	**16.5**	16.8	**0.56**	0.56	**1.00**	1.00

4.2.2.3 Transport Coefficients

Furthermore, the two transport coefficients D^{t} and D^{r} obtained from PCS were addressed utilizing the structural information obtained from the representation of ρ^* data. It is recalled (Table 4.4) that $R_{\mathrm{h}} < R_{\mathrm{r}}$ is not compatible with spherical symmetry of the AuNPs. Instead, implementation of anisotropic graft shape was also found to account for the difference between the two radii. For an adequate description of D^{r} by Perrin's equations (Appendix subsection B.3), the hydrodynamic volume, $V_{\mathrm{h}} = \kappa \cdot V_{\mathrm{o}}$, should exceed ($\kappa \geq 1$) the geometrical volume $V_{\mathrm{o}} = (4/3)\pi p a^3$ with the p=b/a being the aspect ratio. Since V_{h} is not accessible experimentally, the dimensionless κ was treated as an adjustable parameter together with the length b for the long spheroidal axis. For the short axis, the length a was well captured by the experimental hydrodynamic radius, R_{h}. More specifically, using $\mathrm{a} = 0.95 \cdot R_{\mathrm{h}}$, the two adjustable parameters b and κ were then obtained from the representation of D^{t} and D^{r} for all six systems. Figure 4.14 illustrates exemplarily the followed procedure in the case of Au-PEG_{16} for which $p \approx 1.2$ and $\kappa = 2.35$. Table 4.6 summarizes the values for the other systems as well. The value of κ is found to be large for thin shells and approaches asymptotically unity for long grafts (Figure 4.15), i.e. $V_{\mathrm{h}} \approx V_{\mathrm{o}}$.

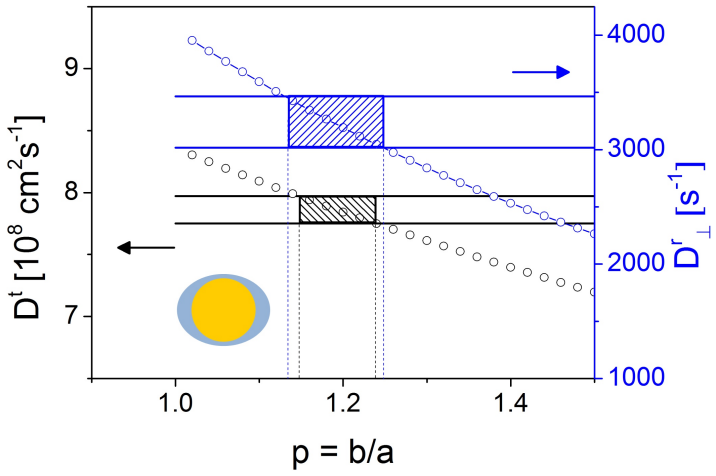

Figure 4.14: *Computed D^t (black) and $D^r_\perp$ (blue) for Au-PEG$_{16}$ using Perrin's eqs for spheroidal shape at different values of the aspect ratio p. The shaded black and blue rectangles represent the experimental range of D^t and $D^r_\perp$ respectively.*

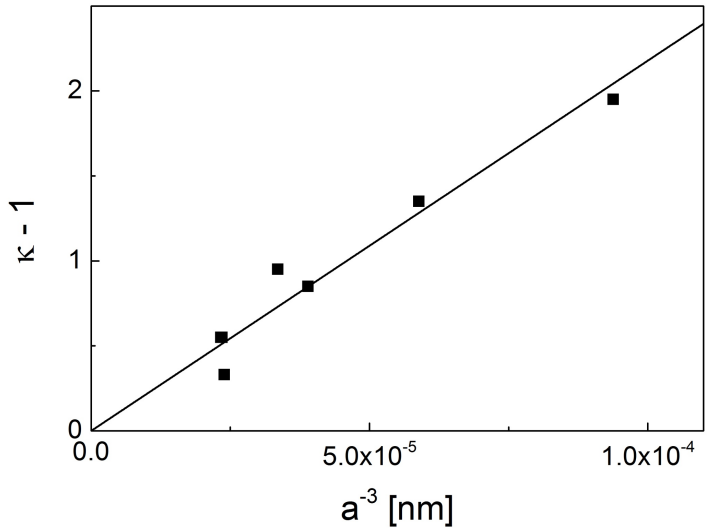

Figure 4.15: *The proportionality factor κ(black)=V_h/V_0 (V_h and V_0 denote the hydrodynamic and the geometrical volume) vs. $1/a^3$ for different grafts; κ approaches 1 at large a, and therefore $V_h = V_0$.*

Interestingly, while the bare Au cores assume almost a spherical shape (Figure 4.6e), the assigned asphericity occurs upon their soft grafting. This is the first experimental report on shape anisotropy of uniformly coated spherical particles, which according to recent simulations can be fluctuation induced [Boz13] or solvent-coating interactions [Lan10] mediated. Based on the theoretical representation of the present experimental results, the shell asphericity is parallel to the inherent, due to polycrystallinity, core anisotropy. According to theory and simulations of thiolate-protected gold surfaces [Häk12], it is conceivable that different Au outer facets with different binding energies can drive the organization of self-assembled monolayers, i.e. the reactivity of (111) facets is lower than of (110) surfaces [For06]. Noticeably, the present equilibrium configurations are robust to temperature variations between 20 °C and 50 °C. Since this effect was not considered in the simulations of the shape of coated NPs [Lan10, Boz13, Sal14], the present experimental work opens a new pathway for engineering the shape of metallic NPs driven by their nanocrystallinity. Access to the Au core nanocrystallinity defects is important since many physical properties such as reactivity and mechanical strength are depend on whether the metal NPs are 100% single crystalline or 100%twinned [Tan07]. On the other hand, control of the overall shape of the same spherical NPs by grafting impact their morphology in polymer nanocomposites [Akc09].

4.3 Uptake of Gold Nanospheres into Vesicles

In this section, the interaction of AuNPs with PDMS-*b*-PMOXA polymersomes is described. The AuNPs characterized in the previous section have been used for this study, as well as the polymersomes from section 4.1. Three possible scenarios were considered upon mixing of polymersomes and AuNPs: (i) no interactions between particles and vesicles, (ii) attachment of the particles to the outer side of the vesicle (decoration), and (iii) uptake of particles into the vesicles and either detachment or attachment of the endosome at the inner side of the membrane (see Figure 4.16). Upon mixing of polymersomes and AuNPs, the sample was allowed to stand for $\approx$ 15 min and were then carefully characterized by polarized and depolarized light scattering, UV/Vis spectroscopy and cryo-TEM. It was found that all three scenarios are possible, solely depending on the particle's surface functionalization. It is shown that polarized and depolarized light scattering are excellent tools for analyzing mixtures of vesicles and gold nanoparticles.

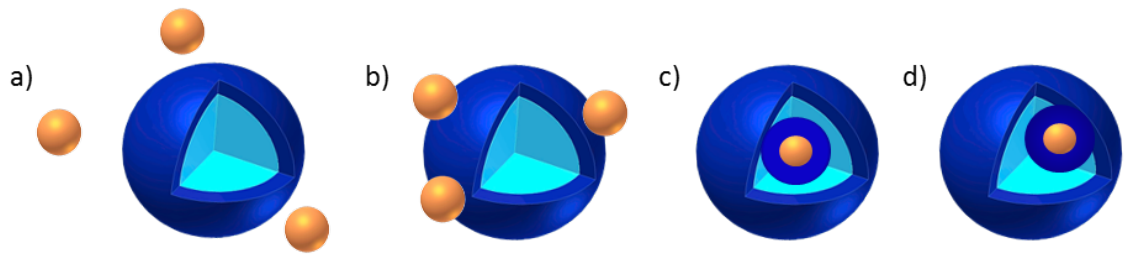

Figure 4.16: *Schematic representations of possible scenarios upon interactions of NPs with vesicles. a) no interaction between vesicles and NPs; b) decoration of vesicles with NPs; c) uptake and detachment of the endosome from the inner side of the membrane; d) uptake but endosome stays attached to the inner side of the membrane.*

4.3.1 Distinguishing Different Interaction Scenarios by PCS

The interaction of different AuNPs with polymersomes was studied by polarized and depolarized photon correlation spectroscopy (PCS). All gold particles used in this study exhibited the same Au core (with diameter d = 44 nm) but bearing three different coatings: Cetyl trimethylammonium bromide (CTAB), poly(ethylene glycol) (PEG) of about

Table 4.8: *Characteristic dimensions of vesicles and Au nanospheres dispersed in Milli-Q water, ζ-potential and surface plasmon resonance wavelengths.*

	c [nM]	R_h [nm]	R_r [nm]	ζ-Potential [mV]	λ_{max} [nm]
Vesicles	0.045	135 ± 3	-	+27.5 ± 1.1	-
Au-CTAB	0.2	22.8 ± 0.7	32.7 ± 0.3	+53.9 ± 8.1	524
Au-PEG_{107}	0.2	37.0 ± 1.4	40.0 ± 0.6	-2.1 ± 3.9	526
Au-Citrate	0.2	23.7 ± 0.5	34.8 ± 0.7	-29.2 ± 4.7	524

107 ethylene glycol units, and citrate (see previous section for particle characterization). CTAB is a cationic surfactant which causes a positive charge on the particle's surface due to its quaternary ammonium ion. PEG is grafted via stable thiol-gold bonds and exhibits a neutral charge on the particle's surface, whereas citrate-anions cause the surface to be negatively charged. ζ-potential was measured for all three particles as well as for the vesicles and the values are given in Table 4.8. As described before, the particles exhibit strong polarized and even depolarized light scattering due to the inherent crystallinity of the gold core and the anisotropic distribution of the grafting molecules, and hence give information on their translational and rotational diffusion coefficient, D^{t} and D^{r}, respectively. The dimensions of the particles, namely the computed hydrodynamic radius $R_{\mathrm{h}} = k_{\mathrm{B}}\mathrm{T}/(6\pi\eta_{\mathrm{s}}D^{t})$ and the rotational radius ($R_{\mathrm{r}} = [k_{\mathrm{B}}\mathrm{T}/(8\pi\eta_{\mathrm{s}}D^{r})]^{1/3}$ for a sphere under stick boundary conditions, where k_{B} is the Boltzmann's constant and η_{s} the solvent viscosity, are listed in Table 4.8. The hydrodynamic radii are in accordance with the size of the gold core plus the thickness of the graft. The higher values for R_{r} are due to asymmetric graft arrangements [Koc14]. The AuNPs all exhibited a single peak in the extinction spectrum, which conforms to the spherical symmetry of the Au core displaying only one LSPR mode. The measured extinction maxima λ_{max} and are consistent with the diameter of the gold core. The slightly red-shifted λ_{max} for Au-PEG_{107} is due to the dense grafting around the gold core and hence the change in the refractive index around the particle. The concentration of the AuNPs in the experimental solutions is $c_{\mathrm{NP}} = 0.2$ nM.

The previously described particles were used for studying the interactions with PDMS-*b*-PMOXA polymersomes with a hydrodynamic radius $R_{h,ves} = 135 \pm 3$ nm. All experiments were conducted in dilute aqueous solutions with a polymer concentration of $c_P = 3.6 \times 10^{-2}$ gL^{-1} (5.5×10^{-6} μM). The aggregation number of one vesicle is $N \approx 125000$, resulting in an overall vesicle concentration of $c_{ves} = 0.045$ nM. Hence, the molar ratio of AuNPs to vesicles is $\approx$ 5:1.

All PCS experiments were conducted at nanomolar concentrations because of the LSPR enhanced scattering intensity of the AuNPs. Prior to all experiments, particles and vesicles were characterized separately in aqueous solutions. Since vesicles are perfectly spherical and do not show any intrinsic anisotropy, only polarized scattering intensity $R_{VV}(q)$ could be recorded. $R_{VV}(q)$ is strongly q-dependent due to the large vesicle size. The Guinier plots (not shown) are linear over the whole q-range and their slope result in a radius of gyration of $R_g = 128 \pm 2$ nm. In contrast, $R_{VV}(q)$ of the AuNPs is almost flat due to the small particle size, and VH-scattering is detectable. $R_{VH}(q)$ is virtually flat and the orientation relaxation functions $C_{VH}(q,t)$ exhibit a single exponential decay with relaxation rate $\Gamma_{VH}(q) = 6D_r + q^2 D_t$. The relaxation functions of the AuNPs $C_{VV}(q,t) = a_{VH} exp(-\Gamma_{VH} t) + a_{iso} exp(-D^t q^2 t)$ are two-step decays, consisting of a slow, purely isotropic component with amplitude a_{iso} and a weak fast decay with amplitude a_{VH}. The translational diffusion processes allow a precise determination of D^t from the slope of the linear dependence, $\Gamma_{VV}(q) = q^2 D^t$, and D^r is directly obtained from the intercept of the rate $\Gamma_{VH}(q \to 0)$. Figure 4.17, Figure 4.18, Figure 4.19 and Figure 4.20 show all experimental PCS data for all three different interaction scenarios, which will be discussed in detail in the following. The data of the mixture of vesicles and AuNPs is represented by red symbols, data of only vesicles by blue symbols, and data of only AuNPs by black symbols. Data from VV and VH scattering is distinguished by solid and open symbols, respectively.

4.3.1.1 No Interactions Between Vesicles and Nanoparticles

Figure 4.17a shows the experimental SLS data for vesicles and Au-CTAB. The VV scattering intensity of the mixture (red solid squares) matches the sum of the two intensity

contributions (dashed line) from the individual vesicles and AuNPs. This indicates that there is no interaction between the two species and that they are scattering independently from each other. The depolarized scattering intensity $R_{\mathrm{VH}}(q)$ of the mixture (red open squares) is the same as $R_{\mathrm{VH}}(q)$ of the particles alone. It can therefore be assumed, that neither the size nor shape of the vesicles and of the particles changed upon mixture of both substances. This is confirmed by both VV and VH relaxation functions of the mixture at different q's (Figure 4.20a). $C_{\mathrm{VV}}(q,t)$ was fitted using a double exponential decay function with all parameters free. For small angles ($q = 6.85 \times 10^{-3}$ nm^{-1}), $C_{\mathrm{VV}}(t)$ of the mixture (red) is consistent with $C_{\mathrm{VV}}(t)$ (blue) of the pure vesicle solution, since $R_{\mathrm{VV}}(q)$ of the vesicles dominate at low q's but strongly decreases at high q's (see Figure 4.17a). For larger scattering angles ($q = 2.55 \times 10^{-2}$ nm^{-1}), polarized scattering of the particles dominate, and hence $C_{\mathrm{VV}}(q,t)$ of the mixture is equal to $C_{\mathrm{VV}}(q,t)$ of the particles (not shown). The relaxation functions $C_{\mathrm{VH}}(q,t)$ of the mixture are all identical with the relaxation functions of the AuNPs.

Figure 4.17b) shows the relaxation rates $\Gamma_{\mathrm{VH}}(q)$ and $\Gamma_{\mathrm{VV}}(q)$. The slow component of the double decay fit of $C_{\mathrm{VV}}(t)$ of the mixture (crossed red squares) corresponds to $\Gamma_{\mathrm{VV}}(q)$ of the vesicles, whereas the fast component of the double decay fit of the mixture (solid red squares) corresponds to $\Gamma_{\mathrm{VV}}(q)$ of the nanoparticles (inset Figure 4.17b). The amplitude of the slow relaxation process decreases with increasing q's, whereas the amplitude of the fast process increases. For VH scattering, $\Gamma_{\mathrm{VH}}(q)$ of the mixture always corresponds to $\Gamma_{\mathrm{VH}}(q)$ of the single AuNPs. R_{h} and R_{r} were computed from D^{t} and D^{r}, respectively, and are listed in Table 4.9. R_{r}, assigning to the rotational radius of the gold particle alone, is almost identical to R_{r} of the particle alone (Table 4.8). Due to the q-dependency of D^{t}, two values for R_{h} could be obtained, one for low q's ($R_{\mathrm{h}} = 143 \pm 8$ nm) and one for high q's ($R_{\mathrm{h}} = 21.3 \pm 0.5$), corresponding to the vesicles and to the particles, respectively. Again, these values are consistent with the measurements of the vesicles and particles alone. The numbers in the brackets in Table 4.9 indicate the difference to the original sizes.

The coexistence and hence the lack of interactions between both species is due to electrostatic repulsions of positively charged vesicles and positively charged particles.

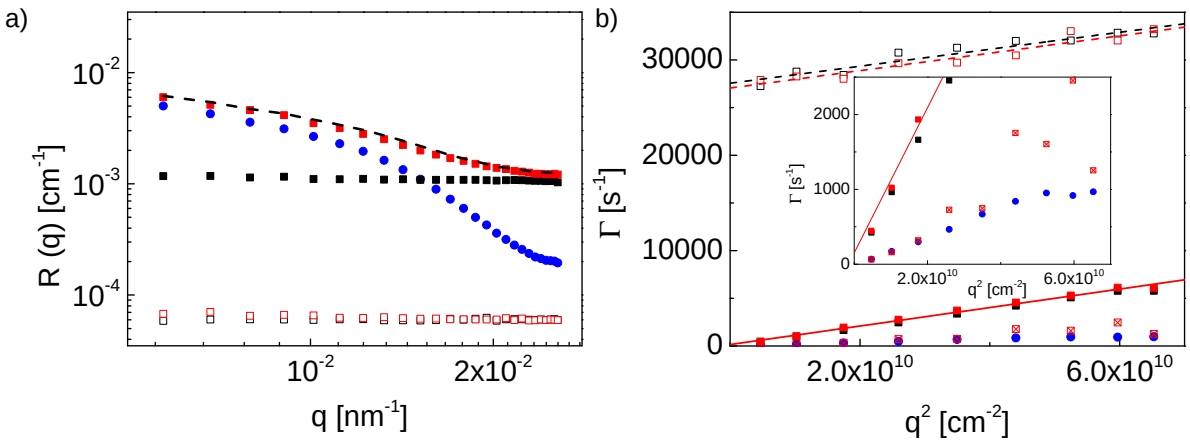

Figure 4.17: *a) Time-average absolute Rayleigh ratio for polarized $R_{VV}(q)$ (solid symbols) and depolarized $R_{VH}(q)$ (open symbols) light scattering from a dilute ($c = 0.036\ gL^{-1}$, $c_M = 0.6$ nM) aqueous suspension of PDMS-b-PMOXA vesicles (diameter $d \approx 250$ nm) and positively charged Au nanospheres (diameter $d = 44$ nm) stabilized with CTAB as a function of the scattering wave vector, q. The data of the mixture is represented by red symbols, data of the vesicles by blue symbol, and data of the NPs by black symbols. The sum of $R_{VV}(q)$ of both vesicles and NPs is represented by the dashed line. b) Relaxation rates Γ for slow (VV, solid symbols) and fast (VH, open symbols) components according to the color code in a). The inset shows an enlargement of the plot for low Γ. The slow component of the double decay fit of $C_{VV}(t)$ is depicted in red crossed squares, the fast component of the double decay fit is depicted in solid red squares.*

As shown by ζ-potential measurements (see Table 4.8), both species exhibit a positive surface charge (+ 27.5 mV and + 53.9 mV for polymersomes and Au-CTAB, respectively). Consequently, no interactions between vesicles and CTAB-functionalized AuNPs are possible.

4.3.1.2 Decoration of Vesicles with Nanoparticles

The same mixing experiments were conducted for vesicles and Au-PEG$_{107}$-NPs, which exhibit a neutral surface charge (ζ-potential is ≈ 0 mV). The PCS data is shown in Figure 4.18. This mixture shows totally different behavior than the mixture characterized above. As can be seen from Figure 4.18a, $R_{VV}(q)$ of the mixture (red) is significantly

higher than the sum (dashed line) of $R_{VV}(q)$ of vesicles (blue) and $R_{VV}(q)$ of AuNPs (black) and drops strongly at high q's. This indicates that vesicles and particles are interacting with each other, and that the formed species are larger in size than the individual species alone. $R_{VH}(q)$ (mixture) slightly varies from $R_{VH}(q)$ (AuNPs) and is slightly q-dependent. The experimental scattering profiles were also compared to the theoretical form factors of different vesicle-NP configurations (theoretical details can be found in Appendix subsection B.5). The decoration scenario was achieved by placing between 1 and 5 nanoparticles at the surface of the vesicle, such that their surfaces were in contact. The results suggest that the profiles shift upwards as the number of decorated nanoparticles increases (data not shown). A remarkable agreement between experimental mixture and a 2-nanoparticle-decorated scenario was found (solid line in Figure 4.18). Experimentally, however, an ensemble average over the different intensities is to be expected. The computed intensity profile at high q's result from the curvature of the system. Parametrization of the vesicle and nanoparticle radii, as well as polydispersity, may affect the location of this feature.

As already mentioned, $R_{VH}(q)$ is slightly q-dependent. The VH-scattering intensity gives rise to detailed information on the anisotropy of the decoration mechanism. Following Horn and coworkers [Hor51, Hor55], a supramolecular assembly with a set of polarizabilities α, β, and γ along each Cartesian direction x, y, and z, respectively, was associated (details see Appendix subsection B.5). By extrapolating the experimental data to $q = 0$, an anisotropy coefficient $\delta \approx 0.05$ was found, which translates to a ratio of polarizabilities $\beta/\alpha \approx 0.86$. Alternatively, the inertia tensor of different conformations of the decorated supramolecular assembly was measured [The85]. The density ratio between gold and polymersome material was estimated to 25. Interestingly, the results show that the one-nanoparticle mixture provides $\beta/\alpha \approx 1.25$. For the two-nanoparticle mixture, two geometries were considered: the two NPs placed at opposite poles of the vesicles, $\vartheta = 180°$ (where ϑ is the polar angle in the spherical coordinates of the vesicle, setting the first nanoparticle at $\vartheta = 0$), and a $\vartheta = 90°$ angle between the two nanoparticles with respect to the center of the vesicle. While the former case provides $\beta/\alpha \approx 1.45$, the $\vartheta = 90°$ scenario results in $\beta/\alpha \approx 0.85$, in excellent agreement with the above-mentioned

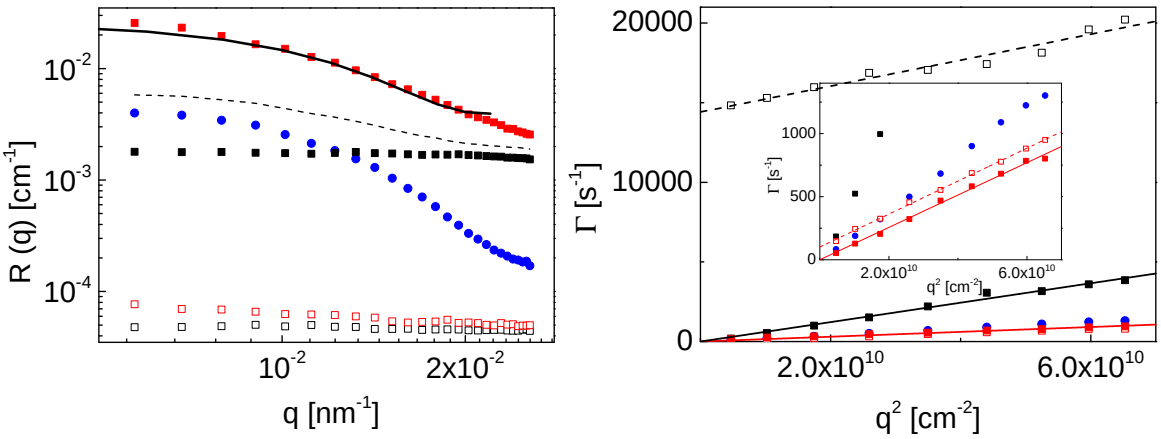

Figure 4.18: *a) Time-average absolute Rayleigh ratio for polarized $R_{VV}(q)$ (solid symbols) and depolarized $R_{VH}(q)$ (open symbols) light scattering from a dilute aqueous suspension of PDMS-b-PMOXA vesicles (diameter $d \approx 250$ nm) and slightly negatively charged Au nanospheres (diameter $d = 44$ nm) stabilized with PEG_{107} as a function of the scattering wave vector, q. The data of the mixture is represented by red symbols, data of the vesicles by blue symbol, and data of the NPs by black symbols. The sum of $R_{VV}(q)$ of both vesicles and NPs is represented by the dashed line. The calculated scattering profile for two decorated nanoparticles is represented by the black solid line. b) Relaxation rates Γ for slow (VV, solid symbols) and fast (VH, open symbols) components according to the color code in a). The inset shows an enlargement of the plot for low Γ.*

analysis of the polarized light scattering data. Moreover, this result is in agreement with the entropic force driving the decoration of a second nanoparticle at an angle ϑ close to 90°, as found in the Jacobian term in spherical coordinates: $\sin\vartheta$.

The relaxation rate $\Gamma_{VV}(q)$ of the mixture is lower than $\Gamma_{VV}(q)$ of the vesicles (inset Figure 4.18b) and the computed R_h increased from 135 nm to 190 nm, which corresponds well to the sum of vesicular radius and NP's diameter. This also indicates decoration of vesicles by nanoparticles. $\Gamma_{VH}(q)$ is completely different from $\Gamma_{VH}(q)$ of the AuNPs and results in $R_r = 207$ nm (Table 4.9), and hence R_h and R_r are consistently larger than the vesicles alone. This is also shown by the relaxation functions $C_{VV}(q,t)$ and $C_{VH}(q,t)$ (Figure 4.20b). $C_{VV}(t)$ of the mixture decays slower than $C_{VV}(t)$ of the vesicles at all scattering angles and $C_{VH}(t)$ of the mixture deviates much from $C_{VH}(t)$ of the particles.

The slight discrepancy of R_h and R_r might be due to the anisotropic shape of the decorated vesicle-NPs constructs. As shown in the previous paragraph, the two nanoparticles decorating the vesicle need to be placed orthogonal to each other. Therefore, the shape of the construct differs from a perfect sphere and Stokes-Einstein equation suffers from inaccuracy.

4.3.1.3 Uptake of Nanoparticles into Vesicles

Another scenario was obtained upon mixing vesicles with negatively charged Au-Citrate nanoparticles. It can be seen from Figure 4.19 that $R_{VV}(q)$ (mixture) is much higher than the sum of vesicles and AuNPs (dashed line), but the decrease of the intensity is weaker than for the mixture of vesicles and Au-PEG_{107} (Figure 4.18a). The latter indicates that the formed species is smaller than the decorated vesicle from the previous experiment. $R_{VH}(q)$ (mixture) and $R_{VH}(q)$ (AuNPs) are almost identical.

Similar to the decoration scenario, computational modeling for the uptake scenario was performed. The uptake mechanism leads to a consumption of the polymeric material of the vesicle by the endocytosed nanoparticles. This consumption was modelled by systematically adding a shell of scattering length density ρ_{ves} around each nanoparticle, using the same thickness $d = 20$ nm. Furthermore, the loss of polymer material in the vesicle itself was considered by decreasing the vesicle's radii. For simplicity, both radii were reduced by 10 nm for any number of nanoparticles considered. In fact, it is shown that the results are largely insensitive to the exact decrease in radius (data not shown). Nanoparticles were placed systematically such that the polymer material surrounding them lied at the inner radius of the vesicle. The solid line in Figure 4.19 shows that, in the range $0.01 < q < 0.02$ nm^{-1}, there is good agreement between the experimental data and an unweighted average between 1- and 2-nanoparticle profiles. Following the results from the decoration mechanism, the more nanoparticles incorporated into the vesicle, the higher is the shift in the scattering profile (data not shown).

$\Gamma_{VV}(q)$ of the mixture deviates slightly from $\Gamma_{VV}(q)$ of the vesicles (Figure 4.19b), but $\Gamma_{VH}(q)$ is completely different from $\Gamma_{VH}(q)$ of the AuNPs. The computed radii are $R_h = 123$ nm and $R_r = 128$ nm and hence symmetrical shape of the assumed species is assumed

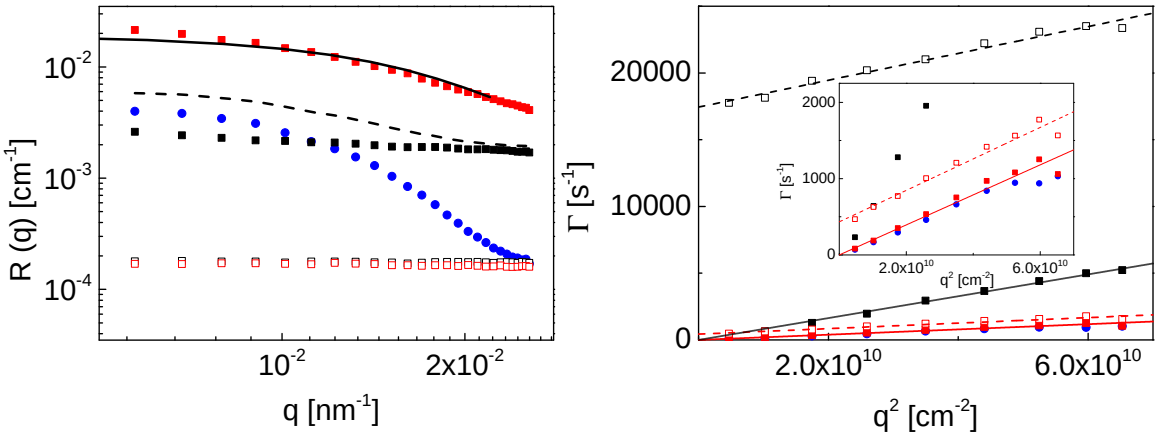

Figure 4.19: *a) Time-average absolute Rayleigh ratio for polarized $R_{VV}(q)$ (solid symbols) and depolarized $R_{VH}(q)$ (open symbols) light scattering from a dilute aqueous suspension of PDMS-b-PMOXA vesicles (diameter $d \approx 250$ nm) and negatively charged Au nanospheres (diameter $d = 44$ nm) stabilized with citrate as a function of the scattering wave vector, q. The data of the mixture is represented by red symbols, data of the vesicles by blue symbol, and data of the NPs by black symbols. The sum of $R_{VV}(q)$ of both vesicles and NPs is represented by the dashed line. The calculated scattering profile for an unweighted average of 1- and 2-nanoparticle profiles is represented by the black solid line. b) Relaxation rates Γ for slow (VV, solid symbols) and fast (VH, open symbols) components according to the color code in a). The inset shows an enlargement of the plot for low Γ.*

Table 4.9: *Characteristic dimensions of mixtures of vesicles and Au nanospheres.*

	R_h [nm]	R_r [nm]	λ_{max} [nm]
Ves + Au-CTAB	21.3 ± 0.5 (-1.5) / 143 ± 8 (+8)	33.1 ± 0.3 (+0.4)	525 (+1)
Ves + Au-PEG$_{107}$	190.0 ± 12 (+55)	207 ± 13 (+167)	530 (+4)
Ves + Au-Citrate	123 ± 3 (-12)	128 ± 4 (+93)	532 (+8)

(see Table 4.9). The formed species are approx. 12 nm smaller than the original vesicles and again the AuNPs need to be attached to the vesicle due to the low D^{r} from depolarized scattering. Since the obtained radii are smaller than the size of the original vesicle, the AuNPs cannot decorate the vesicles as in the previous experiment. Smaller size of the species as well as consistent diffusion rates from VV and VH lead to the assumption that the AuNPs need to be incorporated into the polymersomes. Due to the endocytotic uptake process, membrane needs to be consumed upon particle invagination, and hence the resulting filled vesicle must decrease its size. The amount of consumed membrane relates to approx. 3 wrapped AuNPs, which is in very good agreement with the molar ratio of vesicles and particles and the results obtained from computational modeling of the SLS data. This experiment proves the uptake of negatively charged (citrate-stabilized) AuNPs into polymersomes. Further, if the endosomes diffused freely within the vesicle, the obtained R_{r} would be equal to the radius of the AuNPs plus the thickness of the polymeric membrane ($d = 16$ nm). Due to $R_{\mathrm{h}} \approx R_{\mathrm{r}}$, one can assume that no detachment of the endosomes from the membrane happened, and hence the AuNPs must stick to the inner side of the vesicle. Consequently, one can distinguish scenario 3a and 3b from Figure 4.16 by a single PCS experiment, since the AuNPs serve as tracers within the vesicles. The observed scenario 3b (uptake of particle but remaining tethered to the membrane) has also been predicted by theoretical simulations, assuming homogeneous membrane surfaces [Smi07]. According to these simulations, uptake of particles and successive detachment from the membrane is only possible for inhomogeneous membranes, consisting of an adhesive domain in an otherwise non-adhesive membrane. The vesicles used in this study, however, exhibit a homogeneous membrane surface which is adhesive to the Au-Citrate particle's surface due to attractive electrostatic interactions.

In contrast to the neutral Au-PEG_{107} nanoparticles, where decoration of the vesicles was achieved, the Au-citrate NPs are clearly negatively charged. Consequently, attractive electrostatic interactions between positively charged polymersomes and negatively charged particles are possible. Since the Au-citrate NPs are taken up into the interior of the vesicle, the attractive interactions must be large enough to compensate the loss of bending energy upon membrane deformation.

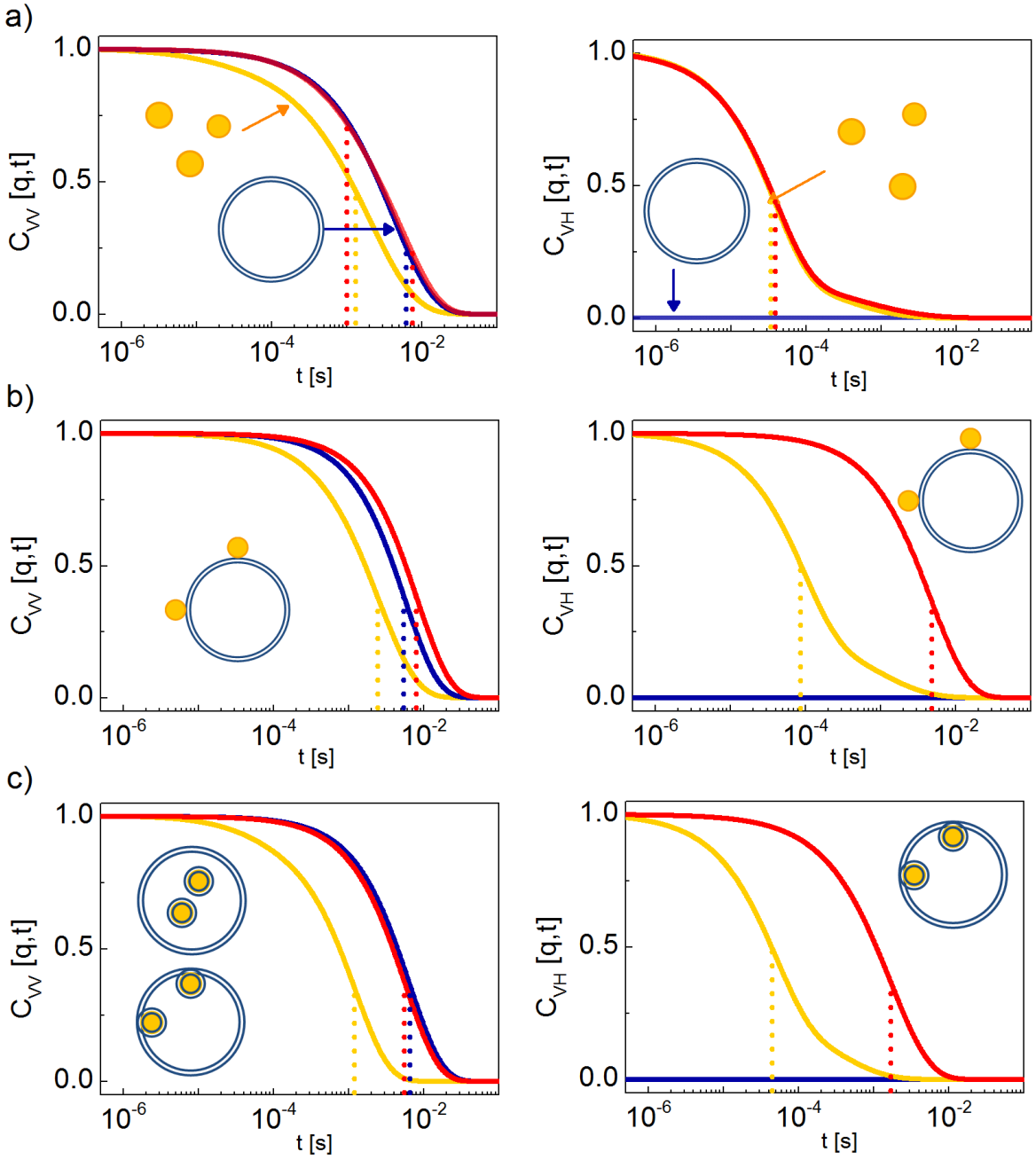

Figure 4.20: *Relaxation functions of the three different systems (a) no interactions, b) decoration, c) uptake) at* $q = 1.01 \times 10^{-2}$ nm^{-1}, *recorded for VV and VH polarization, respectively. The solid lines indicate the theoretical representation (see text) of the experimental functions. Mixture: red, vesicles: blue, NP: yellow. The PCS experiment was performed with a coherent laser light at* $\lambda = 632$ nm, *far above* λ_{max} *of the AuNPs.*

4.3.2 Supporting the Results Obtained from PCS

Based on the present PCS experiments, it became possible to discriminate among the four different scenarios from Figure 4.16. Due to the inherent anisotropy and the LSPR enhanced scattering of the gold particles, it is possible to detect vesicles and AuNPs at the same time, facilitating the study of these complex systems. It has also been shown that we are able to regulate the interactions between NPs and vesicles by simply modifying their surface. Two additional methods were chosen to support the results obtained from PCS: (i) cryo-TEM, for providing a more descriptive image of the different scenarios, and (ii) UV/Vis, for investigating the change in the chemical surrounding of the AuNPs.

4.3.2.1 Images from Cryo-TEM

In order to support the PCS results, cryo-TEM pictures of the mixtures were recorded [Ber14]. Figure 4.21a shows that there is no interaction between vesicles and Au-CTAB NPs and that both species coexist. Figure 4.21b shows decorated vesicles with Au-PEG_{107} NPs. One can clearly see that the particles are not engulfed by the membrane, although they seem to slightly cave into the membrane. Figure 4.21c and Figure 4.21d show the uptake of Au-Citrate NPs into the vesicles, clearly displaying the membrane around the particles. Some of those endosomes seem to be attached to the membrane, while others seem the diffuse freely within the vesicle. However, as it was shown by PCS, only one species was detected in depolarized PCS, and therefore no free AuNPs or gold-endosomes can exist. Since cryo-TEM shows the transmission and hence a two-dimensional picture only, the apparent free gold endosomes must be anyhow attached to the sides of the membrane.

4.3.2.2 Impact of Uptake on UV/Vis

The extinction spectra of all samples were measured and the resonance wavelengths are given in Table 4.9. The numbers in brackets specify the difference to the resonance wavelengths of the AuNPs alone. Pure vesicle solutions do not absorb light in the UV/Vis range, whereas plasmonic particles show a characteristic resonance wavelength, which is very sensitive to changes in the refractive index of the surrounding medium. Therefore,

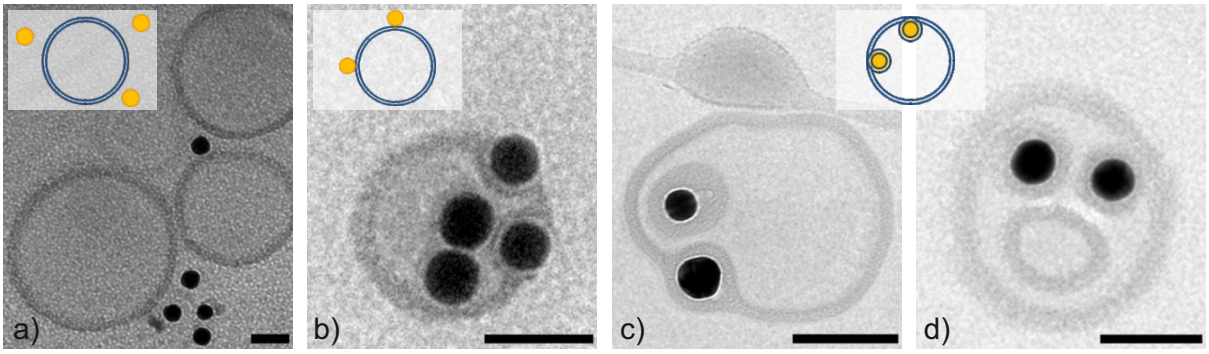

Figure 4.21: *Cryo-TEM images of the three different interaction scenarios of vesicles and nanoparticles. a) Ves + Au-CTAB: No interactions between vesicles and particles. b) Ves + Au-PEG$_{107}$: Decoration of vesicles, but no internalization of the particles into the interior of the vesicles. c) and d) Ves + Au-Citrate: Uptake of nanoparticles into vesicles and complete wrapping of the particles by the polymer membrane. Due to the limitations of cryo-TEM to two dimensions only, one can not differentiate endosomes which are bound to the inner side of the membrane or which diffuse freely within the vesicle. The scale bar corresponds to 100* nm. *All images were recorded by Max Bernhardt [Ber14].*

recording the extinction spectra of vesicle-nanoparticle mixtures, is a sensitive measurement for the AuNPs and their chemical surrounding. As can be seen from Table 4.9, the shift of the extinction maximum of for mixtures of Au-CTAB particles and vesicles is neglectable (+1). However, the shift slightly increases for Au-PEG$_{107}$ particles (+4 nm) and Au-Citrate particles (+8 nm, data shown in Figure 4.22a). Theoretical extinction spectra of gold nanospheres in different media were calculated by Gaëtan Lévêque at the University of Lille. It was found that, assuming a refractive index of the membrane of $n = 1.45$ and a thickness of $d = 16$ nm, a fully coated particle would experience a resonance wavelength shift of 8 nm, whereas a third- or half-coated particle would only be shifted by 3-4 nm(see Figure 4.22b). These calculations are in excellent agreement with the experimentally observed red-shifts of the plasmon resonance wavelengths. In fact, as observed in PCS, the uptaken Au-citrate particles should be fully wrapped by the membrane, and were therefore shifted by 8 nm. In contrast, the Au-PEG$_{107}$ particles should be maximally half-covered by the membrane, and, consequently, were shifted by only 4 nm.

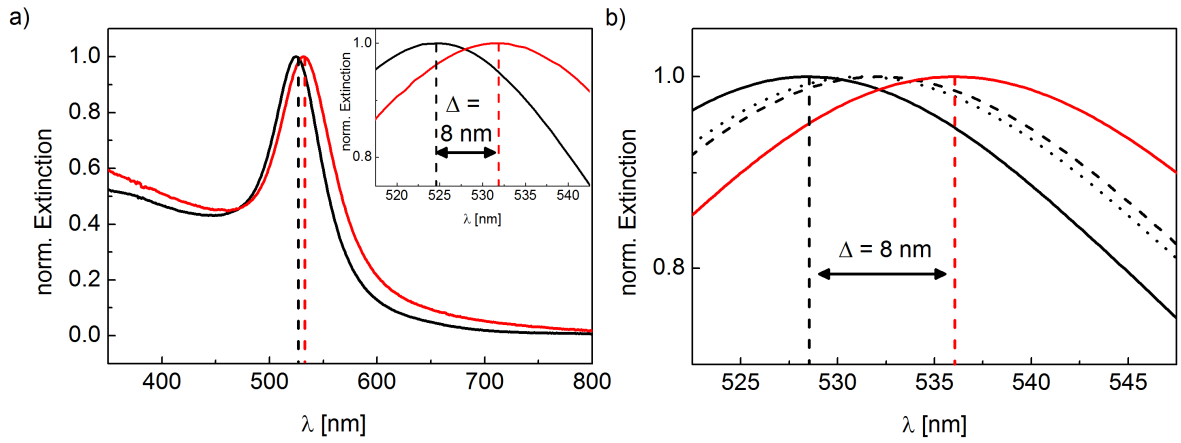

Figure 4.22: *a) Extinction spectra of a dilute suspension of citrate-AuNPs (black line) and of Au-Citrate with polymersomes (red line). The inset shows an enlargement of the extinction spectrum from 517.5 to 542.5* nm. *b) Calculated extinction spectra of AuNPs in different media with different refractive indices: particle in pure water ($n = 1.33$, black solid line), particle with a 16* nm *thick shell with $n = 1.45$ (third coated: dotted line; half-coated: dashed line; fully coated: red line).*

Summing up the experimental techniques, PCS, UV/Vis and cryo-TEM are very powerful for describing the interactions of AuNPs with polymersomes. Thanks to the unique physical and optical properties, their detectability in depolarized light scattering at nanomolar concentrations, their sensitivity to changes in the chemical surrounding, plus their good chemical modifiability, gold nanoparticles are perfectly suitable for sensing interactions at (biological) interfaces. Possible utilizations would reach from nanomedical to sensing applications.

4.4 Gold Nanorods: Characterization and Uptake

Besides spherical Au nanoparticles, also rod-shaped Au particles have been studied in order to investigate shape-dependent uptake of nanoparticles into polymersomes. Au nanorods (AuNRs) with different aspect ratios ranging from 3.0 to 4.3 were purchased from NanoSeeds^{TM} and were characterized by surface plasmon resonance enhanced dynamic polarized and depolarized light scattering, UV/Vis spectroscopy and TEM. Due to their high asphericity, nanorods show a strong anisotropic scattering and hence both translational and rotational diffusion coefficients can be measured. Freshly synthesized Au nanorods are typically stabilized by a double layer of the surfactant cetyltrimethylammonium bromide(CTAB), which induces a positive surface charge to the particles. However, negative surface charges are required for attractive interactions between particles and vesicles, and hence further surface functionalization with 11-mercaptoundecanoic acid (MUA) was necessary. Uptake experiments were conducted similar to the previous section 4.3 (Uptake of Gold Nanospheres into Vesicles).

4.4.1 Surface Modification of Au-Nanorods

Surface modification of Au nanorods is principally more difficult than of Au nanospheres [Shi13]. After synthesis, AuNRs bare a positive surface charge due to electrostatic stabilization by CTAB molecules. CTAB molecules bind strongly to the long sides of the nanorods, and molecules at the short edge of the particles are removed much easier than the ones binding to the long side. Consequently, nanorods tend to aggregate during the surface modification process. In order to obtain a negative surface charge, one must first replace the positively charged CTAB molecules by a transitional, but negatively charged surfactant. Here, sodium dodecyl sulfate (SDS) was used according to a procedure by Sebastian Harms at the University of Mainz. First, AuNRs were centrifuged to remove excess CTAB. The particles were then resuspended in a 0.3% SDS solution and sonnicated for 3 h, while keeping the particles at room temperature. The AuNRs were centrifuged again and the supernatent was replaced by a 5 mM MUA solution in NaOH. The particles

were incubated over night at room temperature and centrifuged for purification and stored in the fridge.

4.4.2 Characterization of Au-Nanorods

4.4.2.1 Bare Au-Nanorods

The bare (CTAB) AuNRs as well as the MUA-functionalized AuNRs were characterized by several techniques. Length l and diameter d were obtained from TEM. Details can be found in Table 4.10. The given numbers are averages of at least 100 different particles. The aspect ratio (AR) was calculated by dividing l over d. The lengths of all samples is $l \approx 70$ nm and the error is in the range of 10-15%. The diameter decreases from $d \approx 23$ nm for the thickest rods to $d \approx 17$ nm for the thinnest rods. Consequently, the aspect ratio increases from 3.0 to 4.3. The percentage of rods over other structures is very high and almost 100% for all samples except for samples 1 and 4. According to their measured sizes in TEM, samples 3 and 4 are very similar to each other, but sample 3 has a higher percentage of rods.

UV/Vis measurements reveal the two extinction maxima of the samples. The position of the longitudinal peak is red-shifted with increasing aspect ratio of the rods, whereas the transversal peak is a rather insensitive measurement for the short side of the rods (see subsection 2.3.2). As can be seen from Table 4.10, the position of the first (transversal) maximum is almost constant for all samples ($\lambda_{max} \approx 510$ nm), whereas the position of the second (longitudinal) maximum increases from $\lambda_{max} \approx 700$ nm to $\lambda_{max} \approx 850$ nm. As expected from TEM, the measured λ_{max} of sample 3 and 4 are almost similar. However, the width of the longitudinal peak is more narrow for sample 3 than for sample 4 as can be seen from the UV/Vis spectra in Figure 4.23a. In addition, the transversal peak of sample 4 shows a shoulder around $\lambda \approx 575$ nm. Consequently, sample 4 is not used for further uptake experiments. Sample 5 also shows a slight shoulder around $\lambda_{max} \approx 575$ nm, which might be due to the presence of spheres with a larger diameter. However, TEM measurements confirm the presence of 99% rods in the sample.

Table 4.10: *Characteristic dimensions (length l, thickness d, aspect ratio AR and extinction maxima λ_{max}) of CTAB-stabilized Au nanorods as determined by TEM and UV/Vis measurements. The last column gives the percentage of rods in the sample, as obtained from evaluating > 100 rods.*

sample	l [nm]	d [nm]	AR	λ_{max} [nm]	rods [%]
1	68.2 ± 10.0	23.3 ± 4.5	3.0 ± 0.5	512 / 714	90
2	73.7 ± 8.3	22.9 ± 2.8	3.2 ± 0.4	511 / 761	97
3	63.7 ± 9.6	16.8 ± 2.8	3.9 ± 0.7	510 / 797	95
4	67.1 ± 8.6	17.6 ± 2.8	3.9 ± 0.8	512 / 813	89
5	71.4 ± 8.8	17.0 ± 2.2	4.3 ± 0.7	511 / 859	99

All AuNRs were also characterized by PCS. Dynamic polarized and depolarized light scattering was used to determine D^{t} and D^{r} (see Table 4.11). The depolarization ratio R_{VH}/R_{VV} was measured with a laser with wavelength $\lambda = 632$ nm. The depolarization ratio decreases with increasing aspect ratio of the samples, although the reverse trend was expected. According to theory [Hor51, Hor55], the experimental values for R_{VH}/R_{VV} are too high except for sample 5, and consequently the equation for β/α cannot be solved (details see Appendix subsection B.5). However, similar values were already reported previously [Hag13]. Possibly, the scattering intensities are very sensitive to the position of the longitudinal extinction maxima, and hence the ratio decreases when the laser is more off-resonance. In addition, the anisotropy recorded in the depolarization ratio might not only arise from its form anisotropy, but also from internal anisotropy such as crystallinity and anisotropic graftings, as already observed for gold nanospheres in subsection 4.2.2 (Surface Asymmetry of Coated Spherical Au-NPs).

From D^{t} and D^{r}, one can calculate the hydrodynamic and the rotational radii (R_{h} and R_{r}, respectively), using Stokes-Einstein equation and assuming a spherical shape of the particles. More precisely, the volume of the sphere with radius R_{h} or R_{r} is equal to the hydrodynamic volume of the measured rods. However, R_{h} and R_{r} are smaller than the length obtained by TEM. This is due to the large aspect ratio of the rods,

Table 4.11: *Characteristic dimensions (depolarization ratio R_{VH}/R_{VV}, translational and rotational diffusion coefficients D^t and D^r, respectively) of CTAB-stabilized Au nanorods as determined by PCS. The deviation in L between l obtained from TEM and L from eq 4.1 are shown in brackets.*

sample	R_{VH} / R_{VV}	D^t [$\times 10^{-12}$ m^2s^{-1}]	D^r [$\times 10^3$ s^{-1}]	L [nm] (eq 4.1)
1	0.412 ± 0.004	8.09 ± 0.06	6.74 ± 0.02	70.8 (+ 2.6)
2	0.407 ± 0.007	5.99 ± 0.21	5.34 ± 0.11	69.4 (- 4.6)
3	0.357 ± 0.009	6.48 ± 0.22	9.71 ± 0.18	55.6 (- 8.1)
4	0.313 ± 0.002	7.18 ± 0.05	8.10 ± 0.07	64.0 (- 3.1)
5	0.232 ± 0.003	6.52 ± 0.05	7.17 ± 0.13	65.9 (- 5.5)

and therefore the large discrepancy between the diffusion coefficients along and normal to the rod axis, $D_{||}$ and $D_{\perp}$, respectively. The experimental $D^t = (D_{||} + 2D_{\perp})/3$ (see subsection 2.3.3). D^r is derived from $\Gamma_r = 6D^r + D^t q^2$ and it describes the rotation around the two short axes or the reorientation of the long axis. Due to rod-like symmetry, D^r is single rotational diffusion. Both R_r and R_h are hydrodynamic radii and cannot be directly compared with the TEM dimensions. Under the assumption of stick boundary conditions, hydrodynamic theory can be employed to estimate the real sizes.

$$\frac{G(AR)}{F(AR)} = \frac{D^r}{D^t} \cdot \frac{L^2}{9} \tag{4.1}$$

The values for $G(\mathrm{AR})/F(\mathrm{AR})$ are almost independent of the aspect ratio (see Figure 4.23b). L was estimated with fixed values for $G(\mathrm{AR})/F(\mathrm{AR})$ according to the aspect ratio obtained from TEM. Mathematical expressions for $F(\mathrm{AR})$ and $G(\mathrm{AR})$ can be found in subsection 2.3.3 (Dynamics of Gold Spheres and Nanorods). The obtained values for L are listed in Table 4.11 and are close to the obtained l from TEM (see deviations in the brackets). However, no reasonable values for $G(\mathrm{AR})$ nor for $F(\mathrm{AR})$ were obtained using the values of L (open symbols in Figure 4.23b). All experimental values are significantly lower than the theoretical curves. The deviations might be due to hydrodynamic

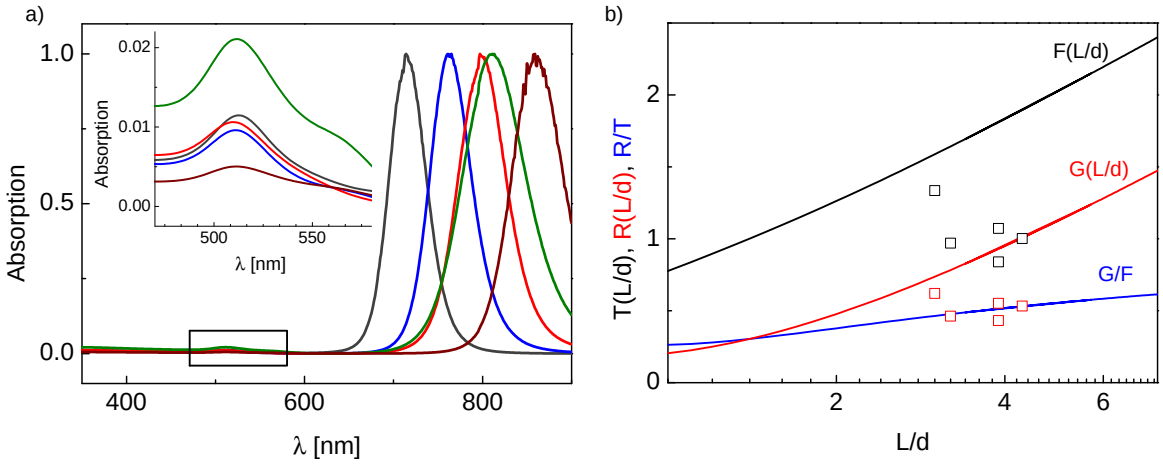

Figure 4.23: *a) Experimental absorption spectra for CTAB-functionalized AuNRs. The inset shows an enlargement of the transversal peaks from. Color code: sample 1 (grey), sample 2 (blue), sample 3 (red), sample 4 (green), sample 5 (brown). b) Translational (F(L/d)) and rotational (G(L/d)) functions as well as their ratio (G/F) as functions of the aspect ratio L/d computed for cylindrical rods using equations 2.19 and 2.20 from subsection 2.3.3 (solid lines). The estimated values for F(L/d) and G(L/d) are represented by the open symbols using the values of L obtained from Equation 4.1.*

boundary conditions, and/or the validity of the model. Similar deviations have already been reported in literature [Gli12, Hag13].

The two correlation functions C_{VV} (polarized) and C_{VH} (depolarized) as well as the relaxation rates Γ_{VV} and Γ_{VH} for all samples are shown in Figure 4.24. The single-step decay of C_{VH} and the double-step decay of C_{VV} can be well described by Equation 3.15 and Equation 3.16 in subsubsection 3.2.1.3 (Data Evaluation), respectively. The first (fast) decay of C_{VV}, which is associated with the rotational dynamics, is identical with the single decay of C_{VH}. This was shown by comparing Γ_{VH} with $\Gamma_{\mathrm{VV,fast}}$ (data not shown). Therefore, the double decay fit of C_{VV} was performed with fixed values for τ_1 and for β_1, as obtained from the single decay fit of C_{VH}. As can be seen from Figure 4.24a, the amplitudes of the fast decay of C_{VV} decreases with increasing aspect ratio of the rods. This finding is in good agreement with the scattered intensities R_{VV} and R_{VH} and their ratio (see Table 4.11). However, due to the rather similar size of the rods, no big

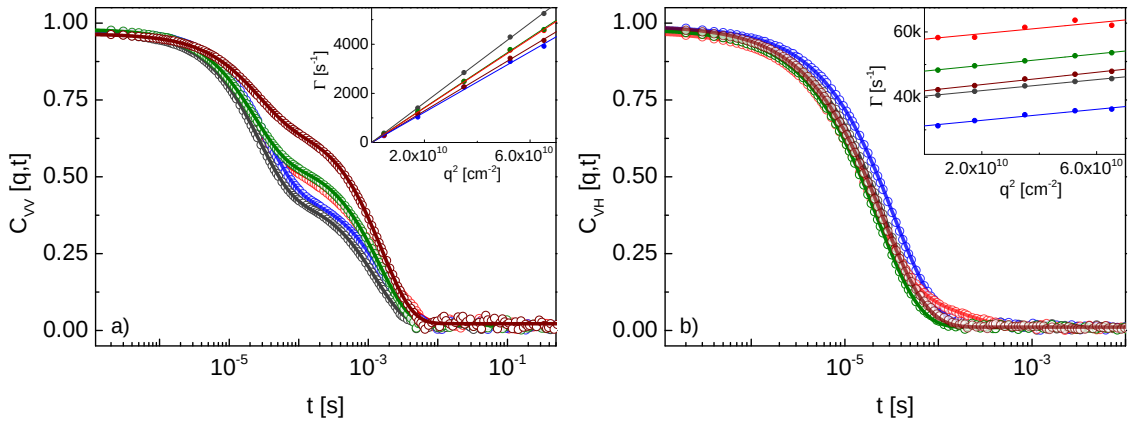

Figure 4.24: *Relaxation functions of five different CTAB-stabilized AuNRs at a wavelength of 632 nm and $q = 1.01 \times 10^{-2}$ nm^{-1}, recorded in the (a) VV (polarized) and (b) VH (depolarized) geometries. Color code: sample 1 (grey), sample 2 (blue), sample 3 (red), sample 4 (green), sample 5 (brown). The solid lines represent the fits to the experimental functions of $C_{VV}(q,t)$ (a) and $C_{VH}(q,t)$ (b). The insets show the relaxation rate Γ_{VV} of the slow process of $C_{VV}(q,t)$ (a) and the relaxation rate $C_{VH}(q,t)$ of the monomodal fast process of $C_{VH}(q,t)$ (b).*

differences in the decay times of C_{VH} can be observed. Here, plotting Γ_{VH} vs. q^2 is a better way for differentiating the measured rods (inset Figure 4.24b). In principle, the longer a nanorod, the slower is its rotational relaxation rate.

4.4.2.2 MUA-functionalized Au-Nanorods

All samples were surface-functionalized with 11-mercaptoundecanoic acid (MUA) by a procedure described in subsection 4.4.1. The freshly modified samples were characterized by the same techniques as before. Table 4.12 and Table 4.13 summarize the results obtained from TEM, UV/Vis and PCS. The position of the transversal maxima did not change upon functionalization, whereas the position of the longitudinal maxima was significantly blue-shifted. This can be either due to a change in the refractive index around the particles or due to a change in size of the particles. The refractive index of CTAB is $n = 1.435$, whereas the refractive index of MUA is $n = 1.463$ [Yu07a]. An increase in the refractive index causes a red-shift of the absorption peaks in UV/Vis. However, it needs to be considered that the organic grafts on the particle's surface are swollen in water and the

Table 4.12: *Characteristic dimensions (length l, thickness d, aspect ratio AR and extinction maxima λ_{max}) of MUA-stabilized Au nanorods as determined by TEM and UV/Vis measurements. The last column gives the percentage of rods in the sample, as obtained from evaluating > 100 TEM pictures. The numbers in brackets indicate the difference to the original (CTAB-stabilized) particles.*

sample	l [nm]	d [nm]	AR	λ_{max} [nm]	rods [%]
1	71.5 ± 9.1 (+3.3)	25.2 ± 4.7 (+1.9)	2.9 ± 0.5 (-0.1)	512 (±0) / 707 (-7)	96 (+6)
2	76.9 ± 7.2 (+3.2)	22.4 ± 3.1 (+0.5)	3.1 ± 0.6 (-0.1)	509 (-2) / 756 (-5)	96 (-1)
3	66.8 ± 16.2 (+3.1)	18.6 ± 2.9 (+1.8)	3.7 ± 1.0 (-0.2)	509 (-1) / 789 (-8)	97 (+2)
4	68.7 ± 11.1 (+1.6)	18.2 ± 3.2 (+0.6)	3.9 ± 0.9 (±0)	511 (-1) / 800 (-13)	91 (+2)
5	75.1 ± 8.7 (+3.7)	18.1 ± 2.5 (+1.1)	4.2 ± 0.8 (-0.1)	510 (-1) / 848 (-11)	97 (-2)

extent of both grafting and swelling affects the refractive index. Therefore, it is assumed that the refractive index around the MUA-functionalized particles is $n = 1.392$, whereas the refractive index of the CTAB double layer is $n = 1.414$ [Yu07a]. In addition, the thickness of a MUA monolayer is only $d = 1.69$ nm [Hae02], whereas CTAB assembles into bilayers of a thickness $d \approx$ 4-5 nm [Mur05]. Consequently, the blue-shift of the absorption maxima is due to a slight decrease of the refractive index around the particles as well as a decrease of the thickness of the organic layer around the particle. In addition, the widths of the longitudinal peaks are much broader after functionalization with MUA, which indicates an increase in polydispersity of the samples. Figure 4.25 shows a comparison between the UV/Vis spectra of the CTAB and the MUA functionalized samples.

TEM analysis of the modified nanorods revealed a marginal increase in the particle's width and length (see Table 4.12). However, the differences of the particle's dimensions

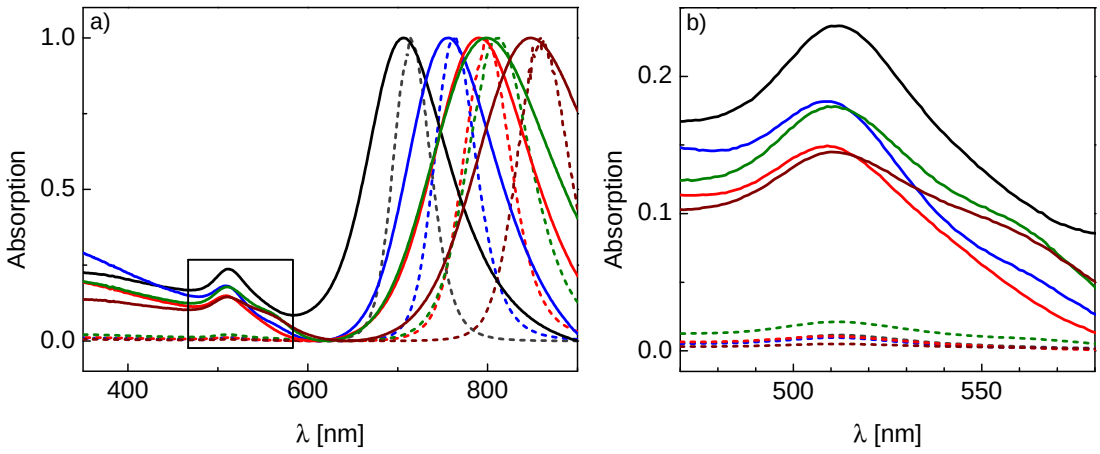

Figure 4.25: *a) Experimental absorption spectra for MUA-functionalized (solid lines) and CTAB-functionalized AuNRs (dashed lines). Color code: sample 1 (grey), sample 2 (blue), sample 3 (red), sample 4 (green), sample 5 (brown). b) shows an enlargement of the transversal peaks from $\lambda = 470$ nm to $\lambda = 580$ nm.*

are within the error. It is therefore assumed that the sizes of cores of the AuNRs did not change after functionalization. In TEM, the organic grafts cannot be seen due to low contrast.

As mentioned above, the thickness of the CTAB bilayer assembling around surfaces is $d \approx$ 4-5 nm [Mur05], whereas the thickness of the MUA monolayer on gold surfaces is only $d = 1.69$ nm [Hae02]. Therefore, a slight decrease of the AuNRs dimensions is expected for PCS measurements. As a matter of fact, the measured values for both D^{t} and D^{r} increase after functionalization, except for sample 1 (see Table 4.13). Therefore, samples 1 is not used for further uptake experiments. The correlation functions $C_{\mathrm{VV}}(q,t)$ and $C_{\mathrm{VH}}(q,t)$ as well as the relaxation rates Γ_{VV} and Γ_{VH} for all samples are shown in Figure 4.26. It can be noticed that the surface functionalization has a higher impact on the rotational than on the translational diffusion, especially for the nanorods with the highest aspect ratios (sample 4 and 5). This can be due to several reasons: 1) The boundary conditions can be different comparing CTAB-stabilized surfaces and MUA-grafted surfaces. 2) Lower grafting density around the tips of the nanorods, because grafting around the tip of the nanorod is more difficult than along the long edge of the rod. Although this effect could not be described quantitatively, this will have no effect

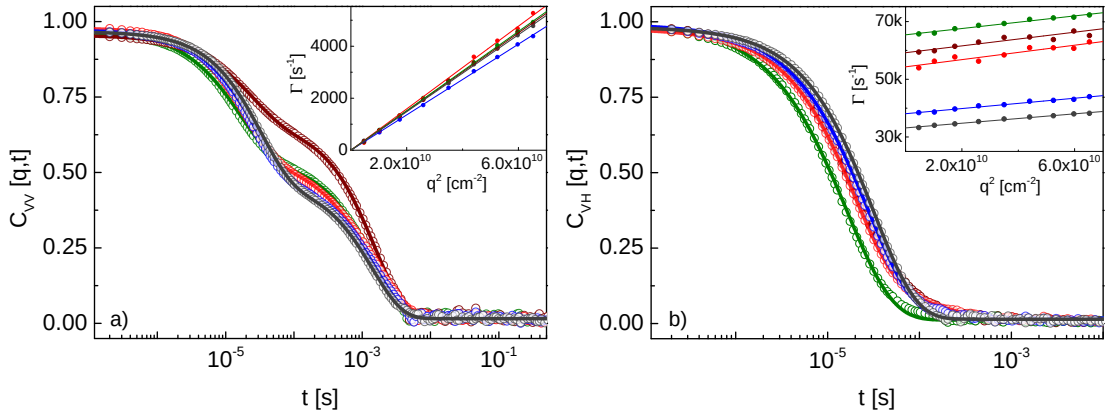

Figure 4.26: *Relaxation functions of five different MUA-functionalized AuNRs at a wavelength of 632 nm and* $q = 1.01 \times 10^{-2}\ nm^{-1}$*, recorded in the (a) VV (polarized) and (b) VH (depolarized) geometries. Color code: sample 1 (gray), sample 2 (blue), sample 3 (red), sample 4 (green), sample 5 (brown). The solid lines represent the fits to the experimental functions of* $C_{VV}(q,t)$ *(a) and* $C_{VH}(q,t)$ *(b). The insets show the relaxation rate* Γ_{VV} *of the slow process of* $C_{VV}(q,t)$ *(a) and the relaxation rate* $C_{VH}(q,t)$ *of the monomodal fast process of* $C_{VH}(q,t)$ *(b).*

on further experiments with vesicles and hence no further investigations were performed. In addition, the changes in the depolarization ratio R_{VH} / R_{VV} are rather small (up to 8%) and will therefore be neglected.

Table 4.13: *Characteristic dimensions (depolarization ratio* R_{VH}/R_{VV}*, translational and rotational diffusion coefficients* D^t *and* D^r*, respectively) of MUA-stabilized Au nanorods as determined by PCS. The numbers in brackets indicate the difference to the original (CTAB-stabilized) particles as presented in Table 4.11.*

sample	R_{VH} / R_{VV}	D^t [$\times 10^{-12}$ $m^2 s^{-1}$]	D^r [$\times 10^3$ s^{-1}]
1	0.387 ± 0.003 (-0.025)	7.51 ± 0.05 (-0.58)	5.55 ± 0.05 (-1.19)
2	0.380 ± 0.008 (-0.027)	6.78 ± 0.03 (+0.79)	6.47 ± 0.09 (+1.13)
3	0.363 ± 0.009 (+0.006)	7.47 ± 0.18 (+0.99)	9.34 ± 0.25 (-0.37)
4	0.331 ± 0.005 (+0.018)	7.41 ± 0.13 (+0.23)	11.09 ± 0.07 (+2.99)
5	0.253 ± 0.007 (+0.021)	7.38 ± 0.05 (+0.86)	10.04 ± 0.26 (+2.87)

4.4.3 Uptake of Gold Nanorods into Vesicles

In section 4.3 (Uptake of Gold Nanospheres into Vesicles), uptake of spherical AuNPs into polymersomes was studied. It was found out that the interactions of AuNPs and polymeric vesicles highly depend on the particle's surface functionalization. More precisely, AuNPs were only able to be taken up into the interior of the vesicle if they were highly negatively charged. For the case of spherical AuNPs, citrate-functionalized particles were chosen. However, nanorods with citrate functionalization are neither commercially nor synthetically available. Due to the procedure of nanorod synthesis, the resulting particles are surrounded by a positively charged CTAB layer, which can then be replaced by surfactants which bind covalently to the gold surface via thiol binding. For this work, a short and negatively charged thiol (MUA) was chosen to replace the CTAB layer on the nanorods. The exchange reaction of CTAB with MUA was described in the previous subsection as well as the particle characterization by TEM, PCS, and UV/Vis.

As a proof of concept, spherical AuNPs were functionalized with MUA and uptake into polymersomes was shown (data not presented). Consequently, one can assume that MUA-functionalized particles act similar as citrate-functionalized particles, and thus the interactions of MUA-functionalized AuNRs with polymersomes were probed. Here, in contrast to section 4.3, where the different interaction scenarios were studied and characterized by PCS, a size- and shape-dependent uptake study was performed using nanorods. In this section, the focus was set on whether nanorods are taken up into vesicles and whether there is limit in aspect ratios for the uptaken nanorods. The experimental results are presented in this subsection.

4.4.3.1 Probing NR-Uptake with PCS

For probing uptake of MUA-functionalized nanorods into polymersomes, only samples 2, 3 and 5 from subsection 4.4.2 were used, because of their different aspect ratios and high monodispersities. Similar to section 4.3, PDMS-*b*-PMOXA polymersomes with a hydrodynamic radius $R_{\mathrm{h,ves}} \approx 135$ nm were used as vesicles. The concentrations of vesicles and nanorods were $c_{\mathrm{ves}} = 1 \times 10^9$ Ves/mL and $c_{\mathrm{NR}} = 2 \times 10^9$ NR/mL, resulting in a ratio of AuNRs to vesicles of $\approx$ 2:1. Polymersomes and AuNRs were mixed by gentle shaking,

and the samples were allowed to stand for ≈ 15 minutes before measuring polarized and depolarized light scattering. In addition, UV/Vis spectroscopy and cryo-TEM of higher concentrated samples were measured.

Figure 4.27a-c shows the polarized (solid symbols) and depolarized scattering intensities (open symbols) of three different mixtures of vesicles and nanorods. For all samples, $R_{\mathrm{VV}}(q)$ of the mixture (red solid squares) is almost equal to the calculated scattering of the sum (dashed line) of vesicles and AuNRs alone. Previously, this indicated no interactions of vesicles and nanoparticles. However, the depolarized scattering intensity $R_{\mathrm{VH}}(q)$ of the mixture (red open squares) is not equal to $R_{\mathrm{VH}}(q)$ of the nanorods alone. Therefore, the size, shape or surrounding of the nanorods needed to have changed upon mixing. The higher the aspect ratio of the nanorod, the stronger the measured $R_{\mathrm{VV}}(q)$ of the mixture deviates from the calculated sum (dashed line). The molar ratio of vesicles and nanorods is 1:2, so the refractive index within the vesicle should increase upon nanorod uptake. For the previous experiments with nanospheres, the uptake of ≈ 2 nanoparticles already lead to a dramatic increase of the scattering intensity by a factor of ≈ 6-7, decoration of vesicles with Au nanospheres even resulted in a 8-9 times higher scattering intensity at q → 0. Consequently, it was assumed that an uptake of nanorods into the interior of the vesicle would also result in a strong increase of scattering intensity. The calculated $R_{\mathrm{VV,mix}}(q \to 0)/R_{\mathrm{VV,ves}}(q \to 0)$ are given in Table 4.14. It can be seen that the ratio is very low, but slightly increases for increasing aspect ratios of the nanorods. In addition, the rate of the intensity decrease becomes less steep from a to c. This indicates a smaller size of the measured species than the pure vesicles. In fact, the radius of gyration (R_{g}) obtained from the slope of the Guinier plot at low q's, reveals a tendency to smaller species at higher aspect ratios (see Table 4.14). The numbers in brackets indicate the difference from the vesicle's R_{g}, and the significant decrease of the vesicular size hypothesizes uptake of nanorods into vesicles. In addition, $R_{\mathrm{VH,mix}}/R_{\mathrm{VH,NR}}$ is not constant over the whole q-range, since $R_{\mathrm{VH,mix}}$ is q-dependent. The values are also given in Table 4.14. Similar to the ratios of the scattering intensities at $q \to 0$, $R_{\mathrm{VH,mix}}/R_{\mathrm{VH,NR}}$ also increases with increasing aspect ratio. This indicates an increase in the overall asymmetry of the system, which is expected for the high aspect ratios of the nanorods.

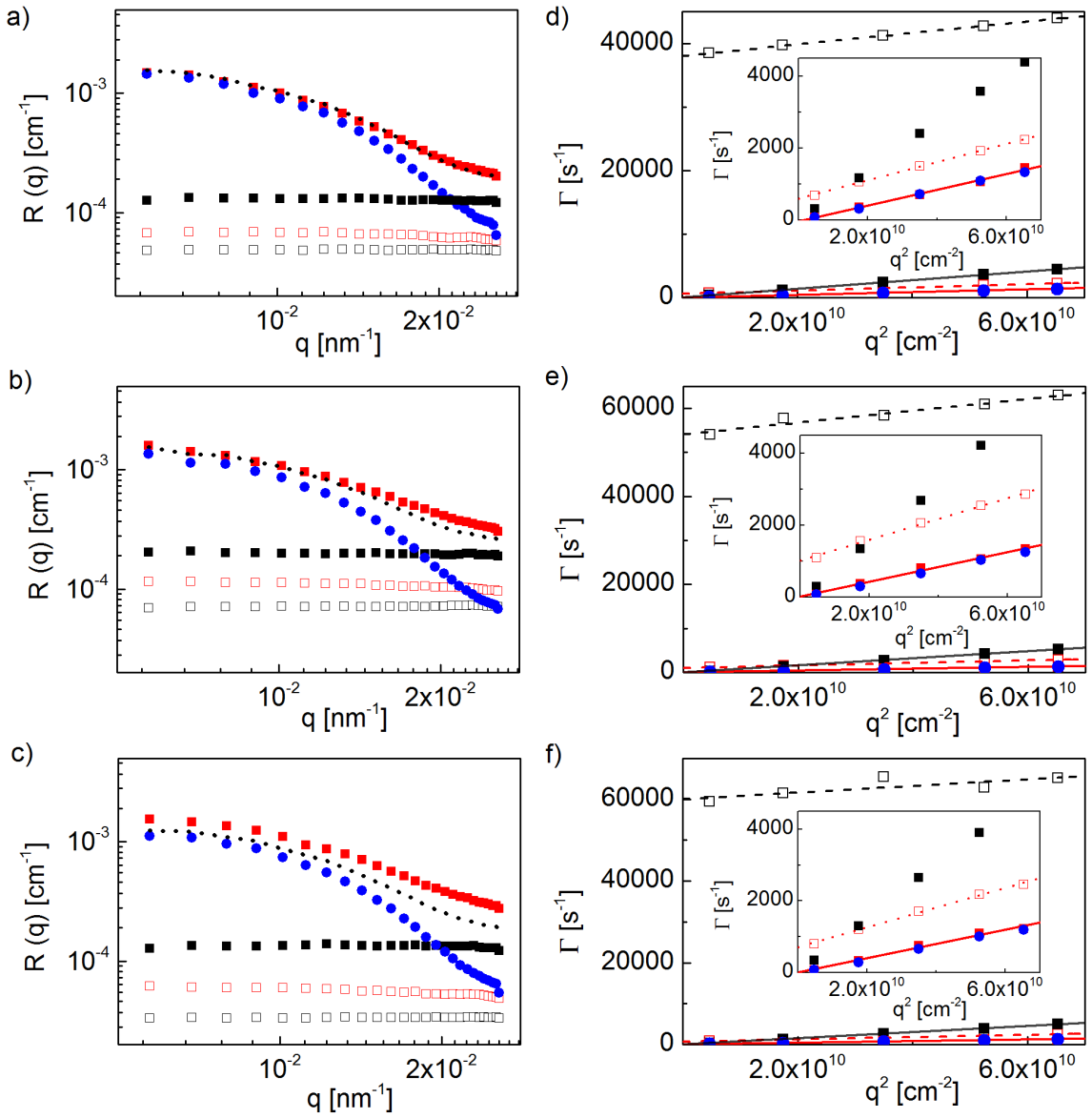

Figure 4.27: *a-c) Time-average absolute Rayleigh ratio for polarized $R_{VV}(q)$ (solid symbols) and depolarized $R_{VH}(q)$ (open symbols) light scattering from a dilute aqueous suspension of PDMS-b-PMOXA vesicles and MUA-functionalized Au nanorods (a) NR 2, b) NR 3, c) NR 5) as a function of the scattering wave vector, q. The data of the mixture is represented by red symbols, data of the vesicles by blue symbol, and data of the NRs by black symbols. The sum of $R_{VV}(q)$ of both vesicles and NRs is represented by the dashed line. d-f) Relaxation rates Γ for slow (VV, solid symbols) and fast (VH, open symbols) components according to the color code in a-c). The inset shows an enlargement of the plot for low Γ.*

Table 4.14: *Comparison of polarized scattering intensities of the mixture and pure vesicles ($R_{VV,mix}(q \to 0)/R_{VV,ves}(q \to 0)$) as recorded in SLS and extrapolated to $q \to 0$. The ratio of the depolarized scattering intensities of the mixture and pure nanorods ($R_{VH,mix}/R_{VH,NR}$) is compared from low to high q's.*

	$\frac{R_{VV,mix}(q \to 0)}{R_{VV,ves}(q \to 0)}$	$\frac{R_{VH,mix}}{R_{VH,NR}}$	R_g (low q) [nm]
Ves + NR 2	1.17	1.40 → 1.21	128 ± 1 (-10)
Ves + NR 3	1.71	1.66 → 1.34	121 ± 2 (-16)
Ves + NR 5	1.77	1.85 → 1.45	118 ± 2 (-20)

Figure 4.27d-f shows the relaxation rates $\Gamma_{VV}(q)$ and $\Gamma_{VH}(q)$ of the systems. For all experiments, $\Gamma_{VV,mix}(q)$ is almost equal to $\Gamma_{VV,ves}(q)$ (see inset), whereas $\Gamma_{VH,mix}(q)$ is far away from $\Gamma_{VH,NR}(q)$. Taking a closer look at the relaxation rates, one can see that there is a difference in the intercepts of $\Gamma_{VH,mix}(q)$ at $q = 0$ for each sample, although all run more or less parallel to the relaxation rates of $\Gamma_{VV,mix}(q)$. Consequently, the correlation rates for both VV and VH of the mixture correspond to the same species. The different relaxation rates of $\Gamma_{VH,mix}(q)$ of the three different samples result in slightly different values for R_r, as summarized in Table 4.15. The values obtained for R_h and R_r, assuming spherical shape of the species, are similar for all samples and are all slightly smaller than for the pure vesicles. A decrease in the size of the vesicles leads to the assumption that nanoparticles were taken up into the interior of the vesicles and thus membrane material was consumed. In addition, a similar size of R_h and R_r reveals that the nanorods need to be attached to the the membrane, since freely diffusing AuNRs would have a much faster rotational diffusion rate. Since the average size of the species is smaller than the size of pure vesicles, the nanorods need to be attached to the inner side of the membrane. Decoration of nanorods at the outer side would result in much larger species, as already observed for interactions of vesicles with nanospheres. Consequently, the AuNRs show similar behavior to spherical AuNPs. However, a small discrepancy between R_h and R_r was observed, while R_r is always smaller than R_h. This can be due to the fact that the internalized nanorods may not be tightly attached to the inner side to the membrane, but

Table 4.15: *Characteristic dimensions of mixtures of vesicles and Au nanorods.*

	R_h [nm]	R_r [nm]	λ_{max} [nm]
Ves + NR 2	119.6 ± 5.5 (-15.4)	109.0 ± 5.1	535 (+24), 815 (+59)
Ves + NR 3	114.5 ± 16.2 (-20.7)	91.1 ± 5.0	536 (+27), 849 (+60)
Ves + NR 5	123.9 ± 11.3 (-14.1)	100.4 ± 6.7	536 (+26), 899 (+51)

are slightly able to rotate along the membrane wall due to their stiff and elongated shape, hence resulting in a faster rotational diffusion coefficient than the whole vesicle-nanorod complex. It has been tried to calculate R_h and R_r assuming aspherical shape (prolate or oblate ellipsoids, or rod-shaped), but no reasonable results were obtained considering both translational and rotational diffusion coefficients.

Figure 4.28 shows the relaxation correlation functions ($C(q,t)$) of the three different samples recorded for polarized (VV, a-c) and depolarized (VH, d-f) scattering. The solid lines represents the theoretical fits of the experimental functions. The relaxation functions of the nanorods (yellow) show the characteristic double decay in polarized scattering, whereas there is only a single decay in depolarized scattering. $C_{VV}(q,t)$ of the vesicles (blue) is always a single exponential decay in VV and zero in VH. As once can see from Figure 4.28a-c, the recorded polarized relaxation functions of the mixtures (red) are always close to those of vesicles alone. However, the functions decay slightly faster, thus resulting in a slightly smaller size of the measured species. Interestingly, $C_{VV}(q,t)$ becomes less steep for the samples with higher aspect ratios, indicating a larger polydispersity or a more pronounced contribution of the depolarized scattering component. The latter might arise from a slightly aspherical shape of the formed species. Figure 4.28d-f reveals the relaxation functions $C_{VH}(q,t)$ of the samples. Clearly, $C_{VH}(q,t)$ of the mixtures are completely different from $C_{VH}(q,t)$ of the nanorods alone. The hydrodynamic and the rotational radii were calculated from the relaxation rates and were already discussed above.

Similar to the previous section on vesicles and nanoparticles (see section 4.3), theoretical simulations of the light scattering profiles of vesicles and nanorods were performed.

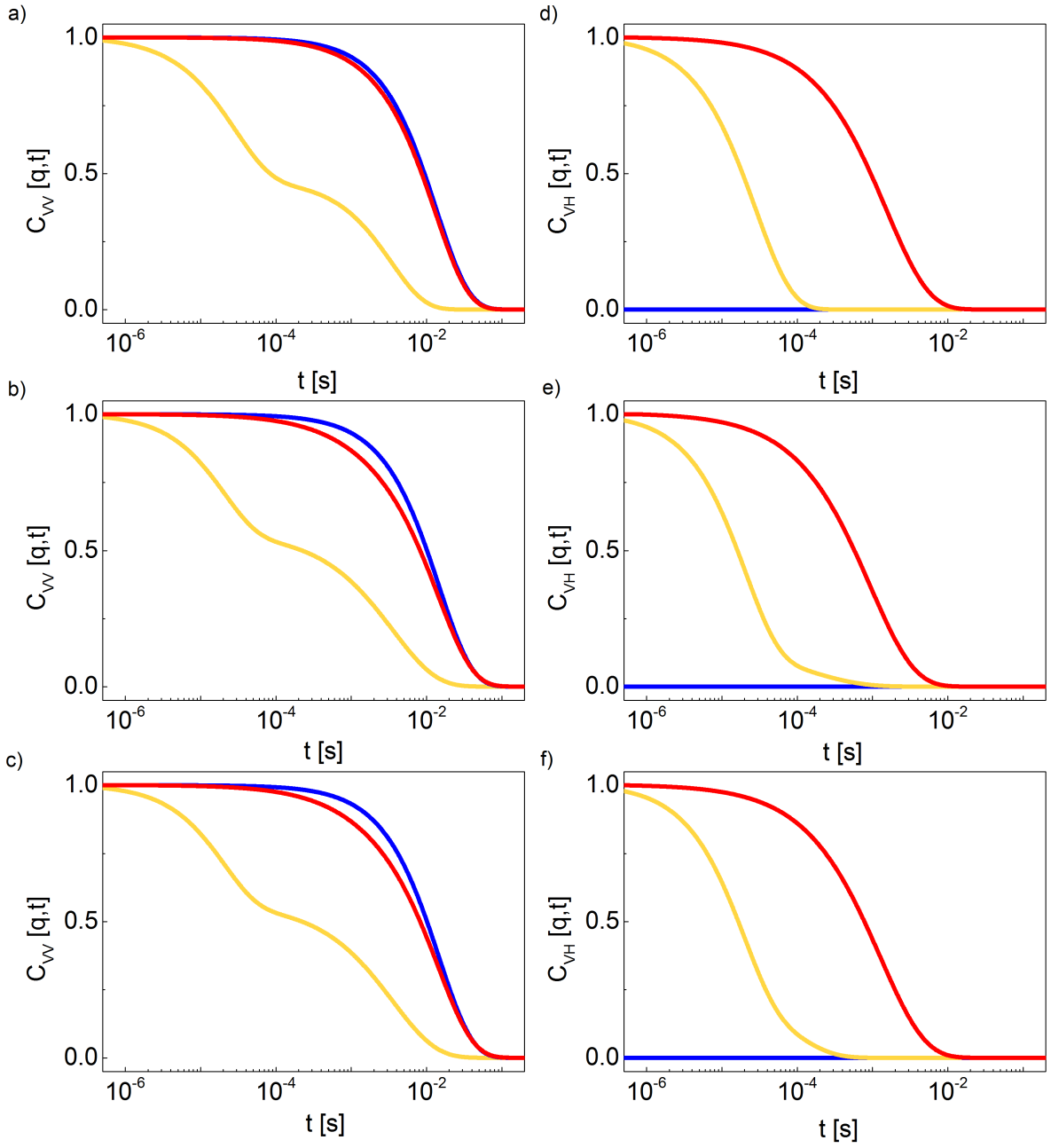

Figure 4.28: *Relaxation functions of the three different systems (a) Ves + NR 2, b) Ves + NR 3, c) Ves + NR 4) at* $q = 6.85 \times 10^{-3}$ nm^{-1}*, recorded for VV and VH polarization, respectively. The solid lines indicate the theoretical representation (see text) of the experimental functions. Mixture: red, vesicles: blue, NP: yellow. The PCS experiment was performed with a coherent laser light at* $\lambda = 632$ nm*, far above* $\lambda_{max,1}$ *and far below* $\lambda_{max,2}$ *of the AuNRs.*

Details are shown in Figure 4.29 a). The results indicate that there is on average only one nanorod per vesicle (red solid line), although the incorporation of two nanorods would still fit the data quite well due to the very low scattering length density of the nanorods alone (red dashed line). This is in very good agreement with the concentration ratio of vesicles and nanorods in the experiment ($\approx$ 2:1). The anisotropy from the polarization data for the mixture of vesicles and nanorods is $\approx 40\%$ and therefore much bigger than that for the case of decoration in the previous section ($\approx 5\%$). The only way to theoretically reproduce this anisotropy is by deforming the vesicles into strong ellipsoids with an aspect ratio of ≈ 4 between the long and the short axes. This could be explained by the propensity of the vesicle to better embrace the shape of the nanorod. However, such strong deformations could not be validated by dynamic light scattering. The experimental results for the two transport coefficients D^{t} and D^{r} do neither allow a prolate nor an oblate shape of the formed species. Furthermore, the images obtained in cryo-TEM do not validate such strong deformations. In addition, assuming two nanorods per vesicle and given the very low scattering length density of the nanorods, their presence influences very little the anisotropy of the system, whatever their orientations. Consequently, no theoretical explanation for the high value of $R_{\mathrm{VH,mix}}/R_{\mathrm{VH,NR}}$ could be found so far.

4.4.3.2 Sensitivity of Nanorods in UV/Vis

The extinction maxima of the samples shown in Table 4.15b) were significantly red-shifted compared to the extinction maxima of the nanorods alone. For the transversal peaks, a shift of $24-27$ nm was observed, whereas the shift of the longitudinal peak was even more pronounced ($51-60$ nm). In the previous section, describing the interactions of gold nanospheres with vesicles, much smaller shifts in the extinction maxima were reported (see Table 4.9 in section 4.3). For example, for uptake of gold nanospheres into the vesicles, a relatively small red-shift of only 8 nm was observed. For all three samples of nanorods in vesicles, the shift of the longitudinal peak is much more pronounced than the shift of the transversal peak. In fact, for plasmonic particles, the wavelength of the shift only depends on the position of the resonance wavelength of the particle, not on its shape or geometry. Larger shifts of the extinction maxima at high wavelengths are due to losses in gold that appear around 500 nm, but are much lower at longer

wavelengths. Consequently, a gold sphere with a diameter of 80 nm, which has a resonance wavelength around 700 nm, is subject to a much larger shift of the extinction maximum than a 20 nm-sized sphere. According to this, the longitudinal resonance wavelength experiences a stronger shift upon change of the refractive index than the transversal resonance wavelength of the same particle. In the case of the nanorods used in this study, the refractive index changes from $n \approx 1.33$ to $n \approx 1.45$, assuming that the nanorod is covered by a polymeric membrane of $d = 16$ nm. Theoretical simulations confirmed a shift of the longitudinal peak by about 40 nm, which is slightly smaller than observed in the experiment. This might be due to an additional increase in the refractive index at one side of the gold nanorods, since the engulfed particles need to be attached to the inner side of the membrane. Consequently, the side of the nanorod attaching to the membrane is covered by two layers of membrane, resulting in a shell thickness of $d = 32$ nm. In addition, the uptaken AuNRs are still covered by a monolayer of MUA molecules, also contributing to a higher shift in the refractive index. Both effects were not considered in the simulations.

4.4.3.3 Cryo-TEM Images of Nanorod Uptake

Cryo-TEM imaging was performed by Max Bernhardt [Ber14] in order to support PCS and UV/Vis results. Figure 4.30 shows images of all three samples. It can be seen that the nanorods are positioned inside of the vesicles and that they are fully wrapped by membrane material. Due to limitations of the method to two dimensions only, one cannot differentiate if the nanorods are attached to the vesicle's membrane or if they are diffusion freely within the vesicle. However, it was shown from PCS, that the nanorods need to be attached to the inner side of the membrane.

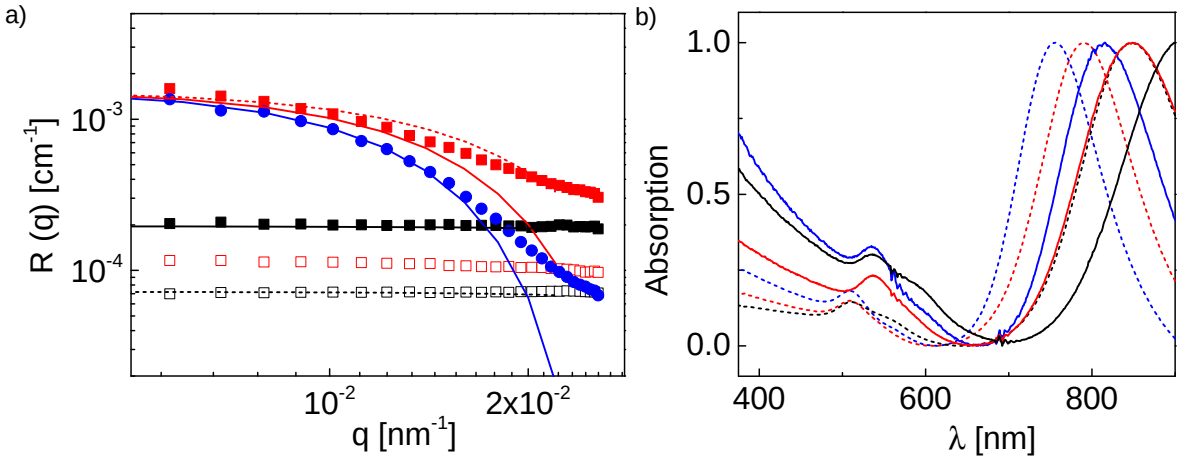

Figure 4.29: *a) Comparison of experimental (symbols) and calculated (lines) scattering profiles for vesicles with NR3 (see Figure 4.27b)). black: nanorods; blue: vesicles; red: mixture. The red solid line represents the calculated scattering profile for one nanorod per vesicle, whereas the red dashed line represents the calculated scattering profile for two nanorods per vesicle. b) Extinction spectra of MUA-functionalized AuNRs (dashed lines) and mixtures of AuNRs and polymersomes (solid lines). Color code: blue: NR-2, red: NR-3, black: NR-5.*

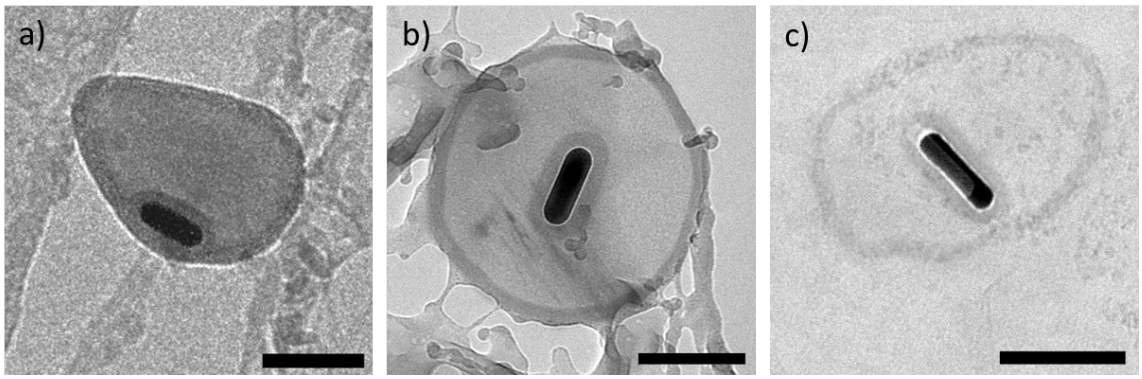

Figure 4.30: *Cryo-TEM images of three different samples of vesicles and nanorods. The AuNRs are fully wrapped by the polymer membrane. a) Ves + NR 2, b) Ves + NR 3, c) Ves + NR 4. The scale bar corresponds to 100* nm.

5. Conclusion and Outlook

In this work, synthesis of PDMS-*b*-PMOXA was performed and subsequent polymersome formation in water was studied. The polymersomes were formed by a film rehydration method and were then homogenized using an extruder with definite membrane size. PCS and cryo-TEM were used to characterize the size, shape and membrane thickness of the formed polymersomes. It was shown that the most monodisperse samples were obtained at a medium extrusion speed at multiple repeating cycles.

Spherical AuNPs were intensively characterized by PCS, TEM, UV/Vis and polarization anisotropy measurements. It was shown that the depolarized light scattering was not zero due to the inevitable internal crystallinity. Interestingly, while the bare Au cores assumed almost a spherical shape, the assigned asphericity occurred upon their soft grafting. For the first time, an experimental report on the asymmetric arrangement of the grafting on spherical cores was given by analyzing the wavelength dependent depolarization ratio for six identical gold cores with different grafting as well as the two transport coefficients obtained from polarized and depolarized DLS. Based on the theoretical representation of the present experimental results, the shell asphericity was parallel to the inherent, due to polycrystallinity, core anisotropy. The presented experimental work opens a new pathway for engineering the shape of metallic NPs driven by their nanocrystallinity. Access to the Au core nanocrystallinity defects is important since many physical properties such as reactivity and mechanical strength are depend on whether the metal NPs are 100% single crystalline or 100% twinned. On the other hand, control of the overall shape of the same spherical NPs by grafting impacts their morphology in polymer nanocomposites.

Interactions of polymersomes and AuNPs were investigated by PCS, cryo-TEM and UV/Vis. Three possible scenarios were considered upon mixing of polymersomes and

AuNPs: (i) *no interactions* between particles and vesicles, (ii) attachment of the particles to the outer side of the vesicle (*decoration*), and (iii) *uptake* of particles into the vesicles. It was found that all three scenarios were possible, solely depending on the particle's surface functionalization. Since the polymersomes were positively charged, no attractive interactions were possible with also positively charged particles due to electrostatic repulsion. Consequently, positively charged AuNPs did not interact with polymersomes in any way. However, attractive interactions were possible when the AuNPs were negatively charged. Slightly negatively charged particles stabilized with PEG interacted with polymersomes, but were not taken up into the interior of the vesicle (decoration). For negatively charged particles without PEG grafts (citrate stabilized), the attractive interaction between particles and polymersomes lead to uptake of particles into polymersomes. All scenarios were distinguished by only measuring SLS and DLS. The findings were supported by cryo-TEM images, UV/Vis measurements and theoretical simulations. In addition, one could obtain an additional information on the uptake process from DLS. The rotational diffusion coefficient measured in depolarized light scattering revealed that the AuNPs needed to be attached to the inner side of the membrane. This crucial information could only be obtained from depolarized DLS, not from any other experimental measurement.

Finally, the shape-dependent uptake of Au nanorods into polymersomes was studied. It was shown that all investigated AuNRs with aspect rations ranging from 3.0 to 4.3 were incorporated into the vesicle's interior. Consequently, no upper limit of the nanorods' aspect ratio for successful uptake could be obtained. Nanorods with even higher aspect ratios were neither commercially nor synthetically available. The uptake of nanorods into polymersomes was documented by PCS, UV/Vis and cryo-TEM experiments. In analogy to the uptake mechanism of Au nanospheres into vesicles, AuNRs also need to stick to the inner side of the membrane, as shown by PCS experiments.

The findings reported in this work are very important for understanding the interactions of nanoparticles with membranes. It was shown that the process of endocytosis can be attributed to physical processes only. Based on the work presented in this thesis, it would be interesting to further investigate the interactions of negatively charged particles

with positively charged vesicles. Instead of differentiating the three extreme cases of *no interactions*, *decoration* and *uptake*, one could take a closer look at the transition from decoration to uptake. Here, a detailed study on the interactions of nanoparticles and vesicles in dependence on the particle's surface charge would be necessary. Ideally, a critical, minimal surface charge of the nanoparticles would be obtained, assuming a constant surface charge of the polymersomes. In addition, one could tune the membrane's surface charge by altering the polymer composition.

The minimal model system of Au nanoparticles and polymeric membranes captivates with its convenience and practicality. At the same time, when transferring the results to biology, it suffers from being over-simplified, ignoring many important biological attributes of a cell. Therefore, it would be interesting to further develop and modify this minimal model by adding biological features, e.g. (trans-)membrane proteins, receptors and ligands, or actin filaments within the interior of the vesicle. This could be achieved by incorporating transmembrane protein into the polymeric membrane, as already demonstrated by the group of Wolfgang Meier [Mei00, Kum07]. Most probably, the membrane properties will change and so will the interactions of nanoparticles with these modified membranes. It would also be interesting to repeat the presented experiments with inhomogeneous membranes. According to theoretical simulations, the endosome would detach from the inner side of the membrane if the membrane consisted of adhesive patches in an otherwise nonadhesive membrane [Smi07].

In addition to studying endocytosis, the system of nanoparticles and vesicles could be used for biomedical applications, such as drug delivery and drug release. Here, either the nanoparticles or the vesicles themselves could be used as drug carriers. Furthermore, the sensitivity of the system in light scattering could be exploited for sensor applications.

6. Zusammenfassung

Im Rahmen dieser Arbeit wurde das Blockcopolymer PDMS-*b*-PMOXA synthetisiert und die anschließende Bildung von Polymersomen in Wasser untersucht. Die Polymersome wurden mittels der Filmrehydrationsmethode gebildet und dann durch Extrusion durch eine Membran homogenisiert. Die Größe, Form und Membrandicke der geformten Polymersome wurde mit Hilfe von PCS und cryo-TEM charakterisiert. Es wurde gezeigt, dass die homogensten Proben bei mittlerer Extrusionsgeschwindigkeit erhalten wurden.

Kugelförmige AuNPs wurden aufwendig mittels PCS, TEM, UV/Vis und Polarisationsanisotropie-Messungen charakterisiert. Es wurde gezeigt, dass die depolarisierte Streuintensität wegen der internen Kristallinität ungleich Null ist. Da die blanken Partikelkerne beinahe absolut sphärisch sind, resultiert die beobachtete Asymmetrie aus der organischen Pfropfung auf der Partikeloberfläche. Zum ersten Mal wurde die asymmetrische Ausrichtung der Propfung auf sonst sphärischen Partikeln experimentell gezeigt. Dies geschah durch Untersuchung des wellenlängenabhängigen Depolarisationsverhältnisses für sechs identische Gold-Kerne mit unterschiedlicher Pfropfung. Ebenso wurden die zwei Transportkoeffizienten untersucht, die durch polarisierte und depolarisierte dynamische Lichtstreuung für alle Proben erhalten wurden. Die theoretischen Simulationen der experimentellen Ergebnisse zeigen, dass die Ausrichtung der gepfropften Bürsten parallel zur Ausrichtung der internen Kristallinität der AuNPs ist. Die gezeigte Arbeit eröffnet eine neue Möglichkeit, die Form metallischer Nanopartikel mit Hilfe ihrer Nanokristallinität zu manipulieren. Zugang zu den Defekten im Kern der AuNPs ist wichtig, da viele physikalischen Eigenschaften, wie zum Beispiel Reaktivität und mechanische Beanspruchbarkeit, davon abhängig sind, ob der metallische Partikel vollständig monokristallin oder verzwill-

ingt ist. Zudem beeinflusst die Kontrolle über die Form eines eigentlich sphärischen Partikels mittels Pfropfung deren Morphologie in Polymer-Nano-Verbundstrukturen.

Wechselwirkungen zwischen Polymersomen und AuNPs wurden mittels PCS, cryo-TEM und UV/Vis untersucht. Drei mögliche Szenarien beim Mischen von Partikeln und Vesikeln wurden in Erwägung gezogen: (i) *keine Wechselwirkungen*, (ii) Anhaftung der Partikel an die äußere Seite der Vesikel (*Dekoration*), und (iii) *Aufnahme* der Partikel in das Vesikel. Wie herausgefunden wurde, sind alle drei Szenarien möglich und können allein durch die Oberflächenfunktionalisierung der Partikel gesteuert werden. Da die Polymersome positiv geladen waren, war keine attraktive Wechselwirkung des Polymersoms mit positiv geladenen Partikeln wegen elektrostatischer Abstoßung möglich. Daher wechselwirkten positiv geladene AuNPs in keinster Weise mit Polymersomen. Attraktive Wechselwirkungen waren jedoch für leicht negativ geladene Partikel möglich. AuNPs, die mit PEG oberflächenmodifiziert wurden und daher leicht negativ geladen waren, wechselwirkten mit den Polymersomen, wurden jedoch nicht in das Innere der Vesikel aufgenommen (Dekoration). Für negativ geladene Partikel ohne PEG-Funktionalisierung (Stabilisierung durch Citrat) war die Wechselwirkung mit Polymersomen stärker und Aufnahme wurde beobachtet. Alle Szenarien wurden allein durch SLS- und DLS-Messungen unterschieden. Die Ergebnisse wurden durch Bilder in cryo-TEM, durch UV/Vis-Messungen und durch theoretische Simulationen unterstützt und bestätigt. Zusätzlich konnte allein durch Messung der depolarisierten DLS eine weitere Information über den Aufnahme-Prozess gewinnen können: Der Rotationsdiffusionskoeffizient zeigte, dass die AuNPs an der Innenseite der Membran angeheftet sein müssen. Dies ist eine Information, die aus sonst keiner anderen Messung erhalten werden konnte.

Abschließend wurde die Formabhängigkeit der Aufnahme von Gold-Nanostäbchen in Polymersome untersucht. Es wurde gezeigt, dass alle untersuchten Nanostäbchen mit steigenden Aspektverhältnissen von 3,0 bis 4,3 in das Vesikelinnere aufgenommen wurden. Daraus folgt, dass keine obere Grenze des Aspektverhältnisses für erfolgreiche Aufnahme erhalten werden konnte. Gold-Nanostäbchen mit noch größerem Aspektverhältnis konnten leider weder kommerziell noch synthetisch erhalten werden. Die Aufnahme der Stäbchen wurde mittels PCS, cryo-TEM und UV/Vis belegt. Es wurde mittels PCS

gezeigt, dass die Stäbchen, analog zu der Aufnahme von kugelförmigen Nanopartikeln, an der Innenseite der Vesikelmembran angeheftet sein müssen.

Die hier berichteten Ergebnisse tragen essentiell zum Verständnis der Wechselwirkungen zwischen Nanopartikeln und Membranen bei. Es konnte gezeigt werden, dass der Prozess der Endozytose lediglich auf physikalische Prozesse zurück zu führen ist. Basierend auf der hier vorgelegten Arbeit wäre eine weitergehende Untersuchung der Wechselwirkung zwischen negativ geladenen Partikeln und positiv geladenen Vesikeln interessant. Anstatt die drei extremen Szenarien *keine Wechselwirkungen*, *Dekoration* und *Aufnahme* zu unterscheiden, könnte der Übergang von Dekoration zu Aufnahme genauer untersucht werden. Hierzu wäre eine detaillierte Studie zu den Wechselwirkungen zwischen Nanopartikel und Vesikel in Abhängigkeit von der Oberflächenladung des Partikels nötig. Idealerweise könnte somit eine kritische Oberflächenladung des Partikels identifiziert werden, bei der Aufnahme gerade eben stattfinden kann. Dies müsste bei konstanter Oberflächenladung der Polymersome geschehen. Zusätzlich könnte die Ladung der Membran durch Modifizierung des Polymers geändert werden.

Das Minimalmodell bestehend aus Gold-Nanopartikeln und Polymermembran besticht durch seine Einfachheit und Zweckmäßigkeit. Gleichzeitig leidet es unter der zu starken Vereinfachung des komplexen biologischen Hintergrunds. Deshalb wäre eine biologische Modifizierung des Minimalsystems hin zu einer biologischen Zelle interessant, z.B. durch Hinzufügen von Membranproteinen, Rezeptoren und Liganden oder eines Actin-Netzwerks im Inneren des Vesikels. Eine Möglichkeit der biologischen Modifizierung der Membran ist das Einfügen von Transmembranproteinen in die Polymermembran, wie bereits erfolgreich von der Gruppe um Wolfgang Meier beschrieben [Mei00, Kum07]. Höchstwahrscheinlich würden die Membranproteine die Eigenschaften der Membran und dadurch auch deren Wechselwirkung mit Nanopartikeln verändern. Es wäre zudem interessant, die hier vorgestellten Experimente mit inhomogenen Membranen zu wiederholen. Gemäß theoretischen Simulationen würde das Endosom von der Innenseite der Membran losgelöst werden, würde die Membran aus adhäsiven Bereichen in einer ansonsten nicht-adhäsiven Membran bestehen [Smi07].

Zusätzlich zur Untersuchung von Endozytose könnte das Minimalmodell für biomedizinische Anwendung, wie z.B. gezielte Pharmakotherapie, herangezogen werden. Dazu könnten sowohl die Nanopartikel wie auch die Vesikel selbst als Medikamententransporter benutzt werden. Außerdem könnte die Sensitivität des Systems in der Lichtstreuung für Sensorikanwendungen ausgenutzt werden.

Bibliography

[Aas98] J. Aaseth, M. Haugen and O. Forre: *Rheumatoid arthritis and metal compounds-perspectives on the role of oxygen radical detoxification*, The Analyst **123**, 3 (1998).

[Ada08] D. J. Adams, S. Adams, D. Atkins, M. F. Butler and S. Furzeland: *Impact of mechanism of formation on encapsulation in block copolymer vesicles*, Journal of Controlled Release **128**, 165 (2008).

[AE01] H. Aranda-Espinoza, H. Bermudez, F. Bates and D. Discher: *Electromechanical Limits of Polymersomes*, Physical Review Letters **87** (2001).

[Akc09] P. Akcora, H. Liu, S. K. Kumar, J. Moll, Y. Li, B. C. Benicewicz, L. S. Schadler, D. Acehan, A. Z. Panagiotopoulos, V. Pryamitsyn and et al.: *Anisotropic self-assembly of spherical polymer-grafted nanoparticles*, Nature Materials **8**, 354 (2009).

[Alb02] B. Alberts, A. Johnson, J. Lewis, M. Raff, K. Roberts and P. Walter: *Molecular Biology of the Cell, Fourth Edition*, Garland Science, 2002.

[Ara76] S. R. Aragón and R. Pecora: *Theory of dynamic light scattering from polydisperse systems*, The Journal of Chemical Physics **64**, 2395 (1976).

[Ban93] A. Bangham: *Liposomes: the Babraham connection*, Chemistry and Physics of Lipids **64**, 275 (1993).

[Ban07] S. K. Banerji and M. A. Hayes: *Examination of nonendocytotic bulk transport of nanoparticles across phospholipid membranes*, Langmuir **23**, 3305 (2007).

[Bat97] R. P. Batycky, J. Hanes, R. Langer and D. A. Edwards: *A theoretical model of erosion and macromolecular drug release from biodegrading microspheres*, J. Pharm. Sci. **86**, 1464 (1997).

[Ber96] A. T. Bernardes: *Monte Carlo Simulation of Vesicle Self-Organisation*, J. Phys. II France **6**, 169 (1996).

[Ber00] B. J. Berne and R. Pecora: *Dynamic Light Scattering: With Applications to Chemistry, Biology, and Physics*, Dover Publ., Mineola, NY, 2000.

[Ber02] H. Bermudez, A. K. Brannan, D. A. Hammer, F. S. Bates and D. E. Discher: *Molecular weight dependence of polymersome membrane structure, elasticity, and stability*, Macromolecules **35**, 8203 (2002).

[Ber05] S. Berciaud, L. Cognet, P. Tamarat and B. Lounis: *Observation of Intrinsic Size Effects in the Optical Response of Individual Gold Nanoparticles*, Nano Lett. **5**, 515 (2005).

[Ber14] M. Bernhardt: *Mikroskopische Analyse des transmembranen Transports von Nanopartikeln in Polymersome, riesige unilamellare Vesikel und Erythrozyten*, Ph.D. thesis, Johannes Gutenberg Universität (2014).

[Boh98] C. F. Bohren and D. R. Huffman: *Absorption and Scattering of Light by Small Particles*, Wiley-VCH Verlag GmbH, 1998.

[Boz13] B. Bozorgui, D. Meng, S. K. Kumar, C. Chakravarty and A. Cacciuto: *Fluctuation-Driven Anisotropic Assembly in Nanoscale Systems*, Nano Lett. **13**, 2732 (2013).

[Bro93] W. Brown: *Dynamic Light Scattering: The Method and Some Applications*, Clarendon Press, 1993.

[Cal07] N. Calander, I. Gryczynski and Z. Gryczynski: *Interference of surface plasmon resonances causes enhanced depolarized light scattering from metal nanoparticles*, Chemical Physics Letters **434**, 326 (2007).

[Can08] H. Cang, D. Montiel, C. S. Xu and H. Yang: *Observation of spectral anisotropy of gold nanoparticles*, The Journal of Chemical Physics **129**, 044503 (2008).

[Cha05] D. Chandler: *Interfaces and the driving force of hydrophobic assembly*, Nature **437**, 640 (2005).

[Che99] L. Chen, H. Shen and A. Eisenberg: *Kinetics and Mechanism of the Rod-to-Vesicle Transition of Block Copolymer Aggregates in Dilute Solution*, The Journal of Physical Chemistry B **103**, 9488 (1999).

[Che03] S. Chen, Z. L. Wang, J. Ballato, S. H. Foulger and D. L. Carroll: *Monopod, Bipod, Tripod, and Tetrapod Gold Nanocrystals*, Journal of the American Chemical Society **125**, 16186 (2003).

[Che05] J. Chen, B. Wiley, Z.-Y. Li, D. Campbell, F. Saeki, H. Cang, L. Au, J. Lee, X. Li and Y. Xia: *Gold Nanocages: Engineering Their Structure for Biomedical Applications*, Advanced Materials **17**, 2255 (2005).

[Che12] X. Chen, Y. Chen, M. Yan and M. Qiu: *Nanosecond Photothermal Effects in Plasmonic Nanostructures*, ACS Nano **6**, 2550 (2012).

[Chu07] B. Chu: *Laser Light Scattering: Basic Principles and Practice*, Dover Books on Physics, 2007.

[Coo00] G. M. Cooper and R. E. Hausman: *The Cell*, Sinauer Associates Inc., 2000.

[Cur89] H. Curtis and N. S. Barnes: *Biology*, W. H. Freeman, 1989.

[Das13] S. Dasgupta, T. Auth and G. Gompper: *Wrapping of ellipsoidal nano-particles by fluid membranes*, Soft Matter **9**, 5473 (2013).

[Das14] S. Dasgupta, T. Auth and G. Gompper: *Shape and Orientation Matter for the Cellular Uptake of Nonspherical Particles*, Nano Lett. **14**, 687 (2014).

[Deg94] V. Degiorgio, R. Piazza, T. Bellini and M. Visca: *Static and Dynamic Light-Scattering Study of Fluorinated Polymer Colloids with a Crystalline Internal Structure*, Advances in Colloid and Interface Science **48**, 61 (1994).

[Der93] B. Derjaguin and L. Landau: *Theory of the stability of strongly charged lyophobic sols and of the adhesion of strongly charged particles in solutions of electrolytes*, Progress in Surface Science **43**, 30 (1993).

[Des02] M. Deserno and W. M. Gelbart: *Adhesion and wrapping in colloid-vesicle complexes*, Journal of Physical Chemistry B **106**, 5543 (2002).

[Des03] M. Deserno and T. Bickel: *Wrapping of a spherical colloid by a fluid membrane*, Europhysics Letters **62**, 767 (2003).

[Des04] M. Deserno: *Elastic deformation of a fluid membrane upon colloid binding*, Physical Review E **69** (2004).

[Die97] C. Dietrich, M. Angelova and B. Pouligny: *Adhesion of Latex Spheres to Giant Phospholipid Vesicles: Statics and Dynamics*, J. Phys. II France **7**, 1651 (1997).

[Dis99] B. M. Discher, Y. Y. Won, D. S. Ege, J. C. M. Lee, F. S. Bates, D. E. Discher and D. A. Hammer: *Polymersomes: Tough vesicles made from diblock copolymers*, Science **284**, 1143 (1999).

[Dis02] D. E. Discher and A. Eisenberg: *Polymer vesicles*, Science **297**, 967 (2002).

[Dis06] D. E. Discher and F. Ahmed: *Polymersomes*, Annual Review of Biomedical Engineering **8**, 323 (2006).

[Doh09] G. J. Doherty and H. T. McMahon: *Mechanisms of Endocytosis*, Annual Review of Biochemistry **78**, 857 (2009).

[Dör02] H.-D. Dörfler: *Grenzflächen und kolloid-disperse Systeme: Physik und Chemie*, Springer-Verlag, 2002.

[DS07] N. Dos Santos, C. Allen, A.-M. Doppen, M. Anantha, K. A. Cox, R. C. Gallagher, G. Karlsson, K. Edwards, G. Kenner, L. Samuels and et al.: *Influence of poly(ethylene glycol) grafting density and polymer length on liposomes: Relating plasma circulation lifetimes to protein binding*, Biochimica et Biophysica Acta (BBA) - Biomembranes **1768**, 1367 (2007).

[Du04] J. Du and Y. Chen: *Preparation of Organic/Inorganic Hybrid Hollow Particles Based on Gelation of Polymer Vesicles*, Macromolecules **37**, 5710 (2004).

[Egl11] S. Egli, M. G. Nussbaumer, V. Balasubramanian, M. Chami, N. Bruns, C. Palivan and W. Meier: *Biocompatible Functionalization of Polymersome Surfaces: A New Approach to Surface Immobilization and Cell Targeting Using Polymersomes*, Journal of the American Chemical Society **133**, 4476 (2011).

[Ein05] A. Einstein: *Über die von der molekularkinetischen Theorie der Wärme geforderte Bewegung von in ruhenden Flüssigkeiten suspendierten Teilchen*, Annalen der Physik **322**, 549 (1905).

[Elw66] P. H. Elworthy and K. J. Mysels: *The surface tension of sodium dodecylsulfate solutions and the phase separation model of micelle formation*, Journal of Colloid and Interface Science **21**, 331 (1966).

[ES05] I. H. El-Sayed, X. Huang and M. A. El-Sayed: *Surface Plasmon Resonance Scattering and Absorption of anti-EGFR Antibody Conjugated Gold Nanoparticles in Cancer Diagnostics: Applications in Oral Cancer*, Nano Letters **5**, 829 (2005).

[Esq02] C. Esquenet and E. Buhler: *Aggregation Behavior in Semidilute Rigid and Semirigid Polysaccharide Solutions*, Macromolecules **35**, 3708 (2002).

[Fer03] A. Fery, S. Moya, P.-H. Puech, F. Brochard-Wyart and H. Mohwald: *Interaction of polyelectrolyte coated beads with phospholipid vesicles*, Comptes Rendus Physique **4**, 259 (2003).

[Fle10] M. Fleischer, D. Zhang, K. Braun, S. Jäger, R. Ehlich, M. Häkkinen, Häffner, C. Stanciu, J. K. H. Hörber, A. J. Meixner and D. P. Kern: *Tailoring gold nanostructures for near-field optical applications*, Nanotechnology **21**, 065301 (2010).

[For06] M. J. Ford, C. Masens and M. B. Cortie: *The application of gold surfaces and particles in nanotechnology*, Surface Review and Letters **13**, 297 (2006).

[Fra84] E. N. Frankel: *Lipid oxidation: Mechanisms, products and biological significance*, Journal of the American Oil Chemists' Society **61**, 1908 (1984).

[Fre73] G. Frens: *Controlled Nucleation for the Regulation of the Particle Size in Monodisperse Gold Suspensions*, Nature Physical Science **241**, 20 (1973).

[Gei05] M. Geiser, B. Rothen-Rutishauser, N. Kapp, S. Schurch, W. Kreyling, H. Schulz, M. Semmler, V. I. Hof, J. Heyder and P. Gehr: *Ultrafine particles cross cellular membranes by nonphagocytic mechanisms in lungs and in cultured cells*, Environmental Health Perspectives **113**, 1555 (2005).

[Gli12] M. Glidden and M. Muschol: *Characterizing Gold Nanorods in Solution Using Depolarized Dynamic Light Scattering*, The Journal of Physical Chemistry C **116**, 8128 (2012).

[Gri89] M. Grit, J. De Schmidt, A. Struijke and D. Crommelin: *Hydrolysis of phosphatidylcholine in aqueous liposome dispersions*, International Journal of Pharmaceutics **50**, 1, cited By (since 1996)53 (1989).

[Gri93] M. Grit and D. J. Crommelin: *Chemical stability of liposomes: implications for their physical stability*, Chemistry and Physics of Lipids **64**, 3 (1993).

[Had02] N. Hadjichristidis, S. Pispas and G. A. Floudas: *Block Copolymers: Synthetic Strategies, Physical Properties, and Applications*, John Wiley & Sons, 2002.

[Hae02] A. J. Haes and R. P. Van Duyne: *A Nanoscale Optical Biosensor: Sensitivity and Selectivity of an Approach Based on the Localized Surface Plasmon Resonance Spectroscopy of Triangular Silver Nanoparticles*, Journal of the American Chemical Society **124**, 10596 (2002).

[Hag13] M. Haghighi, M. A. Plum, G. Gantzounis, H.-J. Butt, W. Steffen and G. Fytas: *Plasmon-Enhanced Dynamic Depolarized Light Scattering*, The Journal of Physical Chemistry C **117**, 8411 (2013).

[Hal91] F. Hallett, J. Watton and P. Krygsman: *Vesicle sizing*, Biophysical Journal **59**, 35 (1991).

[Han07] M. Hanauer, S. Pierrat, I. Zins, A. Lotz and C. Sönnichsen: *Separation of Nanoparticles by Gel Electrophoresis According to Size and Shape*, Nano Lett. **7**, 2881 (2007).

[Häk12] H. Häkkinen: *The gold-sulfur interface at the nanoscale*, Nature Chemistry **4**, 443 (2012).

[Hor51] P. Horn, H. Benoit and G. Oster: *Etude de la lumiere diffusee par des solutions tres diluees de batonnets optiquement anisotropes*, Journal de chimie physique et de physicochimie biologique **48**, 530 (1951).

[Hor55] P. Horn: *Contributions to the study of the scattering of light by solutions of anisotropic macromolecules*, Annales de Physique **10**, 386 (1955).

[Hua07] W. Huang, W. Qian, M. El-Sayed, Y. Ding and Z. Wang: *Effect of the Lattice Crystallinity on the Electron-Phonon Relaxation Rates in Gold Nanoparticles*, Journal of Physical Chemistry C **111**, 10751 (2007).

[Hun81] R. J. Hunter: *Zeta potential in colloid science: principles and applications*, Academic Press, 1981.

[Ima01] S.-i. Imabayashi, D. Hobara and T. Kakiuchi: *Voltammetric Detection of the Surface Diffusion of Adsorbed Thiolate Molecules in Artificially Phase-Separated Binary Self-Assembled Monolayers on a Au(111) Surface*, Langmuir **17**, 2560 (2001).

[Ion08] P. Ionita, A. Volkov, G. Jeschke and V. Chechik: *Lateral Diffusion of Thiol Ligands on the Surface of Au Nanoparticles: An Electron Paramagnetic Resonance Study*, Analytical Chemistry **80**, 95 (2008).

[Isr76] J. N. Israelachvili, D. J. Mitchell and B. W. Ninham: *Theory of self-assembly of hydrocarbon amphiphiles into micelles and bilayers*, J. Chem. Soc., Faraday Trans. 2 **72**, 1525 (1976).

[Jas12a] K. Jaskiewicz: *Transport of nanoparticles into polymersomes : a minimal model system of particles passage through biological membranes*, Ph.D. thesis, Johannes Gutenberg Universität (2012).

[Jas12b] K. Jaskiewicz, A. Larsen, I. Lieberwirth, K. Koynov, W. Meier, G. Fytas, A. Kroeger and K. Landfester: *Probing bioinspired transport of nanoparticles into polymersomes*, Angew Chem Int Ed Engl **51**, 4613 (2012).

[Jas12c] K. Jaskiewicz, A. Larsen, D. Schaeffel, K. Koynov, I. Lieberwirth, G. Fytas, K. Landfester and A. Kroeger: *Incorporation of Nanoparticles into Polymersomes: Size and Concentration Effects*, Acs Nano **6**, 7254 (2012).

[Jas12d] K. Jaskiewicz, M. Makowski, M. Kappl, K. Landfester and A. Kroeger: *Mechanical Properties of Poly(dimethylsiloxane)-block-poly(2-methyloxazoline) Polymersomes Probed by Atomic Force Microscopy*, Langmuir **28**, 12629 (2012).

[Jia08] W. Jiang, B. Y. S. Kim, J. T. Rutka and W. C. W. Chan: *Nanoparticle-mediated cellular response is size-dependent*, Nature Nanotechnology **3**, 145 (2008).

[Joh72] P. B. Johnson and R. W. Christy: *Optical Constants of the Noble Metals*, Phys. Rev. B **6**, 4370 (1972).

[Jua11] M. L. Juan, M. Righini and R. Quidant: *Plasmon nano-optical tweezers*, Nature Photon **5**, 349 (2011).

[Kam84] R. F. Kamrath and E. I. Franses: *Mass-action model of mixed micellization*, The Journal of Physical Chemistry **88**, 1642 (1984).

[Kel03] K. L. Kelly, E. Coronado, L. L. Zhao and G. C. Schatz: *The Optical Properties of Metal Nanoparticles: The Influence of Size, Shape, and Dielectric Environment*, The Journal of Physical Chemistry B **107**, 668 (2003).

[Kem88] J. Kemps and D. Crommelin: *Chemical stability of phospholipids in pharmaceutical preparations. II. Peroxidation of phospholipids in aqueous solutions*, Pharmaceutisch Weekblad **123**, 457 (1988).

[Ken81] C. R. Kensil and E. A. Dennis: *Alkaline hydrolysis of phospholipids in model membranes and the dependence on their state of aggregation*, Biochemistry **20**, 6079 (1981).

[Khl08] N. G. Khlebtsov: *Determination of size and concentration of gold nanoparticles from extinction spectra*, Analytical Chemistry **80**, 6620 (2008).

[Koc14] A. H. R. Koch, G. Lévêque, S. Harms, K. Jaskiewicz, M. Bernhardt, A. Henkel, C. Sönnichsen, K. Landfester and G. Fytas: *Surface Asymmetry of Coated Spherical Nanoparticles*, Nano Lett. **14**, 4138 (2014).

[Koe03] G. H. Koenderink, H. Zhang, D. G. A. L. Aarts, M. P. Lettinga, A. P. Philipse and G. Nagele: *On the validity of Stokes-Einstein-Debye relations for rotational diffusion in colloidal suspensions*, Faraday Discussions **123**, 335 (2003).

[Kol99] I. Koltover, J. Rädler and C. Safinya: *Membrane Mediated Attraction and Ordered Aggregation of Colloidal Particles Bound to Giant Phospholipid Vesicles*, Physical Review Letters **82**, 1991 (1999).

[Kos99] K. Kostarelos, T. F. Tadros and P. F. Luckham: *Physical Conjugation of (Tri-) Block Copolymers to Liposomes toward the Construction of Sterically Stabilized Vesicle Systems*, Langmuir **15**, 369 (1999).

[Kum07] M. Kumar, M. Grzelakowski, J. Zilles, M. Clark and W. Meier: *Highly permeable polymeric membranes based on the incorporation of the functional water channel protein Aquaporin Z*, Proceedings of the National Academy of Sciences of the United States of America **104**, 20719 (2007).

[Lan10] J. M. D. Lane and G. S. Grest: *Spontaneous Asymmetry of Coated Spherical Nanoparticles in Solution and at Liquid-Vapor Interfaces*, Physical Review Letters **104** (2010).

[Las94] D. D. Lasic: *Sterically Stabilized Vesicles*, Angewandte Chemie International Edition in English **33**, 1685 (1994).

[LB09] O. Le Bihan, P. Bonnafous, L. Marak, T. Bickel, S. Trepout, S. Mornet, F. De Haas, H. Talbot, J. C. Taveau and O. Lambert: *Cryo-electron tomography of nanoparticle transmigration into liposome*, Journal of Structural Biology **168**, 419 (2009).

[Lee02] J. C.-M. Lee, M. Santore, F. S. Bates and D. E. Discher: *From Membranes to Melts, Rouse to Reptation: Diffusion in Polymersome versus Lipid Bilayers*, Macromolecules **35**, 323 (2002).

[Lei80] L. Leibler: *Theory of Microphase Separation in Block Copolymers*, Macromolecules **13**, 1602 (1980).

[Len02] J. Leng, S. U. Egelhaaf and M. E. Cates: *Kinetic pathway of spontaneous vesicle formation*, Europhysics Letters (EPL) **59**, 311 (2002).

[Len03] J. Leng, S. Egelhaaf and M. Cates: *Kinetics of the Micelle-to-Vesicle Transition: Aqueous Lecithin-Bile Salt Mixtures*, Biophysical Journal **85**, 1624 (2003).

[Lew08] N. Lewinski, V. Colvin and R. Drezek: *Cytotoxicity of Nanoparticles*, Small **4**, 26 (2008).

[Lin99] S. Link and M. A. El-Sayed: *Size and temperature dependence of the plasmon absorption of colloidal gold nanoparticles*, Journal of Physical Chemistry B **103**, 4212 (1999).

[Lin10] D. Lingwood and K. Simons: *Lipid Rafts As a Membrane-Organizing Principle*, Science **327**, 46 (2010).

[Liu10] C.-J. Liu, C.-H. Wang, S.-T. Chen, H.-H. Chen, W.-H. Leng, C.-C. Chien, C.-L. Wang, I. M. Kempson, Y. Hwu, T.-C. Lai and et al.: *Enhancement of cell radiation sensitivity by pegylated gold nanoparticles*, Phys. Med. Biol. **55**, 931 (2010).

[LM11] J. F. Le Meins, O. Sandre and S. Lecommandoux: *Recent trends in the tuning of polymersomes' membrane properties*, The European Physical Journal E **34** (2011).

[Lod00] H. Lodish, A. Berk and P. Matsudaira: *Molecular Cell Biology*, W. H. Freeman, 2000.

[Log80] M. K. Logani and R. E. Davies: *Lipid oxidation: Biologic effects and antioxidants-A review*, Lipids **15**, 485 (1980).

[LR05] C. Le Roy and J. L. Wrana: *Clathrin- and non-clathrin-mediated endocytic regulation of cell signalling*, Nat Rev Mol Cell Biol **6**, 112 (2005).

[Luo01] L. Luo and A. Eisenberg: *Thermodynamic Size Control of Block Copolymer Vesicles in Solution*, Langmuir **17**, 6804 (2001).

[Mad09] M. M. Mady, M. M. Darwish, S. Khalil and W. M. Khalil: *Biophysical studies on chitosan-coated liposomes*, European Biophysics Journal **38**, 1127 (2009).

[Mar98] O. Martin and N. Piller: *Electromagnetic scattering in polarizable backgrounds*, Phys. Rev. E **58**, 3909 (1998).

[Mar03] S. J. Marrink and A. E. Mark: *Molecular Dynamics Simulation of the Formation, Structure, and Dynamics of Small Phospholipid Vesicles*, Journal of the American Chemical Society **125**, 15233 (2003).

[Mat95] H. Matsumura, K.-i. Watanabe and K. Furusawa: *Flocculation behavior of egg phosphatidylcholine liposomes caused by Ca2+ ions*, Colloids and Surfaces A: Physicochemical and Engineering Aspects **98**, 175 (1995).

[McM11] H. T. McMahon and E. Boucrot: *Molecular mechanism and physiological functions of clathrin-mediated endocytosis*, Nat Rev Mol Cell Biol **12**, 517 (2011).

[McN97] A. D. McNaught and A. Wilkinson: *IUPAC Compendium of Chemical Terminology. 2nd ed. (the "Gold Book")*, Blackwell Scienteific Publications, 1997.

[Mei00] W. Meier, C. Nardin and M. Winterhalter: *Reconstitution of channel proteins in (polymerized) ABA triblock copolymer membranes*, Angewandte Chemie-International Edition **39**, 4599 (2000).

[Mic13] R. Michel, T. Plostica, L. Abezgauz, D. Danino and M. Gradzielski: *Control of the stability and structure of liposomes by means of nanoparticles*, Soft Matter **9**, 4167 (2013).

[Mor03] K. Morigaki, H. Schönherr, C. W. Frank and W. Knoll: *Photolithographic Polymerization of Diacetylene-Containing Phospholipid Bilayers Studied by Multimode Atomic Force Microscopy*, Langmuir **19**, 6994 (2003).

[Muk97] S. Mukherjee, R. N. Ghosh and F. R. Maxfield: *Endocytosis.*, Physiol Rev **77**, 759 (1997).

[Mur05] C. J. Murphy, T. K. Sau, A. M. Gole, C. J. Orendorff, J. Gao, L. Gou, S. E. Hunyadi and T. Li: *Anisotropic Metal Nanoparticles: Synthesis, Assembly, and Optical Applications*, The Journal of Physical Chemistry B **109**, 13857 (2005).

[Nap01] A. Napoli, N. Tirelli, G. Kilcher and A. Hubbell: *New Synthetic Methodologies for Amphiphilic Multiblock Copolymers of Ethylene Glycol and Propylene Sulfide*, Macromolecules **34**, 8913 (2001).

[Nar00] C. Nardin, T. Hirt, J. Leukel and W. Meier: *Polymerized ABA triblock copolymer vesicles*, Langmuir **16**, 1035 (2000).

[Nog01] H. Noguchi and M. Takasu: *Self-assembly of amphiphiles into vesicles: A Brownian dynamics simulation*, Phys. Rev. E **64**, 041913 (2001).

[Odi04] G. Odian: *Principles of Polymerization*, Wiley-Interscience, 2004.

[Ort03] A. Ortega and J. Garcia de la Torre: *Hydrodynamic properties of rodlike and disklike particles in dilute solution*, The Journal of Chemical Physics **119**, 9914 (2003).

[Pay06] E. K. Payne, K. L. Shuford, S. Park, G. C. Schatz and C. A. Mirkin: *Multipole Plasmon Resonances in Gold Nanorods*, The Journal of Physical Chemistry B **110**, 2150 (2006).

[Per36] F. Perrin: *Mouvement Brownien d'un ellipsoide (II). Rotation libre et dépolarisation des fluorescences. Translation et diffusion de molécules ellipsoidales*, J. Phys. Radium **7**, 1 (1936).

[Pia91] R. Piazza and V. Degiorgio: *Single-particle dynamics in a colloidal crystal*, Physical Review Letters **67**, 3868 (1991).

[Por10] H. Portalès, N. Goubet, L. Saviot, P. Yang, S. Sirotkin, E. Duval, A. Mermet and M.-P. Pileni: *Crystallinity Dependence of the Plasmon Resonant Raman Scattering by Anisotropic Gold Nanocrystals*, ACS Nano **4**, 3489 (2010).

[Pro82] S. W. Provencher: *CONTIN: A general purpose constrained regularization program for inverting noisy linear algebraic and integral equations*, Computer Physics Communications **27**, 229 (1982).

[Que10] F. Quemeneur, M. Rinaudo, G. Maret and B. Pépin-Donat: *Decoration of lipid vesicles by polyelectrolytes: mechanism and structure*, Soft Matter **6**, 4471 (2010).

[Ran03] S. Rangelov, K. Edwards, M. Almgren and G. Karlsson: *Steric Stabilization of Egg-Phosphatidylcholine Liposomes by Copolymers Bearing Short Blocks of Lipid-Mimetic Units*, Langmuir **19**, 172 (2003).

[Rei08] L. Reimer and H. Kohl: *Transmission Electron Microscopy: Physics of Image Formation*, Springer, 2008.

[RR06] B. M. Rothen-Rutishauser, S. Schurch, B. Haenni, N. Kapp and P. Gehr: *Interaction of fine particles and nanoparticles with red blood cells visualized with advanced microscopic techniques*, Environmental Science & Technology **40**, 4353 (2006).

[Sal14] K. M. Salerno, A. E. Ismail, J. M. D. Lane and G. S. Grest: *Coating thickness and coverage effects on the forces between silica nanoparticles in water*, The Journal of Chemical Physics **140**, 194904 (2014).

[Sav11] S. Savarala, S. Ahmed, M. A. Ilies and S. L. Wunder: *Stabilization of Soft Lipid Colloids: Competing Effects of Nanoparticle Decoration and Supported Lipid Bilayer Formation*, ACS Nano **5**, 2619 (2011).

[Sch99] K. Schillén, K. Bryskhe and Y. S. Mel'nikova: *Vesicles Formed from a Poly(ethylene oxide)-Poly(propylene oxide)-Poly(ethylene oxide) Triblock Copolymer in Dilute Aqueous Solution*, Macromolecules **32**, 6885 (1999).

[Sch04] J. R. Schmidt and J. L. Skinner: *Brownian Motion of a Rough Sphere and the Stokes-Einstein Law*, The Journal of Physical Chemistry B **108**, 6767 (2004).

[Sch07] W. Schärtl: *Light Scattering from Polymer Solutions and Nanoparticle Dispersions*, Springer, 2007.

[Sch08] O. Schubert, J. Becker, L. Carbone, Y. Khalavka, T. Provalska, I. Zins and C. Sönnichsen: *Mapping the Polarization Pattern of Plasmon Modes Reveals Nanoparticle Symmetry*, Nano Lett. **8**, 2345 (2008).

[Sch14] G. Schmid (ed.): *Nanoparticles: From Theory to Application*, Wiley-VCH Verlag GmbH, 2014.

[Sha05] S. S. Shankar, S. Bhargava and M. Sastry: *Synthesis of Gold Nanospheres and Nanotriangles by the Turkevich Approach*, Journal of Nanoscience and Nanotechnology **5**, 1721 (2005).

[Shi13] D. Shi, C. Song, Q. Jiang, Z.-G. Wang and B. Ding: *A facile and efficient method to modify gold nanorods with thiolated DNA at a low pH value*, Chemical Communications **49**, 2533 (2013).

[Smi07] K. A. Smith, D. Jasnow and A. C. Balazs: *Designing synthetic vesicles that engulf nanoscopic particles*, Journal of Chemical Physics **127**, 084703 (2007).

[Smo06] M. von Smoluchowski: *Zur kinetischen Theorie der Brownschen Molekularbewegung und der Suspensionen*, Annalen der Physik **326**, 756 (1906).

[Spe93] W. Spevak, J. O. Nagy, D. H. Charych, M. E. Schaefer, J. H. Gilbert and M. D. Bednarski: *Polymerized liposomes containing C-glycosides of sialic acid:*

potent inhibitors of influenza virus in vitro infectivity, Journal of the American Chemical Society **115**, 1146 (1993).

[Tan74] C. Tanford: *Theory of micelle formation in aqueous solutions*, The Journal of Physical Chemistry **78**, 2469 (1974).

[Tan80] C. Tanford: *The Hydrophobic Effect: Formation of Micelles and Biological Membranes*, Wiley, 1980.

[Tan07] Y. Tang and M. Ouyang: *Tailoring properties and functionalities of metal nanoparticles through crystallinity engineering*, Nature Materials **6**, 754 (2007).

[Ter02] I. Teraoka: *Polymer Solutions*, John Wiley & Sons, Inc., 2002.

[The85] D. N. Theodorou and U. W. Suter: *Shape of unperturbed linear polymers: polypropylene*, Macromolecules **18**, 1206 (1985).

[Tir84] M. M. Tirado, C. L. Martinez and J. G. de la Torre: *Comparison of theories for the translational and rotational diffusion coefficients of rod-like macromolecules. Application to short DNA fragments*, The Journal of Chemical Physics **81**, 2047 (1984).

[Tor81] J. de la Torre, de la Torre and V. A. Bloomfield: *Hydrodynamic properties of complex, rigid, biological macromolecules: theory and applications*, Quarterly Reviews of Biophysics **14**, 81 (1981).

[Tur51] J. Turkevich, P. C. Stevenson and J. Hillier: *A study of the nucleation and growth processes in the synthesis of colloidal gold*, Discussions of the Faraday Society **11**, 55 (1951).

[Und94] S. Underwood and P. Mulvaney: *Effect of the Solution Refractive Index on the Color of Gold Colloids*, Langmuir **10**, 3427 (1994).

[Une07] T. Uneyama: *Density functional simulation of spontaneous formation of vesicle in block copolymer solutions*, The Journal of Chemical Physics **126**, 114902 (2007).

[Ver47] E. J. W. Verwey: *Theory of the Stability of Lyophobic Colloids.*, J. Phys. Chem. **51**, 631 (1947).

[Wan08] B. Wang, L. F. Zhang, S. C. Bae and S. Granick: *Nanoparticle-induced surface reconstruction of phospholipid membranes*, Proceedings of the National Academy of Sciences of the United States of America **105**, 18171 (2008).

[Wil70] G. Williams and D. C. Watts: *Non-symmetrical dielectric relaxation behaviour arising from a simple empirical decay function*, Trans. Faraday Soc. **66**, 80 (1970).

[Win13] S. Winzen, M. Bernhardt, D. Schaeffel, A. Koch, M. Kappl, K. Koynov, K. Landfester and A. Kroeger: *Submicron hybrid vesicles consisting of polymer-lipid and polymer-cholesterol blends*, Soft Matter **9**, 5883 (2013).

[Wu96] C. Wu and S. Zhou: *First Observation of the Molten Globule State of a Single Homopolymer Chain*, Physical Review Letters **77**, 3053 (1996).

[Yam02] S. Yamamoto, Y. Maruyama and S.-a. Hyodo: *Dissipative particle dynamics study of spontaneous vesicle formation of amphiphilic molecules*, The Journal of Chemical Physics **116**, 5842 (2002).

[Yos01] S. Yoshioka, Y. Aso and S. Kojima: *Usefulness of the Kohlrausch-Williams-Watts stretched exponential function to describe protein aggregation in lyophilized formulations and the temperature dependence near the glass transition temperature.*, Pharm Res **18**, 256 (2001).

[Yu07a] C. Yu and J. Irudayaraj: *Quantitative Evaluation of Sensitivity and Selectivity of Multiplex NanoSPR Biosensor Assays*, Biophysical Journal **93**, 3684 (2007).

[Yu07b] Y. Yu, S. M. Anthony, L. F. Zhang, S. C. Bae and S. Granick: *Cationic nanoparticles stabilize zwitterionic liposomes better than anionic ones*, Journal of Physical Chemistry C **111**, 8233 (2007).

[Yua12] H. Yuan, C. G. Khoury, H. Hwang, C. M. Wilson, G. A. Grant and T. Vo-Dinh: *Gold nanostars: surfactant-free synthesis, 3D modelling, and two-photon photoluminescence imaging*, Nanotechnology **23**, 075102 (2012).

[Zie11] C. Ziegler and A. Eychmuller: *Seeded Growth Synthesis of Uniform Gold Nanoparticles with Diameters of 15-300 nm*, Journal of Physical Chemistry C **115**, 4502 (2011).

Appendix

A Experimental Details

A.1 Particles

Table 1: *Overview of all AuNPs used in this study, sorted by shape and surface grafting.*

	Citr.	CTAB	MUA	PEG 16	PEG 45	PEG 107	PEG 107-COOH	DNA T10	DNA T40
Sphere d = 41 nm	x	x	x	x	x	x	x	-	-
Sphere d = 44 nm	x	x	x	x	x	x	x	x	x
Rod AR ≈ 3.0	-	x	x	-	-	-	-	-	-
Rod AR ≈ 3.2	-	x	x	-	-	-	-	-	-
Rod AR ≈ 3.7	-	x	x	-	-	-	-	-	-
Rod AR ≈ 3.9	-	x	x	-	-	-	-	-	-
Rod AR ≈ 4.3	-	x	x	-	-	-	-	-	-

A.2 Cleaning of cuvettes

Prior to PCS measurement the cylindrical cuvettes were cleaned as follows:

- Cleaning in aqueous solution of Hellmanex® (1 Vol.-%) for 30 min at room temperature.
- Extensive rinsing with Milli-Q water
- Extensive rinsing with boiling acetone in a Thurmont-apperatus.

The cuvettes were then immediately placed into a flowbox in order to keep them dust-free. It was waited for at least 30 min for evaporation of remaining acetone in the cuvettes.

B Theoretical Details

B.1 Fits for Polymersome Characterization by PCS

The fits for characterizing polymersomes by PCS were adopted from [Jas12a]. A modified Rayleigh-Gans-Debye (RGD) approach of the total scattered intensity I for a coated sphere was used to represent polymersomes [Hal91]:

$$I(q) = \left[(m_1 - 1)\left(\frac{3j_1(x)}{x} + f^3\frac{m_2 - m_1}{m_1 - 1}\frac{3j_1(fx)}{fx}\right)\right]^2 \quad (1)$$

where

- $x = R_p \cdot q$
- $f = 1 - d/R_p$
- $m_1 = n_1/n_0$, the relative refractive index of the shell ($n_1 = 1.4$) divided by the refractive index of the solvent ($n_0 = 1.33$)

- $m_2 = n_2/n_0$, the relative refractive index of the lumen ($n_2 = 1.33$ for empty vesicles) divided by the refractive index of the solvent
- $j_1(x)$, the first-order spherical Bessel function

Since polymersomes exhibit a size distribution, the scattered intensity of a polydisperse system is given by:

$$I(q,R) = \frac{\int R^6 f_g(r) I_p dR}{\int R^6 f_g(R) dR} \tag{2}$$

$$f_g(R) = \frac{1}{m!}\left[\left(\frac{m+1}{\bar{R}}\right)^{m+1} R^m e^{-\frac{(m+1)r}{\bar{R}}}\right] \tag{3}$$

with $f_g(R)$ being the two-parameter unimodal Schulz distribution for fraction of particles having a radius R [Ara76]. $\bar{R}$ is the number average size of the particle/polymersome, m is a parameter related to the polydispersity via PDI $= \frac{1}{m+1}$. m can only be in whole numbers.

The q-dependence of the diffusion coefficient is described by:

$$\frac{\Gamma(q)}{q^2} = \frac{\int \frac{f_g(R) I_p D_i}{R^2} dR}{\int \frac{f_g(R) I_p}{R^2} dR} \tag{4}$$

B.2 Theoretical simulations on spherical AuNPs

Here, the theoretical simulations performed by Gaetan Leveque for the Nanoletters paper are described.

Depolarization ratio of naked AuNPs with Green's tensor simulations

The effect of size dispersion on bared AuNPs has been investigated using the Green's tensor formalism [Mar98], which allows computing the electromagnetic field scattered by

a small object embedded in a multilayered environment, under an arbitrary monochromatic illumination of pulsation ω. It relies on the resolution of the Lippmann-Schwinger equation:

$$\mathbf{E} = \mathbf{E}_0 + k_0^2 \int_V \mathbf{G}_0(\mathbf{r}, \mathbf{r}', \omega) \overline{\overline{\Delta\epsilon}}(\omega) \mathbf{E}(\mathbf{r}', \omega) dV \tag{5}$$

where V is the NP's volume, $\mathbf{E}_0$ the complex incident electric field, $\mathbf{E}$ the complex total electric field, and $\mathrm{k}_0 = \omega/\mathrm{c}$ is the wavevector of the light in the vacuum. The tensor $\mathbf{G}_0(\mathbf{r},\mathbf{r}',\omega)$ is the Green's function of the homogeneous water environment, which is analytical for every couple $(\mathbf{r},\mathbf{r}')$ in the whole space. Moreover, the tensor $\overline{\overline{\Delta\epsilon}}(\omega)$ is defined by:

$$\overline{\overline{\Delta\epsilon}}(\omega) = \bar{\bar{\epsilon}}(\omega) - \epsilon_B \tag{6}$$

where ϵ_B is the dielectric constant of water, and $\bar{\bar{\epsilon}}(\omega)$ is the gold dielectric constant, tensorial if the particle is polycrystalline, as explained earlier.

The first step of the simulation is the discretization of the AuNP in small polarizable cells, which allows accessing the NP internal field in every discretization point by numerically solving the Lippmann-Schwinger equation. The second step is the computation of the electric field scattered at infinity in the plane perpendicular to the incidence plane of the incident plane wave, through:

$$\mathbf{E}_S = k_0^2 \int_V \mathbf{G}_\infty(\Theta, \Phi; \mathbf{r}', \omega) \overline{\overline{\Delta\epsilon}} \mathbf{E}(\mathbf{r}', \omega) dV \tag{7}$$

where (Θ, Φ) are the detection directions and $\mathbf{G}_\infty(\Theta, \Phi; \mathbf{r}', \omega)$ is the asymptotic Green's function. Then, the polarized $\mathrm{I}_{VV}^{\Theta,\Phi}$ and depolarized $\mathrm{I}_{VH}^{\Theta,\Phi}$ intensities in the (Θ, Φ) direction are:

$$I_{VV}^{\Theta,\Phi} = \left| E_S(\Theta, \Phi) \cdot \frac{E_0}{\|E_0\|} \right|^2 \tag{8}$$

$$I_{VH}^{\Theta,\Phi} = |E_S(\Theta, \Phi)|^2 - I_{VV}^{\Theta,\Phi} \tag{9}$$

Finally, the scattered intensities are numerically averaged on the incident field orientation in order to obtain $\rho(\omega) = \mathrm{I}_{VH}(\omega)/I_{VV}(\omega)$.

Theoretical model for the AuNPs polycrystallinity

A basic phenomenological model for the gold polycrystallinity has been implemented in the theoretical calculations. In this very simple approach, the polycrystalline particle is described as a spheroidal particle cut into several parallel slices of equal thickness l, along the direction of one of the principal axis, as shown in Figure B.1. When the particle is cut in 2, 3, 4, ... , n parts (n being called in the following the polycrystallinity order), l takes the values 2R/2, 2R/3, 2R/4, ... , 2R/n. Each interface between two slices behaves as a barrier that increases the collisions rate of electrons moving normally to it, due to the shortening of the electrons mean free path in that direction. For electrons moving parallel to the cut planes, the absorption rate can as well be increased due to a shortening of the mean-free path by the NP outer surface, when its diameter becomes smaller than the bulk free electron mean free path. This effect can be taken into account in the gold dielectric constant by increasing the absorption rate of the free-electrons contribution to ϵ_{bulk}, the dielectric constant of the bulk gold. Such corrections are usually applied to describe the dielectric constant of gold NP of very small diameter, typically 20 nm and below [Ber05]. In this model, the dielectric constant reads:

$$\epsilon_l(\omega) = \epsilon_{bulk}(\omega) - \delta\epsilon_f(\omega) + \delta\epsilon_f^c(\omega) \tag{10}$$

where $\delta\epsilon_f(\omega)$ is the bulk contribution of the free electrons:

$$\delta\epsilon_f(\omega) = 1 - \frac{\omega_p^2}{\omega(\omega + i\Gamma)} \tag{11}$$

and $\delta\epsilon_f^c(\omega)$ is the corrected contribution of the free electrons:

$$\delta\epsilon_f^c(\omega) = 1 - \frac{\omega_p^2}{\omega(\omega + i\widetilde{\Gamma})}, \quad \text{with:} \quad i\widetilde{\Gamma} = \Gamma + \frac{A}{L} \tag{12}$$

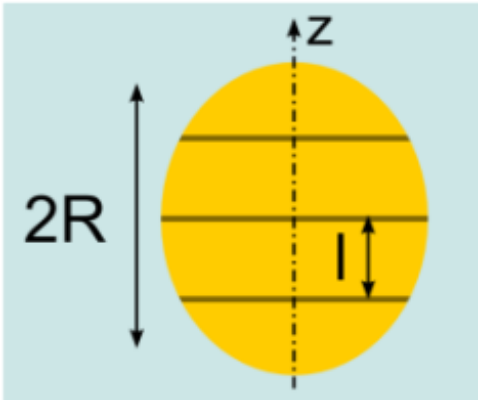

Figure B.1: *Schematic representation of the polycrystalline gold nanoparticle, cut into four slices of thickness l along the z-direction.*

The bulk absorption rate Γ is increased by a factor inversely proportional to the length scale L (slice thickness and/or particle dimensions). More precisely, in the direction perpendicular to the cut, $L = l$, whereas along the two parallel directions, $L = 2R$.

Depolarization ratio of grafted AuNPs with an analytical model in the quasi-static approximation

In the quasi-static approximation, where the wavelength of the incident plane wave is large compared to the nanoparticle dimensions, the retardation effects of the wave inside the particle can be neglected. It can be shown that the polarization inside a spheroid is then homogeneous and proportional to the incident electric field through:

$$\mathbf{P} = \frac{\overline{\overline{\alpha}}(\omega)}{V}\mathbf{E}_0 \tag{13}$$

where the tensorial polarizability $\overline{\overline{\alpha}}(\omega)$ is diagonal inside the principal-axes frame of the spheroid:

$$\overline{\overline{\alpha}}(\omega) = \begin{bmatrix} a_x & 0 & 0 \\ 0 & a_y & 0 \\ 0 & 0 & a_z \end{bmatrix} \tag{14}$$

Each diagonal term can be written as:

$$a_i = V\epsilon_0 \frac{\epsilon_B \Delta\epsilon_i}{\epsilon_B + L_i \Delta\epsilon_i}, \quad i = x, y, z \tag{15}$$

where $\Delta\epsilon_i = \epsilon_i(\omega) - \epsilon_B$ and L_i is the depolarization factor, which depends on the shape of the particle. Notice the dependency of the gold dielectric constant $\epsilon_i(\omega)$ on the direction $i = x, y, z$, necessary to describe the NP's polycrystallinity. We will consider spheroids for which the symmetry axis is the z-axis. If b is the length of the semi-major axis and a the length of the semi-minor axis, the L_z factors are given in Table 2 [Boh98].

Table 2: *Depolarization factors of a spheroid of semi-major axis length b and two identical semi-minor axis lengths a.*

r = b/a	**r > 1 (prolate)**	**r < 1 (oblate)**
e	$\sqrt{1 - 1/r^2}$	$\sqrt{1 - r^2}$
L_z	$\frac{1-e^2}{2e^3}\left(\ln(\frac{1+e}{1-e}) - 2e\right)$	$1 - \frac{g(e)}{e^2}\left(\frac{\pi}{2} - \text{atan}(g(e))\right) + g(e)^2$, $g(e) = \frac{\sqrt{1-e^2}}{e}$

whereas $L_x = L_y = (1 - L_z)/2$.

The expression (Equation 15) can be generalized to a core-shell spheroid. With unchanged notations for the gold spheroidal core and considering the external shape of the shell (dielectric constant ϵ_1) with the same symmetry axis z, semi-major and semi-minor axis lengths respectively b' and a', the polarizability components are [Boh98]:

$$a_i = V\epsilon_0 \frac{(\epsilon_1 - \epsilon_B)[\epsilon_1 + \Delta\epsilon_1(L_i^c - fL_i)] + f\epsilon_1\Delta\epsilon_1}{[\epsilon_1 + \Delta\epsilon_1(L_i^c - fL_i)][\epsilon_B + (\epsilon_1 - \epsilon_B)L_i] + fL_i\epsilon_1\Delta\epsilon_1} \tag{16}$$

with:

$$f = \frac{a^2 b}{a'^2 b'} \tag{17}$$

and:

$$\Delta\epsilon_1 = \epsilon_i(\omega) - \epsilon_1 \tag{18}$$

The depolarization factors L_i and L_i^c have the same expression as in Table 2.

Finally, after averaging the Au nanoparticle orientation, the depolarization ratio $\rho(\omega) = I_{VH}(\omega)/I_{VV}(\omega)$ is [Deg94]:

$$\rho(\omega) = 12\frac{|a_x + a_y - 2a_z|^2 + 3|a_x - a_y|^2}{5|a_x + a_y + a_z|^2 + |a_x + a_y - 2a_z|^2} \tag{19}$$

As an illustration, Figure B.2a shows the evolution of the maximum depolarization ratio ρ (occurring for a wavelength of about 532 nm) of a core-shell nanoparticle with spherical gold core and spheroidal shell with different refractive indexes n_{graft}. The value a'+b' = 25 nm is kept constant while b' is varied from 0 nm to 25 nm. The polycrystallinity order is fixed to n = 2, the cut plane being perpendicular to the NP revolution axis. The depolarization ratio is minimal for a spherical shell. Figure B.2b shows the ratio $\rho^* = \rho(532\ nm)/\rho(632nm)$ as a function of b', for different values of the shell refractive indexes. In order to obtain $\rho^* < 1$, the NP must be oblate, with a minimum value for b' decreasing with n_{graft}.

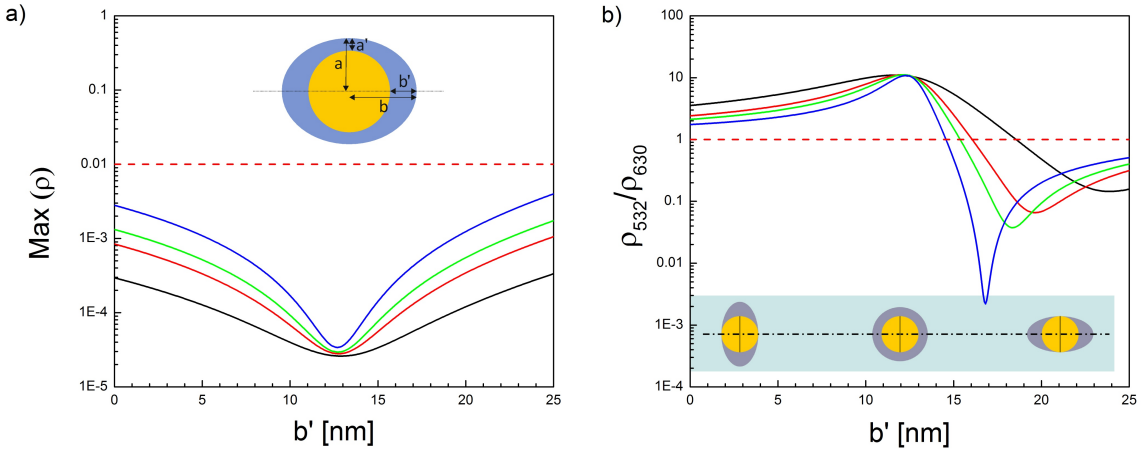

Figure B.2: *a) Depolarization ratio ρ for spherical gold cores as a function of the coating thickness and anisotropy along the particle long axis; b) ratio $\rho^* = \rho(532nm)/\rho(632nm)$. Blue: n=1.40, green: n=1.46 (PEG), red: n=1.50 (citrate), black: n=1.60 (DNA).*

B.3 Perrin's Equations

$$D_{\perp}^{\mathrm{r}} = \frac{k_{\mathrm{B}}T}{6\eta V_{\mathrm{hydro}} g_{\perp}} \tag{20}$$

$$g_{\perp} = \frac{2(p^4-1)}{3p\left[(2p^2-1)S-p\right]} \tag{21}$$

$$S_{\mathrm{prolate}} = \frac{1}{\sqrt{p^2-1}} \ln\left[p+\sqrt{p^2-1}\right] \tag{22}$$

$$D^{\mathrm{t}} = \frac{k_{\mathrm{B}}T S_{\mathrm{prolate}}}{6\pi\eta b} \tag{23}$$

B.4 Fractional Coefficients for Prolate Ellipsoids

Translational (F(AR)) and rotational (G(AR)) frictional coefficients of prolate ellipsoids are:

$$F(AR) = \frac{AR}{\sqrt{AR^2-1}} \ln\left[AR+\sqrt{AR^2-1}\right] \tag{24}$$

and

$$G(AR) = \frac{AR\left[(2AR^2-1)\frac{1}{\sqrt{AR^2-1}} \ln\left[AR+\sqrt{AR^2-1}\right] - AR\right]}{2(AR^4-1)} \tag{25}$$

For oblate ellipsoids (AR $\leq$ 1), the expression for F(AR) changes to:

$$F(AR) = \frac{AR}{\sqrt{1-AR^2}} \arctan\left[AR^{-}1+\sqrt{1-AR^2}\right] \tag{26}$$

B.5 Computational Modeling of Scattering Profiles

Vesicles and nanoparticles were assigned a scattering length density, ρ, while the environment was set at $\rho = 0$, thereby effectively working with contrasts and greatly reducing the computational cost. Vesicles were modelled as shells of radii $R_{\text{ves}}^{\text{inner}}$ and $R_{\text{ves}}^{\text{outer}}$, where the scattering length density of the inner sphere was set to the environment (i.e., $\rho = 0$), while nanoparticles were described as spheres of size R_{NP}. Vesicles and nanoparticles were discretized on a cubic grid of volume $L^3 = 600$ nm^3 with grid spacing $a = 18$ nm (i.e., a small-enough length scale to probe details up to the maximum wavevector considered), assigning the scattering length density on each grid point depending on any object present.

The radius of the vesicle was optimized to best reproduce the curvature of the experimental scattering profile, though its thickness was set to $R_{\text{ves}}^{\text{outer}} - R_{\text{ves}}^{\text{inner}} = 20$ nm, while the radius of the nanoparticles was enforced to $R_{\text{NP}} = 20$ nm.

The scattering form factor was deermined using the Debye formula:

$$P(q) = \frac{1}{z^2} \sum_{i=1}^{z} \sum_{j=1}^{z} \rho_i \rho_j \frac{sin(qr_{ij})}{qr_{ij}} \tag{27}$$

where z is the number of particles, and r_{ij} is the distance between particle i and j.

Both decoration and uptake mechanisms of nanoparticles on the polymersomes were studied. For both scenarios, between 1 and 5 nanoparticles were considered close to the polymersome, distributed across the surface of the vesicle to minimize the interaction between nanoparticles. The intensity $I(q)$ is proportional to the scattering form factor. The scattering length densities to reproduce the experimental data for vesicles and nanoparticles were optimized. Figure B.3 shows a comparison between experimental and fitted scattering profiles for vesicles and nanoparticles. The optimized radii for the vesicle shell are $R_{\text{ves}}^{\text{inner}} = 120$ nm and $R_{\text{ves}}^{\text{outer}} = 140$ nm, while the effective scattering length densities were set at $\rho_{\text{ves}} = 1.5 \cdot 10^{-5}$ Å^{-2} and $\rho_{\text{ves}} = 1.0 \cdot 10^{-3}$ Å^{-2}. Good agreement for both vesicles and naoparticles were found. The computed vesicle scattering profile shows a much more pronounced dip than the experimental results, likely due to a polydispersity of polymersomes measured experimentally, effectively smearing out the dip.

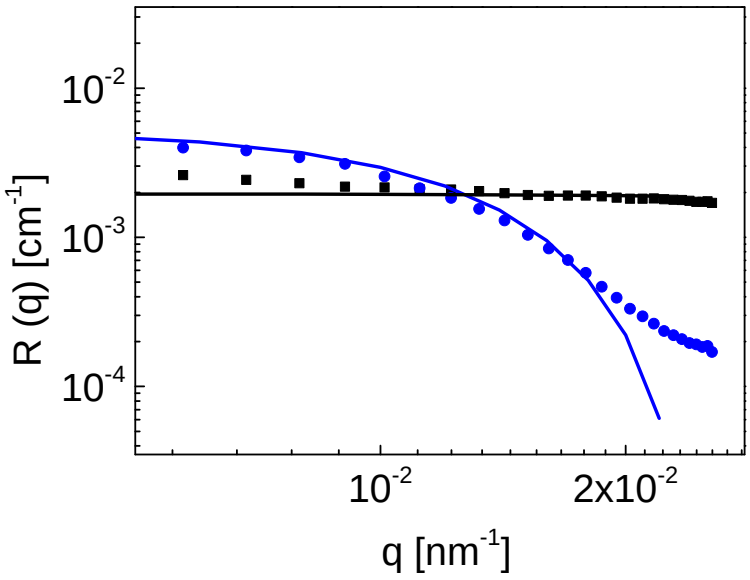

Figure B.3: *Experimental (squares) and numerical (lines) scattering profiles for vesicles (blue) and nanoparticles (black). Both numerical profiles were fitted to reproduce the experimental intensity, while the radii of the vesicle was optimized according to the curvature of the experimental data.*

For analyzing the anisotropy of the decoration mechanism, one associated a supramolecular assembly with a set of polarizabilities α, β, and γ along each Catesian direction x, y, and z, respectively. The anisotropy is then expressed by:

$$\delta = \frac{1}{2}\frac{(\alpha-\beta)^2+(\beta-\gamma)^2+(\alpha-\gamma)^2}{(\alpha+\beta+\gamma)^2} \tag{28}$$

Assuming cylindrical symmtery (i.e., $\beta = \gamma$), the ratio of the $q = 0$ intercepts of the polarized intensities enables the determination of $\delta = (\alpha - \beta)/(\alpha + 2\beta)$:

$$\frac{I_{VH}(q=0)}{I_{VV}(q=0)} = \frac{d\delta^2}{5+4\delta^2} \tag{29}$$

where I_{VH} and I_{VV} correspond to the vertical and horizontal component retained after filtering, respectively, while for both intensities the incident light is polarized vertically.

C List of Symbols and Abbreviations

α	Amplitude of the autocorrelation function
β_{KWW}	Shape parameter in PCS
χ	Flory-Huggins parameter
η	dynamic viscosity
Γ	Relaxation rate
ν	electrophoretic mobility
ρ	Depolarization ratio
τ	Relaxation time
θ	Scattering angle
ε	dielectric constant
A_2	Second viral coefficient
c	Concentration
$C(q,t)$	Field autocorrelation function
d	Distance
D^{r}	Rotational diffusion coefficient
D^{t}	Translational diffusion coefficient
dn/dc	Refractive index increment
E_{A}	Energy of attraction
E_{R}	Energy of repulsion
E_{t}	Total energy
k_{B}	Boltzmann constant
k_{i}	Incident beam vector
N_{A}	Avogadro number
$P(q)$	Form factor
R_{g}	Radius of gyration
R_{h}	Radius of hydration

R_{r}	Radius of rotation
R_{VH}	Absolute scattering intensity for a horizontally polarized incident light beam
R_{VV}	Absolute scattering intensity for a vertically polarized incident light beam
T	Temperature
T_{g}	glass-transition temperature
V	Volume
Å	Angström
AFM	Atomic Force Microscopy
AR	Aspect ratio
ATP	adenosine triphosphate
AuNP	Gold nanoparticle
AuNR	Gold Nanorods
CMC	critical micelle concentration
CTAB	Cetyl trimethylammonium bromide
DLS	Dynamic light scattering
DLVO	Derjaguin-Landau-Verwey-Overbeek
DOPC	1,2-Dioleoyl-*sn*-glycero-3-phosphocholine
FCS	Fluorescence Correlation Spectroscopy
GPC	Gel permeation chromatography
IUPAC	International Union of Pure and Applied Chemistry
KWW	Kohlrausch-Williams-Watts
MOXA	2-methyloxa-zoline
MWCO	Molecular weight cut-off
NMR	Nuclear magnetic resonance
NP	Nanoparticle
PAA	Poly(acrylic acid
PBD	Polybutadiene
PCS	Photon Correlation Spectroscopy
PDEAMA	Poly(N,N-diethylaminoethyl methacrylate

PDI	Polydispersity Index
PDMS	Poly(dimethylsiloxane)
PDMS-OH	PDMS-monocarbinol
PEE	Poly(ethylethylene)
PEG	Poly(ethylene glycol), $M_W < 20000$ g mol^{-1}
PEO	Poly(ethylene oxide), $M_W > 20000$ g mol^{-1}
PLA	Polylactide
PMOXA	Poly(2-methyloxazoline)
PPS	Poly(propylene sulfide)
PS	Polystyrene
RGD	Rayleigh-Gans-Debye
rpm	rounds per minute
SDS	sodium dodecyl sulfate
SLS	Static light scattering
SPR	Surface plasmon resonance
wt%	Weight percent

D Acknowledgments

I want to thank the many people who made this thesis possible.

First of all, I would like to thank [redacted] for giving me the opportunity to do this PhD Thesis in her group, for the interesting topic and for her professional support, both scientific and mental, and many valuable meetings and discussions over the time. I am very grateful for being a student at her group and for being taught the field of colloidal science.

I would like to give very special acknowledgments to [redacted] for teaching me light scattering, for many intense scientific discussions, for his constant guidance and support and for his assistance during writing scientific publications. I am very grateful to have worked with and learned from such a great and enthusiastic scientist.

[redacted] is very kindly acknowledged for his contributions to the Gold Nanoparticles project and for giving me the opportunity to contribute to his research. I would especially like to thank his student [redacted] and his Post-Doc [redacted] for nanoparticle preparation, PA measurements and many valuable scientific conversations.

My collaboration partners [redacted] and [redacted] are especially acknowledged for their very valuable contributions to my work. Thank you for supporting my experimental findings with your theoretical calculations and simulations, for numerous discussions, and for answering so many emails.

I would like to thank my former colleague and predecessor on the topic [redacted] for introducing me to light scattering and to vesicle preparation, and for finding the analogous between the topic and *Pacman* eating chocolates. I would also like to thank my colleague [redacted] for his contributions to the project, for supporting this thesis with cryo-TEM images, and for sharing ups and downs during these three years.

Special thanks I would like to give to the **Polymer Analytics Group**, specially to [redacted], [redacted] and [redacted] for their assistance with mea-

surements and vesicle preparation, for aligning the PCS setup, for polymer characterization and many pleasant conversations in the lab and in the coffee corner.

[redacted] is acknowledged for proofreading this thesis.

Last but not least I want to thank my family and friends for their continual support throughout my studies.